

Search for pair production of Higgs bosons via vector-boson
fusion process in the $b\bar{b}b\bar{b}$ final state using proton-proton
collisions at $\sqrt{s} = 13$ TeV with the ATLAS detector

ATLAS 検出器での重心系エネルギー 13 TeV の陽子陽子衝突を用いたベクトルボソン融合過程で
の $b\bar{b}b\bar{b}$ 終状態のヒッグス対生成事象の探索

Yuta SANO

High Energy Physics Laboratory

Department of Physics, Nagoya University

December, 2019

Abstract

The Higgs boson (h) was discovered by the ATLAS and CMS collaborations in 2012, using proton–proton (pp) collisions at the Large Hadron Collider (LHC). The measured properties have so far been found to be in agreement with the Standard Model (SM) predictions. However, there is a "fine-tuning" problem that means a quite large radiative correction is needed to explain the difference between the observed Higgs mass (125 GeV) and the bare Higgs mass in the SM. The hypothesis of Two Higgs Doublet Model (2HDM) is a candidate to solve that problem. The production of a pair of Higgs bosons (hh) is a rare process in the SM, but various models beyond the SM predict cross-sections for the hh production that are significantly higher than those of the SM prediction. The heavy scalar boson that decay into Higgs boson pairs appear in exotic scenarios of the 2HDM. Enhanced non-resonant Higgs boson pair production is also predicted by many models. Previous searches for Higgs boson pair production in the $b\bar{b}b\bar{b}$ channel were carried out in the gluon-gluon fusion (ggF) production mode by the ATLAS and CMS collaborations and limits were set for resonant and non-resonant productions.

This thesis report a search for a Higgs boson pair (hh) produced via Vector Boson Fusion (VBF) and decaying into the dominant $b\bar{b}b\bar{b}$ final state. This study provides a completely new signature in the Higgs sector. This search has complementary sensitivity to the production of an additional heavy scalar boson, that may decay into a Higgs boson pair, compared to past direct searches. Additionally, this search can place constraints on the parameters of the Higgs coupling with vector bosons, especially the quadruple coupling of $VVhh$, using the non-resonant signature. This analysis uses the Run-2 dataset collected by ATLAS at $\sqrt{s} = 13$ TeV, corresponding to 126.0 fb $^{-1}$ taken in 2016–2018.

In this research, the following items are achieved:

- The correction on the b -jet energy has been implemented to improve the resolution of the reconstructed mass of the Higgs boson candidates.
- The event selections that are specific to the VBF signal are defined and optimized.
- The unique procedure of the estimation of QCD multi-jet background and $t\bar{t}$ background is established.
- The background estimation is evaluated to be well-established.

As a result, unfortunately, no significant excess was observed, but I have worked out two important results. The first one is that the limits on the cross-section of heavy resonant signals have been set. The observed excluded region with 95% C.L. corresponding to $m_H > 666.9$ GeV for the parameters of $\tan\beta = 2.0$ and $\sin(\beta - \alpha) = 0.6$ in the Type-II 2HDM. The second one is that the limits on the cross-section of non-resonant signals with various $VVhh$ coupling strength, κ_{2V} , are set. The observed 95% C.L. limits on the cross-section of SM non-resonant HH production via VBF is given as 1450 fb. The parameter regions κ_{2V} is $\kappa_{2V} < -0.56$ and $\kappa_{2V} > 2.89$ are excluded at 95% C.L. This constraint on κ_{2V} is provided for the first time in the world. We can also explore the VBF production using the final states of $hh \rightarrow b\bar{b}\gamma\gamma, b\bar{b}\tau\tau$ and so on. This first research of $hh \rightarrow b\bar{b}b\bar{b}$ in VBF production opened up new parameter spaces, to perform a measurement of the $VVhh$ coupling and to search for new physics in specific models.

Contents

1	Introduction	1
	Introduction	1
2	Theoretical motivations	3
2.1	The Standard Model	3
2.2	The problem of the Standard Model	5
2.3	Two Higgs Doublet Model	6
2.4	hh production at LHC	7
2.4.1	Kinematics of the pp collision at LHC	7
2.4.2	Overview of non-resonant hh production	8
2.4.3	Overview of resonant hh production	9
2.4.4	Past searches for the hh production via ggF	10
2.4.5	New phenomena possible to be observed in hh production via VBF	10
3	LHC-ATLAS experiment	15
3.1	LHC accelerator	15
3.2	ATLAS detector	16
3.3	ATLAS sub-detector	17
3.3.1	Inner tracker	17
3.3.2	Calorimeter	17
3.3.3	Muon spectrometer	19
3.4	Particle Reconstruction	19
3.4.1	Jet reconstruction	19
3.4.2	b -tagging	20
3.4.3	Muon reconstruction	21
3.4.4	Electron reconstruction	22
3.5	Data taking	22
3.5.1	Trigger	22
4	Search for the hh production in vector boson fusion	24
4.1	Signal and backgrounds	24
4.1.1	Signal topology	24
4.1.2	Backgrounds	24
4.2	Collision data and used triggers	24
4.3	MC simulations	26
4.3.1	Signal MC production	26
4.3.2	ggF contamination	28
4.3.3	The samples for the background estimation	29

4.3.4	Pile-up events implemented in the MC samples and the detector simulation	29
4.4	Jet energy correction and jet selections	30
4.4.1	The b -jet energy regression	30
4.4.2	Selection for the jets	32
4.5	Trigger efficiency	33
4.5.1	Jet-level Trigger Efficiencies/Scale Factors	34
4.5.2	Calculating the event-level efficiency	34
4.6	Event selection	36
4.7	Background estimation	42
4.7.1	QCD multijet background modelling	42
4.7.2	$t\bar{t}$ Background Modelling	45
4.7.3	Control regions for the normalization of backgrounds	46
4.7.4	The kinematic reweighting	54
4.7.5	The other backgrounds	60
4.7.6	Normalization in the control regions	60
4.8	Systematic uncertainty	61
4.8.1	Systematic from signals	62
4.8.2	Systematic from backgrounds	76
4.9	Statistical analysis	80
4.9.1	Search procedure	80
4.9.2	Limit setting procedure	81
4.10	Results	82
4.10.1	The unblinded SR	82
4.10.2	Observed limits	82
5	Discussion	95
5.1	Interpretation on the Type-II 2HDM	95
5.2	Possibility of the other channels	96
5.3	Prospects for the High Luminosity LHC	97
6	Conclusion	100
	Appendices	105
A	The sensitivity with two case of cut on the η of the jets	105
B	Comparison of distributions with different pseudo tag rate	107
B.1	Non-all hadronic $t\bar{t}$	107
B.2	All hadronic $t\bar{t}$	110

Chapter 1

Introduction

Understanding the physical behavior of the elementary particles can help us know how our universe is formed. The Standard Model (SM) was formulated in the 1970s to describe the behavior of the elementary particles. In the SM, the fermions, of which six are quarks and six are leptons and whose spin is $1/2$, form the matters according to the Fermi statistics, and the gauge bosons whose spin is 1 mediate the strong, weak, and electromagnetic interactions between the fermions. The Higgs boson endows the fermions and the gauge bosons with their masses. We have discovered all of the particles in the SM and measured the observable properties of them which we can access, and the experimental observations that have been obtained so far are consistent with the SM. However, there are some problems that cannot be solved by the SM, and we are still half way down the road to grab a clue to new physics beyond the SM (BSM physics).

We have two approaches to search for the BSM physics: (1) measure the remaining couplings of the SM particles in order to grab an evidence of the effect by the BSM physics indirectly, and (2) directly search for the production events of the new particle. The discovery of the Higgs boson (h^0) by the Large Hadron Collider (LHC) experiments in 2012 [1, 2] motivates searches for the new BSM physics. Since the BSM physics can change some couplings of the Higgs boson, the measurement of the Higgs coupling strength is effective procedure for the BSM search. However, the trilinear Higgs couplings to W , Z , t , b , and τ have been measured so far, and the results are consistent with SM [3]. We have to measure not only trilinear coupling to quarks, leptons, and bosons, but also the self-coupling of Higgs bosons and quadruple coupling to vector bosons. Additionally, some BSM physics predicts heavy Higgs particle (H^0) may decays to two Higgs bosons. The events that two Higgs bosons are involved in may be an appropriate tool for the approach (1) and (2).

This thesis discusses the search for the pair production of the SM Higgs bosons (hh production) at the $\sqrt{s} = 13$ TeV pp collisions, using data recorded by the ATLAS detector at the LHC. The hh production via gluon-gluon Fusion (ggF) at the LHC is important rare events which help us to search for the heavy Higgs boson may decays to two Higgs bosons or measure the self-coupling of the Higgs boson. Although the analysis which targets such a hh production have been performed so far, no evidence of the new physics has been implied, neither [4]. We should do obtain a new procedure to access the new parameter spaces of the specific BSM physics or to prove the other Higgs couplings that is challenging to be measured.

I have conducted a completely new analysis to search for the hh production via Vector Boson Fusion (VBF) using data of the pp collision with $\sqrt{s} = 13$ TeV recorded by the ATLAS detector at the LHC. This analysis is sensitive to the complementarily new parameter spaces of the model which predicts heavy Higgs boson and can newly give a significant constraint on the quadruple Higgs coupling to the vector bosons that we have never access it. This thesis contains the following discussions: In Chapter 2, the detailed theoretical backgrounds for this analysis are

summarized. In Chapter 3, the LHC accelerator and the ATLAS detector are explained. In Chapter 4, the analysis to search for the pair production of the SM Higgs bosons associated with two jets is described. In Chapter 5, the interpretation of the results is discussed. And Chapter 6 summarizes the conclusion.

Chapter 2

Theoretical motivations

2.1 The Standard Model

In the SM, the fermions of six quarks and six leptons are interacted by three forces; the strong force, the weak force, and the electromagnetic force. These forces are mediated by bosons, which are described based on a gauge-symmetry in $SU(3)_C \otimes SU(2)_L \otimes U(1)_Y$ group. The fermions are summarized in Table 2.1 and the bosons are summarized in Table 2.2.

For the weak force and the electromagnetic force, the $SU(2) \times U(1)$ gauge invariance is proposed by Glashow, Salam and Weinberg in 1960 in order to achieve the unification of the weak interactions and the electromagnetic interactions. In order to make the Lagrangian invariant under the local $SU(2) \times U(1)$ transformation, we introduce three gauge fields \vec{W}_μ for three generators \vec{T} of $SU(2)$ and one gauge field B_μ for the generator Y of $U(1)$. The Lagrangian under the gauge invariance is then

$$\begin{aligned} \mathcal{L} = & \bar{L}i\not{D}L + \bar{\nu}_R i\not{D}\nu_R + \bar{l}_R i\not{D}l_R + \bar{Q}i\not{D}Q + \bar{u}_R i\not{D}u_R + \bar{d}_R i\not{D}d_R + (D_\mu\phi)^\dagger(D^\mu\phi) - V(\phi^\dagger\phi) \\ & - [y^l(\bar{L}\phi)l_R + y^\nu(\bar{L}\phi_c)\nu_R + y^u(\bar{Q}\phi)d_R + y^d(\bar{Q}\phi_c)u_R + c.c.] - \frac{1}{4}W_{\mu\nu}^i W^{i\mu\nu} - \frac{1}{4}F_{\mu\nu}F^{\mu\nu}, \end{aligned} \quad (2.1)$$

where

$$\begin{aligned} \not{D} &= \gamma^\mu D_\mu, \quad D_\mu = \partial_\mu + ig\vec{W}_\mu\vec{T} + ig'B_\mu Y, \quad L = \begin{pmatrix} \nu_L \\ l_L \end{pmatrix}, \quad Q = \begin{pmatrix} u_L \\ d_L \end{pmatrix}, \\ \phi &= \begin{pmatrix} \phi_+ \\ \phi_0 \end{pmatrix}, \quad \vec{W}_{\mu\nu} = \partial_\nu\vec{W}_\mu - \partial_\mu\vec{W}_\nu + g\vec{W}_\mu \times \vec{W}_\nu, \quad F_{\mu\nu} = \partial_\nu B_\mu - \partial_\mu B_\nu, \\ V(\phi^\dagger\phi) &\text{ is potential which depends only on } \phi^\dagger\phi. \end{aligned} \quad (2.2)$$

The $SU(2) \times U(1)$ gauge invariance of the theory requires masses of the gauge bosons to be zero, because the mass term for the gauge bosons violates the gauge invariance. However, the three gauge bosons are observed to have masses. The Higgs mechanism that introduces algebraic transformation on the Lagrangian can avoid this situation of massless gauge bosons, which is based on the spontaneous braking of the local gauge symmetry of the Higgs field. By choosing the Higgs field as

$$\phi(x) = \frac{1}{\sqrt{2}} \begin{pmatrix} 0 \\ v + h(x) \end{pmatrix}, \quad (2.3)$$

where v is the vacuum expectation value, the gauge bosons can have there masses while they don't break the $SU(2)$ gauge symmetry. Then the terms which are involved in the Higgs field in the Lagrangian can be written as

Table 2.1: Fermions in the SM. Six quarks and six leptons are categorized in three generations according to their mass. The electric charge (Q) in the unit of the elementary charge corresponding to the charge of electrons, third-component of iso-spin(T_L^3), the hyper charge ($Y^W = Q - T_L^3$), and the spin are summarized. The L and R means the spin is left-handed and right-handed, respectively. The u, c and t are called up-type quarks and The d, s and b are called down-type quarks.

	1st-generation	2nd-generation	3rd-generation	Q	T_3	Y	Spin
quark	$\begin{pmatrix} u_L \\ d_L \end{pmatrix}$	$\begin{pmatrix} c_L \\ s_L \end{pmatrix}$	$\begin{pmatrix} t_L \\ b_L \end{pmatrix}$	$\begin{pmatrix} +\frac{2}{3} \\ -\frac{1}{3} \end{pmatrix}$	$\begin{pmatrix} +\frac{1}{2} \\ -\frac{1}{2} \end{pmatrix}$	$+\frac{1}{3}$	$\frac{1}{2}$
	u_R	c_R	t_R	$+\frac{2}{3}$	0	$+\frac{4}{3}$	$\frac{1}{2}$
	d_R	s_R	b_R	$-\frac{1}{3}$	0	$-\frac{2}{3}$	$\frac{1}{2}$
lepton	$\begin{pmatrix} \nu_{eL} \\ e_L \end{pmatrix}$	$\begin{pmatrix} \nu_{\mu L} \\ \mu_L \end{pmatrix}$	$\begin{pmatrix} \nu_{\tau L} \\ \tau_L \end{pmatrix}$	$\begin{pmatrix} 0 \\ -1 \end{pmatrix}$	$\begin{pmatrix} +\frac{1}{2} \\ -\frac{1}{2} \end{pmatrix}$	-1	$\frac{1}{2}$
	e_R	μ_R	τ_R	-1	0	-2	$\frac{1}{2}$

Table 2.2: Gauge bosons in the SM. The bosons with spin 1 carries the strong force (gluon), weak force (W^\pm and Z^0), and the electromagnetic force (γ). The Higgs boson, h , endow the fermions and the gauge bosons with the masses.

Boson	Composition	Q	T_3	Y	Spin
gluon	G_μ	0	0	0	1
W^\pm	$\begin{pmatrix} W^+ \\ W^- \end{pmatrix} = \begin{pmatrix} \frac{W_\mu^1 + W_\mu^2}{\sqrt{2}} \\ \frac{W_\mu^1 - W_\mu^2}{\sqrt{2}} \end{pmatrix}$	$\begin{pmatrix} +1 \\ -1 \end{pmatrix}$	$\begin{pmatrix} +1 \\ -1 \end{pmatrix}$	0	1
Z^0	$Z_\mu = \cos \theta_W W_\mu^3 - \sin \theta_W B_\mu$	0	0	0	1
γ	$A_\mu = \sin \theta_W W_\mu^3 + \cos \theta_W B_\mu$	0	0	0	1
h	$\begin{pmatrix} \phi^+ \\ \phi^0 \end{pmatrix} = \begin{pmatrix} 0 \\ v/\sqrt{2} \end{pmatrix}$	$\begin{pmatrix} +1 \\ 0 \end{pmatrix}$	$\begin{pmatrix} +\frac{1}{2} \\ -\frac{1}{2} \end{pmatrix}$	1	0

$$\mathcal{L} = \frac{1}{2} \left(\partial_\mu \chi \partial^\mu \chi + m_h^2 \chi^2 + \frac{1}{3} \lambda \chi^3 + \dots \right) + \frac{2v\chi + \chi^2}{4} \left(g^2 W_{+\mu}^* W_+^\mu + \frac{\bar{g}^2}{2} Z_\mu Z^\mu \right) - \frac{m_l}{v} \chi(\bar{l}l) - \frac{m_\nu}{v} \chi(\bar{\nu}\nu) - \frac{m_u}{v} \chi(\bar{u}u) - \frac{m_d}{v} \chi(\bar{d}d) \quad (2.4)$$

where

$$\chi = \frac{1}{\sqrt{2}} \begin{pmatrix} 0 \\ h(x) \end{pmatrix}, \quad g = \frac{2m_W}{v}, \quad \bar{g} = \frac{2m_Z}{v}, \quad \lambda = \frac{m_h^2}{2v^2}. \quad (2.5)$$

m_l , m_ν , m_u , m_d , m_W , m_Z , and m_h are the mass of the charged leptons, neutrinos, up-type quarks, down-type quarks, W boson, Z boson, and Higgs boson, respectively. The strength of the Higgs couplings to the fermions and the bosons are predicted to be proportional to the mass of them. The Higgs coupling strength with W , Z , t , b , and τ have been measured using the production event of single Higgs boson at LHC experiment so far, and the results are consistent with the SM [3]. On the other hand, the terms of the Higgs self-coupling ($\frac{1}{3}\lambda\chi^3$) and the quadruple coupling of $WWhh$ and $ZZhh$ ($\frac{\chi^2}{4} (g^2 W_{+\mu}^* W_+^\mu + \frac{\bar{g}^2}{2} Z_\mu Z^\mu)$) are challenging to be measured, because we have to prove the pair production of the Higgs bosons ($h \rightarrow hh$, $WW \rightarrow hh$, or $ZZ \rightarrow hh$) whose cross-section is not significant, compared to that of the production event of single Higgs boson.

2.2 The problem of the Standard Model

Although the experimental observables are consistent with the SM, there are some problems that cannot be solved by the SM. For example, the existence of the dark matters (DMs) is indicated by the flatness of the rotation curve of spiral galaxies [5]. If the DMs are elementary particles, they must have different properties from the SM particles; stable, neutral, massive, and colorless.

Another example is the fact that the Higgs boson mass (m_h) receives one-loop collections:

$$m_h^2 = m_0^2 + \delta m_h^2 \quad (2.6)$$

$$\delta m_h^2 = \frac{3\Lambda^2}{8\pi^2 v^2} [(4m_t^2 - 2m_W^2 - m_Z^2 - m_h^2) + O(\log \frac{\Lambda}{\mu})] \quad (2.7)$$

where m_0 , m_t , m_W , and m_Z are the mass of a bare Higgs boson, top quark, W boson, and Z boson, respectively, and Λ is a cut-off energy scale to which the SM is applicable. We recognize the contributions of the diagrams of Figure 2.1. Plugging the numbers, $m_h = 125$ GeV and $\Lambda \sim M_P \sim 10^{19}$ GeV (M_P : Planck mass), we see that the mass must be adjusted to more than 30 orders of magnitude. This is known as an intolerable fine tuning.

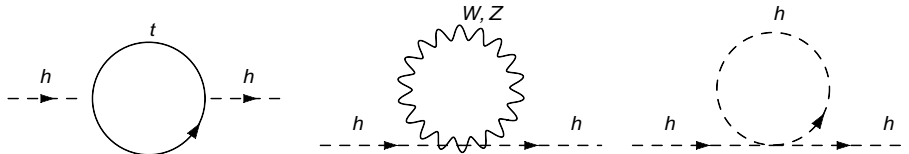


Figure 2.1: The Feynman diagrams of the correction term to the Higgs boson mass squared in the Standard Model.

As one of solutions to the fine-tuning problem, the Super Symmetry (SUSY) which is a new symmetry between a scalar field and a fermion field is one of the strongest candidates. Under the SUSY, new fermion (boson) partners are predicted for all SM bosons (fermions) like Figure 2.2. The contribution of fermions to the quadratic divergence cancels the contribution of bosons. The lightest neutral SUSY particle is one of the candidates of DMs. The SUSY requires the model which predicts additional Higgs bosons, which is described in Section 2.3.

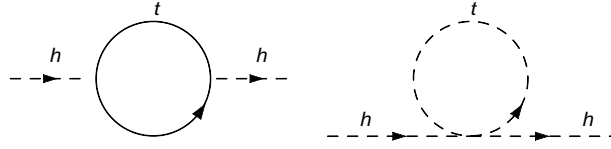


Figure 2.2: The Feynman diagrams of the correction term to the Higgs boson mass squared in SUSY model. If the \tilde{t} quark that is the bosonic partner of the t-quark exists, the contribution of fermions to the quadratic divergence is canceled.

2.3 Two Higgs Doublet Model

In the SM, only one complex Higgs doublet is introduced. There is no reason why the only one doublet exists. The model with one more Higgs doublet is called as Two Higgs Doublet Model (2HDM). In general 2HDM, the Lagrangian of quark-Higgs Yukawa interaction of the $Q = -1/3$ quarks (q) is

$$\mathcal{L} = y_{ij}^1 \bar{q}_i q_j \Phi_1 + y_{ij}^2 \bar{q}_i q_j \Phi_2 \quad (2.8)$$

where i, j are generation indices, $y_{ij}^{1,2}$ are the Yukawa couplings, and the $\Phi_{1,2}$ are the Higgs doublets. The mass matrix of the quarks is then

$$M_{ij} = y_{ij}^1 \frac{v_1}{\sqrt{2}} + y_{ij}^2 \frac{v_2}{\sqrt{2}} \quad (2.9)$$

where the $v_{1,2}$ are the vacuum expectation value of the two Higgs doublets. In this general 2HDM, there is a possibility of tree level flavor-changing neutral currents (FCNC) because y^1 and y^2 are not simultaneously diagonalizable, while there is no tree-level FCNC in the SM because diagonalizing the mass matrix automatically diagonalizes the Yukawa interactions. Many experimental measurements indicate the tree-level FCNCs are strongly suppressed. If all fermions with the same quantum numbers (which are thus capable of mixing) couple to the same Higgs multiplet, then FCNC will be absent. Under that constraint, there are four types depending on which doublet couples to up-type quark, down-type quark, or charged leptons, so that we prohibit the tree-level FCNC as summarized in Table 2.3. The SUSY requires the Type-II 2HDM.

There are eight degrees of freedom for the Higgs field when two complex Higgs doublets are introduced. Under the $SU(2)$ symmetry, three degrees are absorbed by gauge bosons so that the gauge bosons become massive. Because of that, we have five Higgs bosons with the remaining freedom: h^0 and H^0 that are neutral scalar Higgs bosons but only mass is different, H^\pm that are charged scalar Higgs bosons, and A^0 that is pseudo scalar Higgs boson. We can assume the h^0 is a Higgs boson which has been discovered by LHC experiments.

Table 2.3: This table shows which Higgs doublets couples (Φ_1 and Φ_2) to up-type quarks, down-type quarks, and charged leptons in the four types of the model with the case that the tree-level FCNC is prohibited.

Model	up-type quarks	down-type quarks	charged leptons
Type-I	Φ_2	Φ_2	Φ_2
Type-II	Φ_2	Φ_1	Φ_1
Type-X	Φ_2	Φ_2	Φ_1
Type-Y	Φ_2	Φ_1	Φ_2

2.4 hh production at LHC

We have two approaches to search for the BSM physics: (1) measure the remaining couplings of the SM particles in order to grab an evidence of the effect by the BSM physics indirectly, and (2) directly search for the resonant signal of the new particle. The pair production of the Higgs bosons in the pp collision at LHC is appropriate tool for accessing the self-coupling of the Higgs boson and the quadruple coupling with vector bosons, and searching for the heavy Higgs boson predicted in the 2HDM. The sensitivity for them at the LHC experiment will be discussed in this section.

2.4.1 Kinematics of the pp collision at LHC

The LHC is a proton-proton collider with the center of mass energy $\sqrt{s} = 13$ TeV. At the pp collision, the interactions between quarks and gluons which constitute protons are occurred. The production cross-section for a specific process in the pp collision can be written as:

$$\sigma_{pp \rightarrow X} = \sum_{ij} \int dx_1 dx_2 f_i(x_1, \mu_F^2) f_j(x_2, \mu_F^2) \hat{\sigma}_{ij \rightarrow X}(x_1, x_2, Q^2, \mu_F^2, \mu_R^2, \alpha_s(\mu_R^2)) \quad (2.10)$$

where $f_i(x, \mu_F^2)$ is the parton distribution function (PDF) for the partons $i = g, q, \bar{q}$ (g is gluon, and q is quark) and $\hat{\sigma}_{ij \rightarrow X}$ is the cross-section between the partons of i and j . x_k ($k = 1, 2$) is a longitudinal momentum fraction of the total proton momentum and Q is momentum transfer of the event. μ_F is so-called factorization factor which sets a minimum cutoff energy scale to avoid the divergent contributions of the small-angle emissions. The emissions with transverse momenta below μ_F are accounted for within the PDFs, $f_i(x_k, \mu_F^2)$. μ_R is so-called renormalization factor which keep the strong coupling satisfies the following renormalization group equation:

$$\mu_R^2 \frac{d\alpha_s}{d\mu_R^2} = -(b_0\alpha_s^2 + b_1\alpha_s^3 + b_2\alpha_s^4 + \dots) \quad (2.11)$$

where b_0 , b_1 , and b_2 are 1, 2, and 3-loop coefficient, respectively. The μ_F and μ_R are chosen to be close to the scale of the momentum transfer Q in a given process.

Figure 2.3 shows the PDF at two scale choices ($Q = 2$ GeV and $Q = 85$ GeV). Four PDFs are shown: valence up-quarks ($u_{\text{valence}}(x, Q) = (u - \bar{u})(x, Q)$) in red, valence down-quarks ($d_{\text{valence}}(x, Q) = (d - \bar{d})(x, Q)$) in blue, sea quarks ($q_{\text{sea}}(x, Q) = 2(\bar{u} + \bar{d} + \bar{s})(x, Q)$) in blown, and gluons ($g(x, Q)$) in green. The production process starts from the collision of the partons with the specific energy scale.

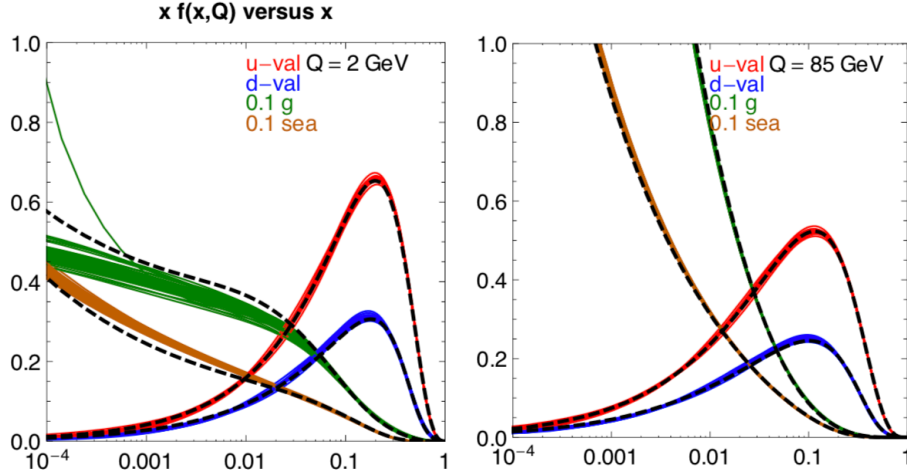


Figure 2.3: CT10 NNLO (solid color) and NLO (dashed) parton distribution functions at two scale choices ($Q = 2$ GeV and $Q = 85$ GeV). [6]

2.4.2 Overview of non-resonant hh production

In the SM, the hh production at the pp collision of $\sqrt{s} = 13$ TeV is mainly caused by (1) gluon-gluon Fusion (ggF) as shown in Figure 2.4 or (2) Vector Boson Fusion (VBF) as shown in Figure 2.5.

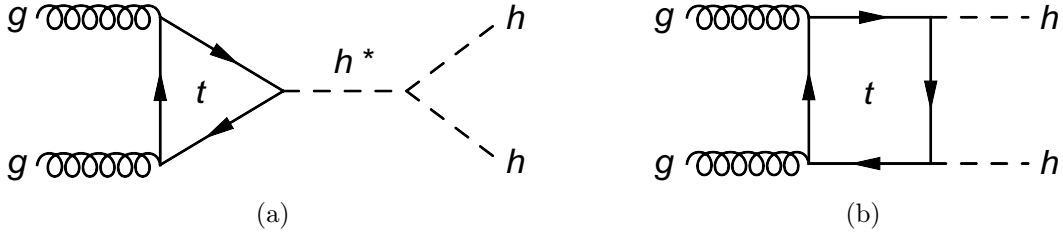


Figure 2.4: Tree-level Feynman diagrams contributing to SM non-resonant Higgs boson pair production via ggF.

The feature of the hh production via ggF is that we can test the strength of the self coupling of the Higgs boson using the production mode. In the SM, the interference between the two diagrams in Figure 2.4 is destructive and the cross-section of the hh production via ggF at $\sqrt{s} = 13$ TeV is 33.4 fb. However, the amplitude of the diagram (a) is proportional to the Higgs self-coupling λ and the cross-section can be enhanced significantly by increasing the amplitude due to the BSM physics. The measurement of the self-coupling has been conducted so far at LHC experiment, which is summarized in the Section 2.4.4.

On the other hand, the feature of the hh production via VBF is that we can access the quadruple coupling with vector bosons ($VVhh$ coupling) using the production mode. In the SM, the amplitudes of (b) and (c) in Figure 2.5 are canceled out by interference and the cross-section at $\sqrt{s} = 13$ TeV is 1.72 fb. The amplitude of the diagram (c) is proportional to the $VVhh$ coupling and the cross-section can be enhanced significantly by increasing the amplitude due to the BSM physics. The details of the enhancement are described in Section 2.4.5. The measurement of the $VVhh$ coupling had never been conducted.

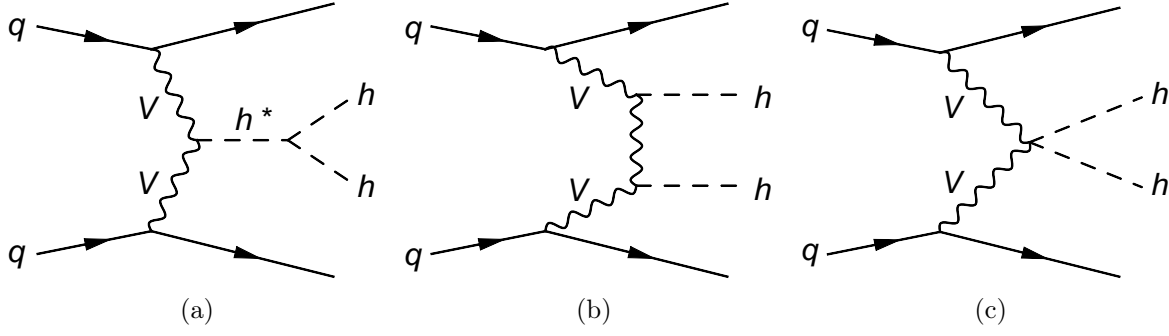


Figure 2.5: Tree-level Feynman diagrams contributing to SM non-resonant Higgs boson pair production via VBF.

2.4.3 Overview of resonant hh production

As well as the enhancement of the cross-section of hh production by the varied Higgs couplings, the resonant signal due to the production of the heavy Higgs boson may decay into two Higgs bosons ($H \rightarrow hh$), whose diagram is shown in Figure 2.6, can make excess in the data.

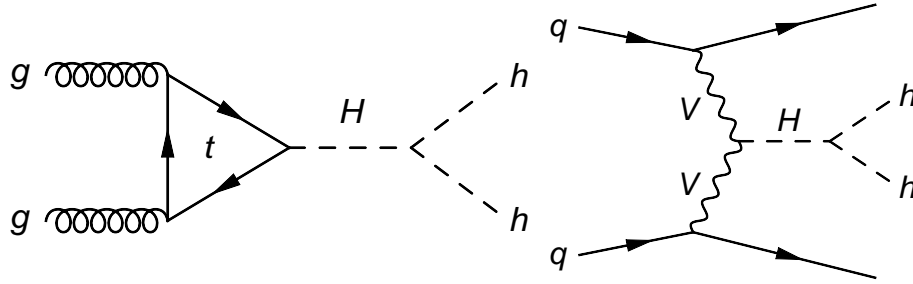


Figure 2.6: Tree-level Feynman diagrams contributing to resonant Higgs boson pair production via ggF (left) or VBF (right).

In the 2HDM, the couplings of the h^0 and H^0 to the vector bosons or the fermions are described using two parameters; the mixing angle of two neutral Higgs bosons (α), and the ratio of the vacuum expectation values of two Higgs doublets ($\tan \beta$) as shown in Table 2.4. As we can see in Figure 2.6, the production via ggF is involved in the coupling of the heavy Higgs boson to the up-type quarks and the production via VBF is involved in the coupling of the heavy Higgs boson to the vector bosons. Therefore, the dependences of the production cross-section of the heavy Higgs boson via ggF and VBF on the angle parameters are different. It is important to search for the production of the heavy Higgs boson via both of ggF and VBF for the complementarity.

Table 2.4: The couplings of h^0 and H^0 with the up-type quarks (g_{uu}) and vector bosons (g_{VV}) in the 2HDM.

	g_{uu}	g_{VV}
h^0	$\propto \cos \alpha / \sin \beta$	$\propto \sin (\beta - \alpha)$
H^0	$\propto \sin \alpha / \sin \beta$	$\propto \cos (\beta - \alpha)$

2.4.4 Past searches for the hh production via ggF

The analysis of the hh production via ggF has been performed using the dataset of 27–36 fb $^{-1}$ with $\sqrt{s} = 13$ TeV at the LHC experiment. The analysis has been performed in the various final states including $hh \rightarrow b\bar{b}b\bar{b}$, $b\bar{b}\tau^-\tau^+$, $b\bar{b}\gamma\gamma$, $b\bar{b}WW$ whose branching ratio of the hh decay is leading as shown in Table 2.5 [4]. The observed events are consistent with the SM hypothesis and no excess on the events due to the BSM physics has been observed in all channels.

The combination results of the all channels give us the upper limit on the SM cross-section of ggF production of $6.9 \times \sigma_{ggF}^{SM}$ and the constraint on the κ_λ which is the ratio with the λ in the SM (about 0.13) of $\kappa_\lambda \in [-5.0, 12]$ as shown in Figure 2.7.

Table 2.5: The branching ratio of the hh decay. The column and row are categorized with the pattern of the decays of the two Higgs bosons.

	$h \rightarrow b\bar{b}$	$h \rightarrow WW$	$h \rightarrow \tau\tau$	$h \rightarrow ZZ$	$h \rightarrow \gamma\gamma$
$h \rightarrow b\bar{b}$	34%	25%	7%	3%	0.3%
$h \rightarrow WW$	-	5%	3%	1%	0.1%
$h \rightarrow \tau\tau$	-	-	0.4%	0.3%	0.03%
$h \rightarrow ZZ$	-	-	-	0.07%	0.01%
$h \rightarrow \gamma\gamma$	-	-	-	-	0.0005%

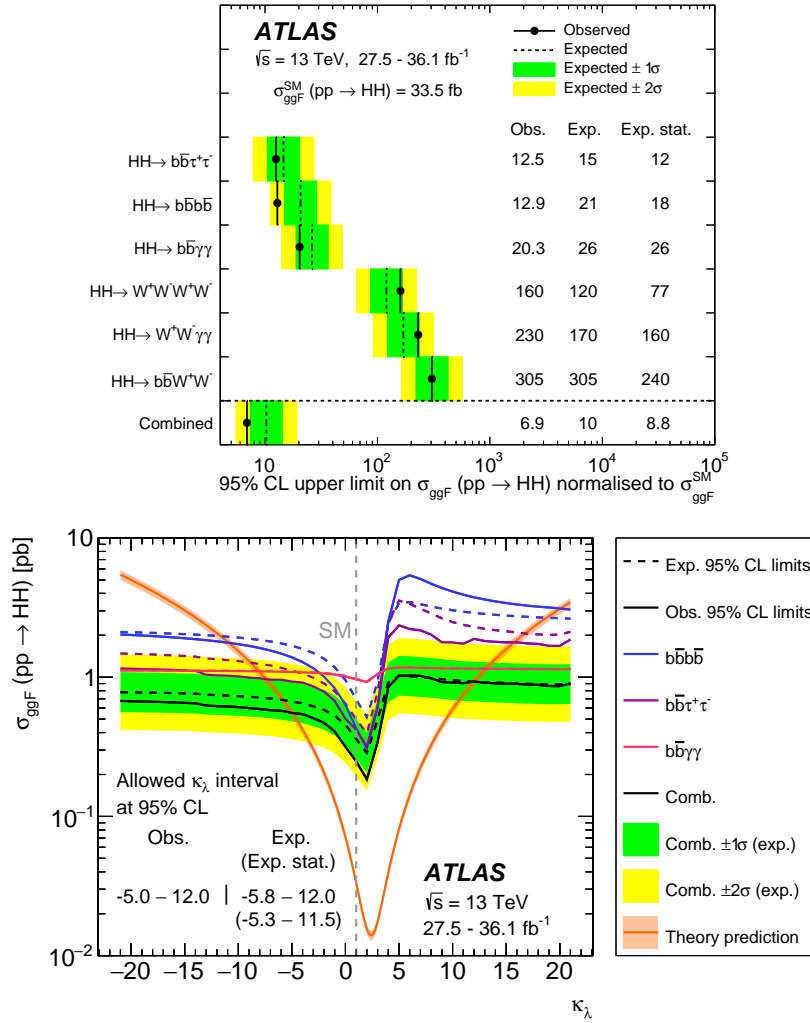
Additionally, we can set the exclusion limit on the production cross-section of the heavy Higgs boson using the results. Figure 2.8 shows the contours of the production cross-section via ggF, σ_{ggF} [fb], times the branching ratio of $H \rightarrow hh \rightarrow b\bar{b}b\bar{b}$ with the mass of the heavy Higgs boson $m_H = 600$ GeV in the Type-II 2HDM. The cross section of the heavy Higgs boson become large in the region of large $\tan\beta$ and small $\sin(\beta - \alpha)$. Figure 2.9 shows the current constraint on the 2HDM in the planes of the mass of the heavy Higgs boson vs. angles ($0.08 < \tan\beta < 50$, and $0.8 < \beta - \alpha < 2.0$ equal to $0.84 < \sin(\beta - \alpha) < 1.0$). Due to the large cross-section of $H \rightarrow hh$ production via ggF in the region of $\tan\beta > 10$ and $\beta - \alpha < 1.0$, the region is excluded by the hh analysis. The region in the $\tan\beta < 1.5$ seems to be excluded for $\beta - \alpha \lesssim 0.5$, comparing to Figure 2.8. The search for the hh production has large contribution in the exclusion. However, there is a room to search for.

2.4.5 New phenomena possible to be observed in hh production via VBF

In the LHC experiment, the hh production in vector boson fusion (VBF) had never been studied. If we focus on that production mode, we can access the quadruple coupling with vector bosons ($VVhh$ coupling) that is able to be a clue for the BSM physics.

Returning to the tree-level Feynman diagrams contributing to the non-resonant Higgs boson pair production via VBF which are shown in Figure 2.5, the coupling strength of κ_{2V} (The ratio of the 4-point $VVhh$ coupling with that in SM), κ_V (The ratio of the three-point VVh coupling with that in SM), and κ_λ (The ratio of the trilinear hhh coupling, λ , with that in SM) are set to 1 in the SM, and a cancellation dictated by perturbative unitarity occurs between the second and third diagrams. For generic values of κ_{2V} and κ_V , the amplitude of the partonic scattering $VV \rightarrow hh$ grows with the partonic center of mass energy $\sqrt{\hat{s}}$ corresponding to the invariant mass of the Higgs bosons (m_{hh}). The leading contribution in the energy range $m_W \ll \sqrt{\hat{s}} \equiv m_{hh}$ comes from the scattering of longitudinal vector bosons (V_L) and is given by

$$\mathcal{A}(V_L V_L \rightarrow hh) \simeq \frac{\hat{s}}{v^2} (\kappa_{2V} - \kappa_V^2), \quad (2.12)$$

Figure 2.7: The upper limit on the cross-section of hh production in ggF, and the λ . [4]

where v is the vacuum expectation value. An analysis of a di-Higgs final state in a VBF topology uniquely provides a constraint on the coupling parameter, κ_{2V} , while the ggF analysis can access to κ_λ and $h \rightarrow ZZ/WW$ analysis can measure κ_V significantly. The cross section of the non-resonant Higgs boson pair production becomes $\mathcal{O}(10)$ times larger with the deviation from the SM hypothesis, $|\Delta\kappa_{2V}| = 1.0$ [10]. Different models of new physics at high scales, such as composite pseudo-Nambu Goldstone Boson theories of the Higgs, predict growth of the $VV \rightarrow hh$ coupling, and this analysis is uniquely sensitive to these signatures [10]. In this study, the parameters of $-4.0 \leq \kappa_{2V} \leq 6.25$ are tested.

We can also access the complementary different parameters in the 2HDM using the hh production via VBF. As mentioned in Section 2.4.3, the heavy Higgs boson is produced via coupling with the vector boson in the VBF, while that is produced via dominant coupling with the top quark in the ggF. As shown in Table 2.4, the behavior of the coupling strength against the vector boson and the top quark are different depending on the angles, α and β . Therefore, the ratio of the cross-section for the VBF and ggF varies in the plane of the angles. Figure 2.10 shows the contours of the ratio of the $\sigma_{\text{VBF}}/\sigma_{\text{ggF}}$ in the 2D plane of $\tan\beta$ and $\sin(\beta - \alpha)$ in the Type-II 2HDM. The production cross-section of the heavy Higgs boson via VBF, σ_{VBF} [fb]

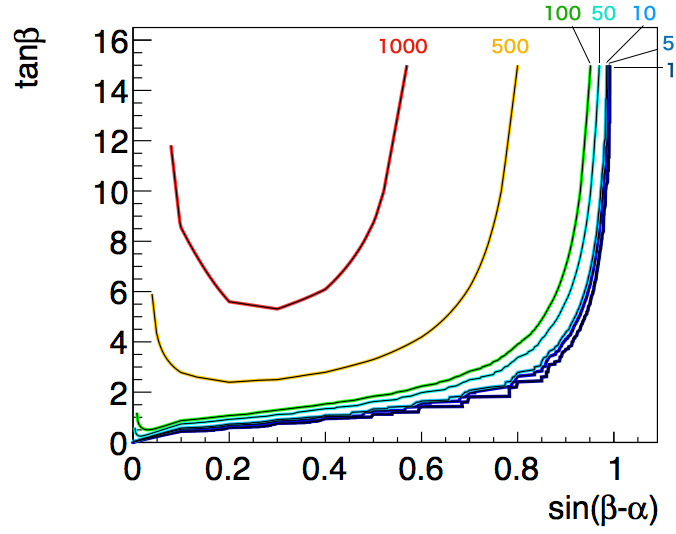


Figure 2.8: The contours of the production cross-section via ggF, σ_{ggF} [fb], times the branching ratio of $H \rightarrow hh \rightarrow b\bar{b}b\bar{b}$ with the mass of the heavy Higgs boson $m_H = 600$ GeV in the Type-II 2HDM. The production cross-section and the branching ratio are calculated using SusHi-1.5.0 [7] and 2HDMC-1.7.0 [8].

and σ_{VBF} times the branching ratio of $H \rightarrow hh \rightarrow b\bar{b}b\bar{b}$ in the Type-II 2HDM are shown in Figure 2.11. σ_{VBF} is large around $\sin(\beta - \alpha) = 0.2$, while the ratio $\sigma_{\text{VBF}}/\sigma_{\text{ggF}}$ is large around $\sin(\beta - \alpha) = 0.8$. Considering the current constraint from the direct searches and the sensitivity, the following parameters are studied as benchmark points: $m_H = 260\text{--}1000$ GeV, $\tan\beta = 2.0$, and $\sin(\beta - \alpha) = 0.6$.

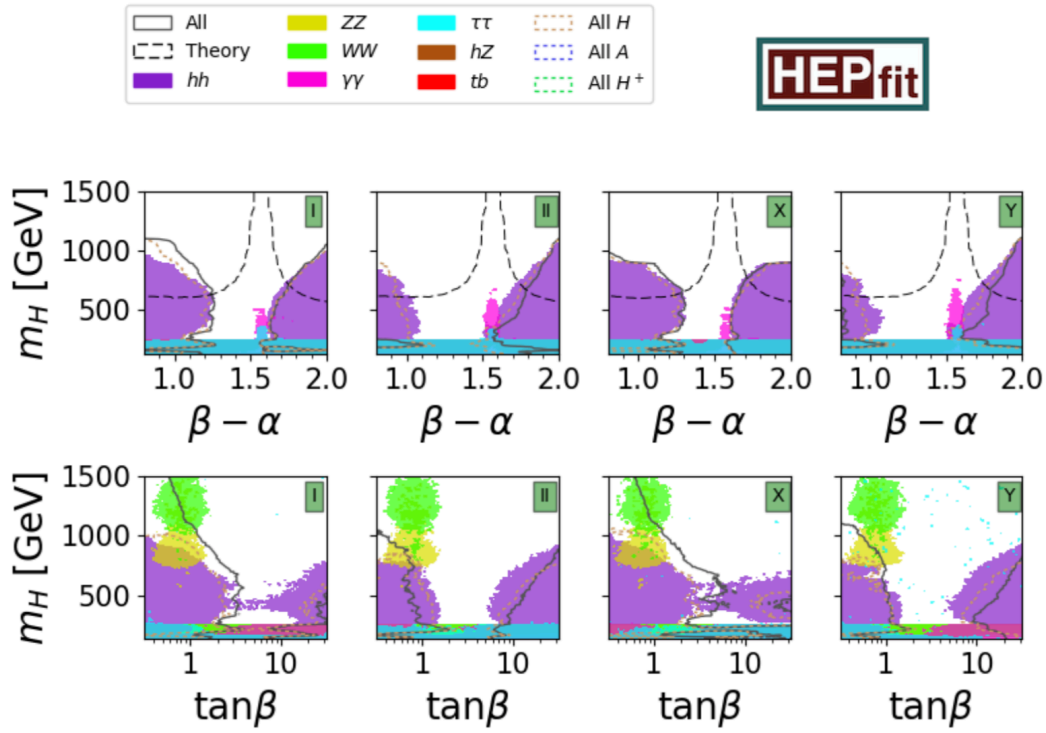


Figure 2.9: In the four types of 2HDM, masses vs. angles planes we display the regions excluded by all heavy Higgs searches with a probability of 95.4% by the central area inside the grey solid line. From left to right, are Type-I, II, X and Y. We compare them with the areas excluded by searches in various final states represented by the colored patches. In the first row the limits from theory constraints are shown by black dashed lines. [9]

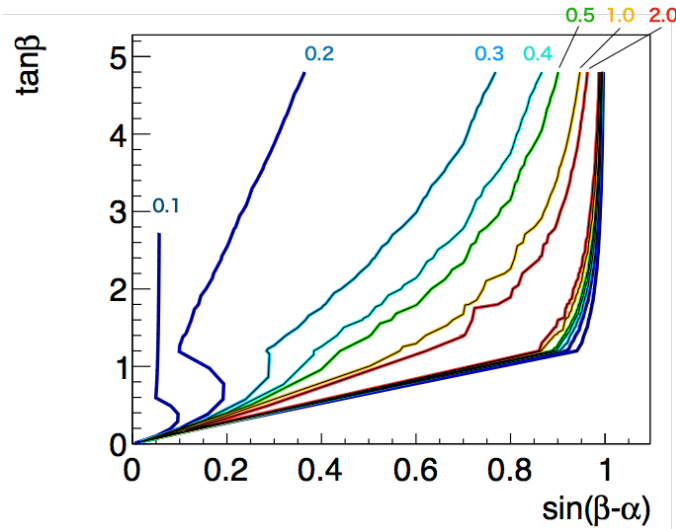


Figure 2.10: The contour of the ratio of the cross-section of the heavy Higgs boson via VBF and ggF, $\sigma_{VBF}/\sigma_{ggF}$, in the Type-II 2HDM. The production cross-section and the branching ratio are calculated using SusHi-1.5.0 [7] and 2HDMC-1.7.0 [8], respectively. The color ordering means, red: 2.0, yellow: 1.0, right green: 0.5, cyan: 0.4, right blue: 0.3, blue: 0.2, dark blue: 0.1.

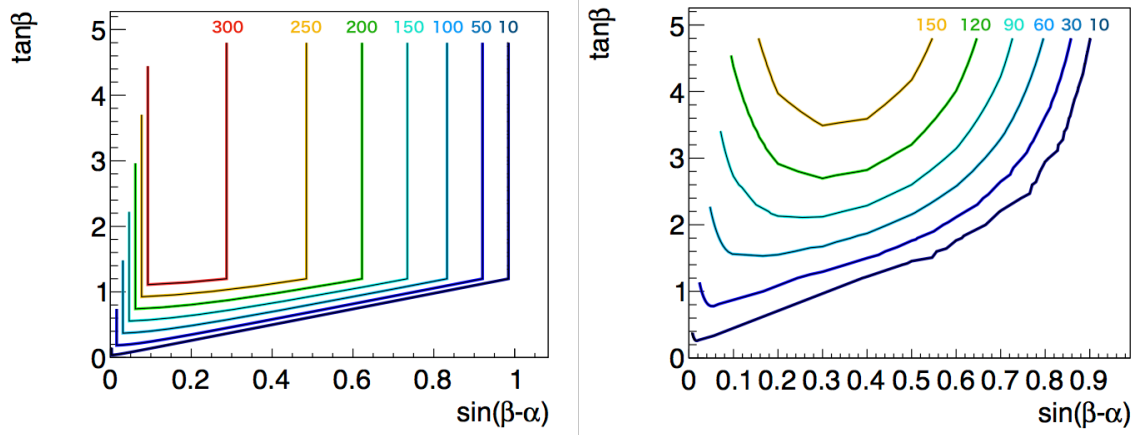


Figure 2.11: The contour of the production cross-section of the heavy Higgs boson via VBF, σ_{VBF} [fb], in the Type-II 2HDM (left) and the contour of the production cross-section via VBF, σ_{VBF} [fb], times the branching ratio of $H \rightarrow hh \rightarrow b\bar{b}b\bar{b}$ in the Type-II 2HDM (right). The production cross-section and the branching ratio are calculated using SusHi-1.5.0 [7] and 2HDMC-1.7.0 [8], respectively.

Chapter 3

LHC-ATLAS experiment

3.1 LHC accelerator

The LHC accelerator is a circular collider of protons with circumference of 26.7 km, which is built straddling the boundary of Switzerland and France. The protons are extracted from the hydrogen atoms and are accelerated in the order of LINAC (50 MeV), BOOSTER (1.4 GeV), Proton Synchrotron (PS ; 25 GeV), Super Proton Synchrotron (SPS ; 450 GeV), and LHC (6.5 TeV) as shown in Figure 3.1. In the LHC, protons are bundled into 2500 bunches, each consists of 1.1×10^{11} protons and the oppositely running bunches collide in 40 MHz with the center-of-mass energy of 13 TeV. The size of the bunch is 8 cm in the direction of the acceleration and $16.7 \mu\text{m}$ in the vertical direction. In results, the instantaneous luminosity of the pp collision reaches about $10^{34} \text{cm}^{-2} \text{s}^{-1}$ ($\sim 40 \text{ MHz} \cdot (1.1 \times 10^{11})^2 / (4\pi \cdot (16 \mu\text{m})^2)$). There are four interaction points in the LHC; ATLAS, CMS, LHCb, and ALICE. ATLAS and CMS are detectors for the general purpose on the measurement of high energy physics. LHCb is a detector for the measurement of the physics of B hadrons. ALICE is a detector for the measurement of the physics in the collision of heavy ions. Table 3.1 shows the LHC beam parameters at the interaction point of the ATLAS detector.

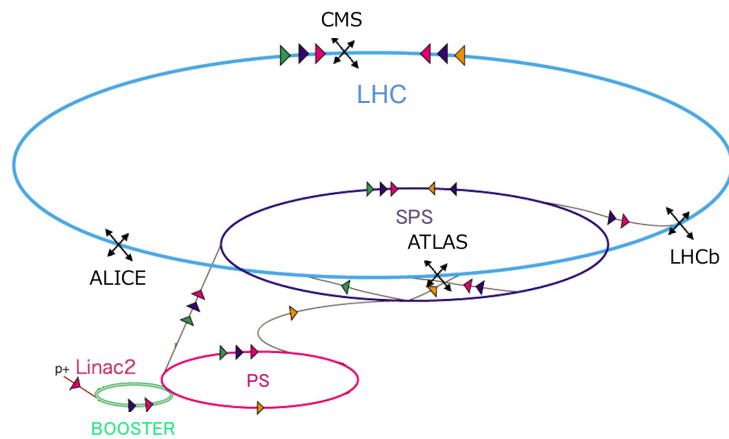


Figure 3.1: The schematic view of the LHC accelerator.

Table 3.1: LHC beam parameters at the interaction point of the ATLAS detector.

	2016	2017	2018
Proton beam energy [TeV]	6.5	6.5	6.5
Luminosity [$10^{-34} \text{ cm}^{-2}\text{s}^{-1}$]	1.3	1.6	1.9
Maximum number of bunches	2208	2544	2544
Number of protons per bunch [10^{11} protons]	1.1	1.1	1.1

3.2 ATLAS detector

Figure 3.2 shows the schematic view of the ATLAS detector. It is a cylindrical detector which is forward-backward symmetric with respect to the interaction point of the proton beams. From inner to outer, the ATLAS detector consists of the inner tracker, the solenoid magnet, the electromagnetic calorimeter, the hadronic calorimeter, the toroidal magnet, and the muon spectrometer. The hadrons, electrons, and muons are identified, and the transverse momentum and energy of them are measured by combining the information from each dedicated detector.

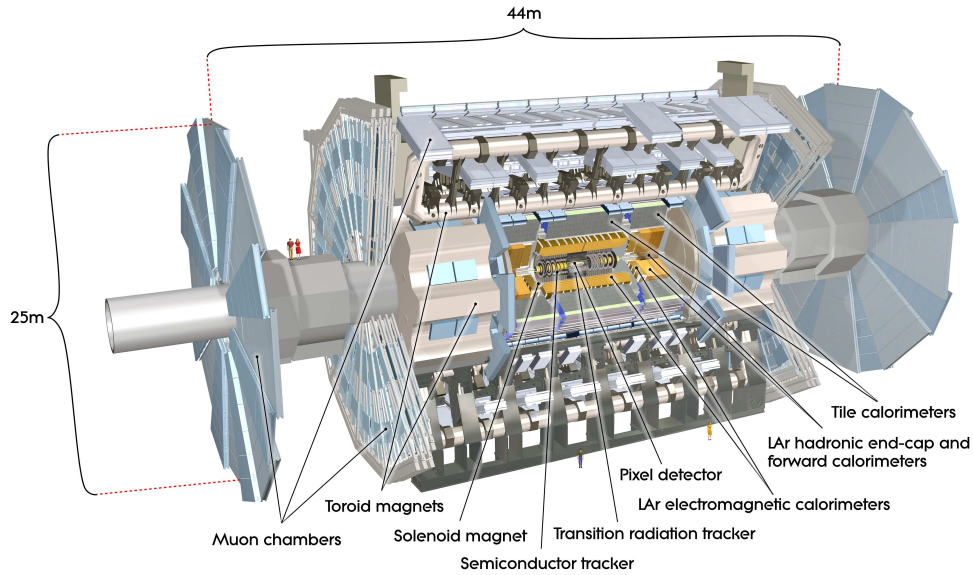


Figure 3.2: The schematic view of the ATLAS accelerator. [11]

The definition of the coordinate system is shown in Figure 3.3. The z -axis is defined along the beam axis, where the positive direction is defined as the counter clockwise of the LHC ring. The positive x -axis is defined in a direction from the origin towards the center of the LHC ring and the positive y -axis is defined as the vertical axis pointing up. The distance from the interaction point in the x - y plane that is vertical with the z -axis is defined as R . The azimuthal angle ϕ is defined with respect to the x -axis and the polar angle θ is defined with respect to the z -axis. In most cases, the pseudo-rapidity, η is used instead of θ :

$$\eta = -\ln \tan(\theta/2) \quad (3.1)$$

The pseudo-rapidity which is defined as the relativistic limit that means the mass of the particle is zero for the rapidity $y = -(1/2) \ln((E + p_z)/(E - p_z))$ (E : the energy of the particle,

p_z : momentum in the z -axis of the particle).

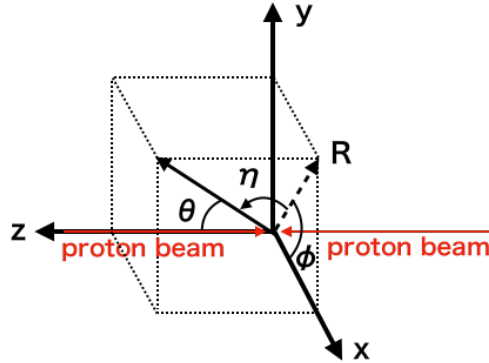


Figure 3.3: The definition of the coordinate system of the ATLAS detector.

3.3 ATLAS sub-detector

3.3.1 Inner tracker

Approximately 1000 particles are emitted from the interaction point of the pp collision every 25 ns within $|\eta| < 2.5$. To reconstruct the tracks of the charged particles near by the interaction point, the inner tracker that consists of Pixel detector, Semiconductor Tracker (SCT), and Transition Radiation Tracker (TRT) is placed inner the solenoid coil. Figure 3.4 shows the schematic view of the pixel detector, SCT, and TRT.

The Pixel detector is a silicon detector. The detector consists of the concentric cylindrical layers in the barrel region ($|\eta| < 2.0$) and disk-shaped layers in the end-cap region ($2.0 < |\eta| < 2.5$). The size of the pixel is $50 \times 400 \mu\text{m}^2$ at minimum. The position resolution is $10 \mu\text{m}$ (ϕ -axis) and $115 \mu\text{m}$ (z -axis) in the barrel region, and $10 \mu\text{m}$ (ϕ -axis) and $115 \mu\text{m}$ (R -axis) in the end-cap region. Typically, the charged particle hits three layers.

The SCT is a silicon detector that consist of strip type semiconductor sensor with 4 layers in barrel region and 9 layers in end-cap region. The pitch of the strip is $80 \mu\text{m}$ in ϕ direction in both of the barrel and the end-cap. The resolution is $17 \mu\text{m}$ (ϕ -axis) and $580 \mu\text{m}$ (z -axis) in the barrel region, and $17 \mu\text{m}$ (ϕ -axis) and $580 \mu\text{m}$ (R -axis) in the end-cap region.

TRT consists of drift tubes with diameter of 4 mm. The gas consists of Xenon (70%), CO_2 (27%), and O_2 (3%), and the charged particle ionize the gas. The intrinsic position resolution is $130 \mu\text{m}$ at the operating voltage of 1530 V. The polypropylene-fiber is spread all over the outer straws as a radiator to distinguish the electron and pion.

The magnetic field of 2 T is applied in z -axis by the solenoid coil to measure the momentum using the radius of curvature of the track. The position resolution of the vertex reconstructed using the tracks is a few $10 \mu\text{m}$ in both of R -axis and z -axis.

3.3.2 Calorimeter

Outside the solenoid magnet, there are the electromagnetic (EM) calorimeter to measure the energy of electrons and photons ($|\eta| < 1.475$ in the barrel region and $1.375 < |\eta| < 3.2$ in the end-cap region) and the hadronic calorimeter to reconstruct the hadron jets ($|\eta| < 1.0$ in barrel region and $1.5 < |\eta| < 3.2$ in the end-cap region). Figure 3.5 shows the schematic view of the calorimeters.

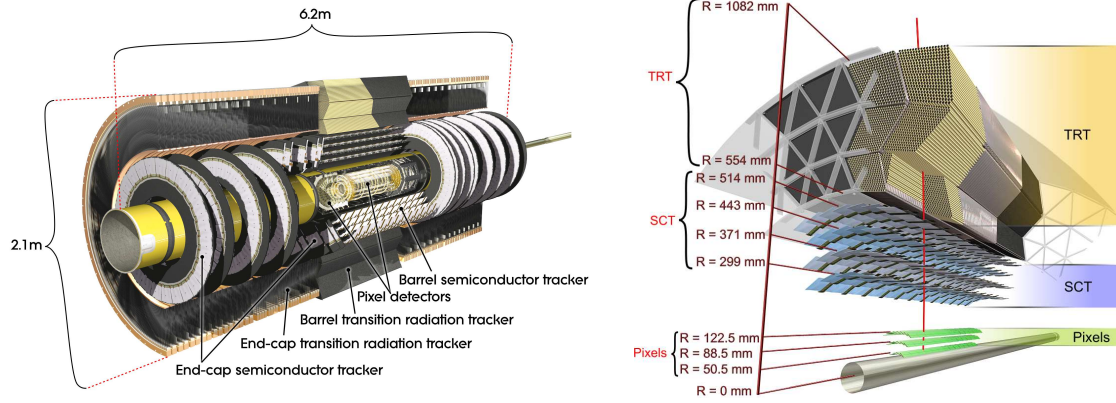


Figure 3.4: The schematic view of the pixel detector, SCT, and TRT. [11]

The EM calorimeter is a sampling calorimeter which uses the accordion shaped lead absorber plates with the thickness of 1.1 mm–2.2 mm and liquid Argon filled between them. The thickness of the EM calorimeter is $20\text{--}30X_0$ (X_0 : radiation length). One channel forms a tower, and the granularity is $\Delta\mu \times \Delta\phi = (0.025\text{--}0.075) \times (0.025\text{--}0.1)$. The electron and photon are distinguished using the shape of the electromagnetic shower. The energy resolution is $\sigma(E)/E = 10\%/\sqrt{E(\text{GeV})} \oplus 0.17\%$.

For the hadronic calorimeter, a tile calorimeter which is a sampling calorimeter using the iron as the absorber and scintillator as the active layer is used in barrel region, and liquid Argon calorimeter is used in the end-cap region. The thickness of the hadronic calorimeter is about 10λ (λ : absorption length). The granularity is $\Delta\mu \times \Delta\phi = (0.1\text{--}0.2) \times (0.1\text{--}0.2)$ and the energy resolution is $\sigma(E)/E = 24\%/\sqrt{E(\text{GeV})}$.

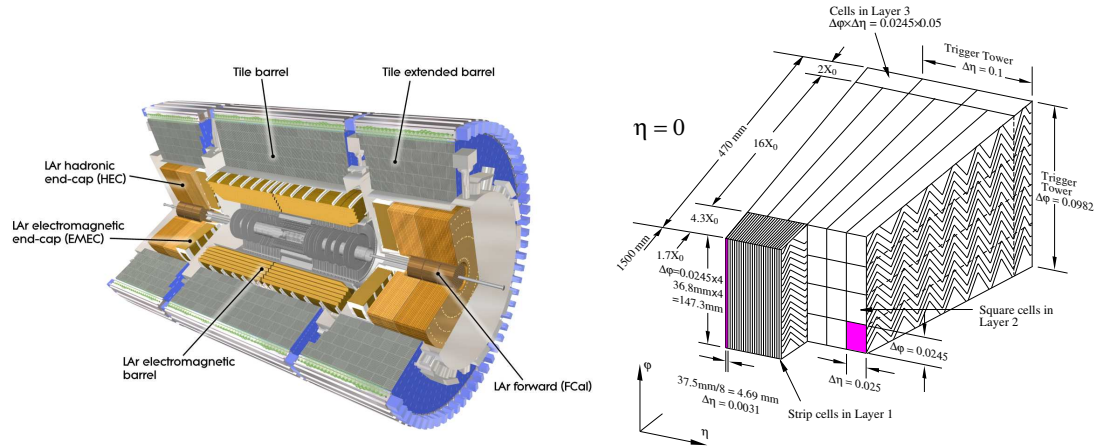


Figure 3.5: The schematic view of the calorimeters. [11] The figure on the left hand-side shows the overview of the EM and hadronic calorimeters. The figure on the right hand-side shows the structure of the EM calorimeter which is a sampling calorimeter based on the accordion shaped lead absorber plates with the thickness of .1 mm–2.2 mm and liquid Argon filled between them.

3.3.3 Muon spectrometer

Outside the calorimeter, there is the muon spectrometer. Figure 3.6 shows the schematic view of the muon spectrometer in the R - z plane. The muon spectrometer consists of Thin Gap Chamber (TGC) and Resistive Plate Chamber (RPC) for the trigger decision at the data taking and Muon Drift Tube (MDT) and Cathode Strip Chamber (CSC) for the precision tracking.

The MDT is an assembly of six parallel layers of drift tubes on a support frame, three layers in the end-cap region and the barrel region. The tubes with their diameter of 30 mm are multi-stacked in a trefoil shape in each layer. Measuring the drift time of the electrons appeared by the ionization of the Argon gas in each tube caused by the muon, the direction of the muon in each layer can be measured. The position resolution of one tube is about $80\ \mu\text{m}$ by position monitoring system of the MDT. The MDT is placed in three layers; Inner ($|z| = 7.5\ \text{m}$ in end-cap region, $|R| = 5\ \text{m}$ in barrel region), middle ($|z| = 13.5\ \text{m}$ in end-cap region, $|R| = 7\ \text{m}$ in barrel region), and outer ($|z| = 21\ \text{m}$ in end-cap region, $|R| = 9.5\ \text{m}$ in barrel region). The tubes are placed in parallel with the ϕ -axis so that the track is reconstructed accurately in the R - η plane.

The maximum available rate of the detection of MDT is $150\ \text{Hz}/\text{cm}^2$. However, the rate of the radiation background of the inner region in $2.0 < |\eta| < 2.7$ exceeds that rate. Therefore, the CSC is used in this region, which is a multi-wire proportional chamber. This detector consists of a layer of the anode wire, parallel to R -axis, and two layers of cathode strip, parallel to R -axis and ϕ -axis respectively. The readout from the cathode strip is executed, and the position resolution is $60\ \mu\text{m}$.

Between the inner and middle layers, a magnetic field of 1.5–5.0 T is applied in ϕ -axis by the toroidal magnet. The resolution of the momentum measurement is 10% for 1 TeV muon.

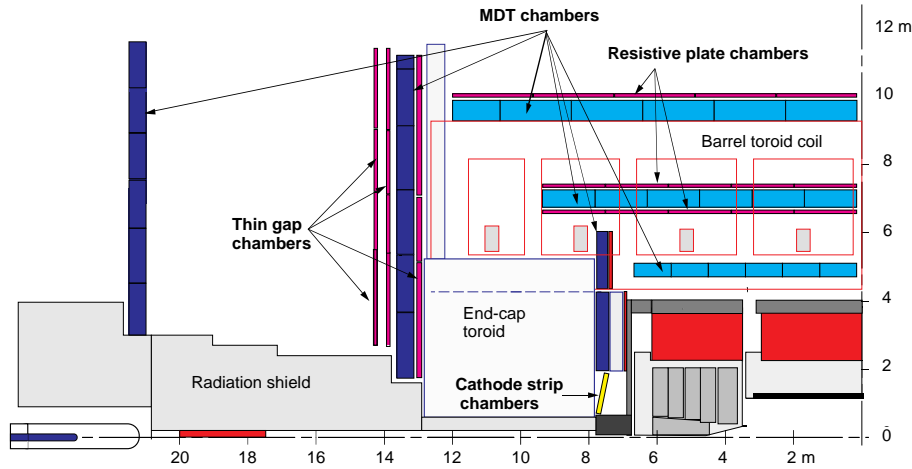


Figure 3.6: The schematic view of the muon spectrometer in the R - z plane.

3.4 Particle Reconstruction

3.4.1 Jet reconstruction

The quarks except for the t -quark are bound into colorless hadrons, which is called as hadronization. Therefore the quarks are detected as groups of the hadrons, called as hadronic jets. The jet reconstruction is performed with anti- k_t algorithm with inputs of the calorimeter clusters. The procedure to find clusters is optimized to suppression of the noise in the calorimeter and the pile-up jets. The first step of the cluster finding is the identification of seeds of cells with

energy deposit $E > 4\sigma$, where σ is the noise level defined as a sum of electronic and pile-up noises in quadrature. The second step is the iterative adjunction of neighboring cells with energy of $E > 2\sigma$ to the seeds. In the third step, an extra layer of cells with $E > 0$ on the perimeter of the clustered cells are added. Splitting algorithm separates the resulting clusters based on local energy maxima. In this way, four-vector (E, p_x, p_y, p_z) is reconstructed assuming the mass of the cluster is zero. The clusters are calibrated to the response from electrons, and such clusters are called as Electromagnetic-energy clusters (EM clusters).

Then the jet finding by the anti- k_t algorithm is performed using the reconstructed clusters. In the anti- k_t algorithm, the following distance between cluster i and j is defined:

$$d_{ij} = \min(p_{T,i}^{-2}, p_{T,j}^{-2}) \frac{\Delta R(i, j)^2}{R^2} \quad (i \neq j) \quad (3.2)$$

$$d_{ij} = p_{T,i}^{-2} \quad (i = j) \quad (3.3)$$

where the $\Delta R(i, j) = \sqrt{(\Delta\eta_{ij}^2 + \Delta\phi_{ij}^2)}$ ($\Delta\eta_{ij}$ and $\Delta\phi_{ij}$ are the difference of η and ϕ between the clusters i and j), and $R = 0.4$ is chosen as the distance within where the jet finding is performed. The d_{ij} of the all clusters are evaluated, and the minimum value of $d_{ij} \equiv d_{\min}$ is sought. If $d_{ij} = d_{\min}$, the i -th cluster and j -th cluster are combined as a k -th jet by adding the four vector ($p_k = p_i + p_j$). If $d_{ii} = d_{\min}$ ($i = j$), the i -th cluster is considered to be a jet, and the cluster is removed the list of the cluster candidates. This process is repeated until all cluster are removed from the list of the cluster candidates.

While the clusters are calibrated to the response from electrons, the reconstructed jet energy are calibrated using the relation between the reconstructed jets and truth-jets before the reconstruction in Monte Carlo (MC) simulated QCD multi-jet events.

3.4.2 b -tagging

In this analysis, we focus on the events that four b -quarks are emitted from the decay of two Higgs bosons in the final states. To identify the hadronized b -jets, we use the characteristic property of the lifetime of the b -hadron ($c\tau \sim 420\mu\text{m}$, where c is speed of light and τ is the lifetime) that means the distance between the primary vertex of the b -hadron production and the second vertex of the b -hadron decay is adequately measurable.

The b -tagging is performed using so-called MV2 algorithm based on the Boosted Decision Tree (BDT) with inputs of the impact parameter based algorithm (IP3D), Secondary Vertex finding algorithm (SV), and decay chain multi-vertex algorithm (JetFitter). The details of these four algorithms are described below.

IP3D

The typical b -hadron topology is characterized by at least one vertex displaced from the point where the hard-scatter collision takes place. The IP3D algorithm uses two parameters: (1) d_0 defined as the distance of closest approach in the R - ϕ plane of the track to the primary vertex, (2) $z_0 \sin \theta$ defined as the distance of the track to the primary vertex in the longitudinal plane at the point of closest approach in R - ϕ . This algorithm calculates the log likelihood ratio for b and other flavor hypotheses, and it discriminates between a b -jet and another flavor jet.

SV

The secondary vertex finding algorithm explicitly reconstructs an inclusive displaced secondary vertex within the jet. This algorithm reconstructs the two-track vertex for all track pair candidates. Any two-track vertices which are likely originated from the decay of K_S and Λ , photon

conversions, and the hadronic interactions with the detector material are rejected. If a two-track vertex remains, a new vertex is then fitted with all tracks from the accepted two-track vertices, where outliers are iteratively removed from this set of tracks.

JetFitter

The decay chain multi-vertex reconstruction algorithm, JetFitter, exploits the topological structure of weak b - and c -hadron decays inside the jet and reconstructs the full b -hadron decay chain. Kalman filter is used to find a common line on which the primary vertex and the bottom and charm vertices lie, approximating the b -hadron flight path, as well as their positions.

MV2

The b -jets and the other-flavor jets are discriminated by using a multivariate analysis called MV2 algorithm that is based on the BDT to achieve a better discrimination than any of the basic algorithms can exploit individually. The training of the multivariate classifier is performed on jets from $t\bar{t}$ events with b -jets (1 million) being considered as signal, and c - (0.5 million) and light-flavor jets (1 million) being considered as background. The performance is tested on an independent sample of 5 million events. Figure 3.7 shows the BDT output evaluated with $t\bar{t}$ events.

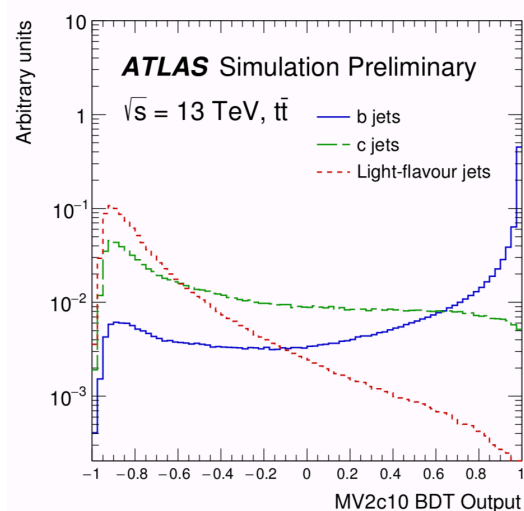


Figure 3.7: BDT output for b - (solid blue), c - (dashed green) and light-flavor (dotted red) jets evaluated with $t\bar{t}$ events. [12]

3.4.3 Muon reconstruction

Focusing on the final state of $hh \rightarrow b\bar{b}b\bar{b}$, the muons are emitted from the semi-leptonic decay of the b -hadrons. The muon reconstruction is first performed independently in the inner detectors (ID) and the muon spectrometers (MS). The information from individual sub-detectors is then combined to form the muon tracks that are used in physics analyses.

Muon reconstruction in the MS starts with a search for hit patterns inside each muon chamber to form segments. The MDT segments are reconstructed by performing a straight-line fit to the hits found in each layer. The RPC or TGC hits measure the coordinate orthogonal to the bending plane. Segments in the CSC detectors are built using a separate combinatorial search

in the η and ϕ detector planes. Muon track candidates are then built by fitting together hits from segments in different layers.

In the ID, the track of the charged particle is reconstructed from Pixel hits, SCT hits, and drift circles on TRT straw tubes. Then, the MS standalone muon and ID trackers are combined by interpolating the MS standalone muon track to the interaction points.

3.4.4 Electron reconstruction

Electromagnetic-energy cluster (EM cluster) candidates are seeded from localized energy deposits of size 3×5 towers in $\eta \times \phi$, whose summed transverse energy exceeds 2.5 GeV. The electron candidate requires the cluster with one track that satisfies $|\eta_{\text{cluster}} - \eta_{\text{track}}| < 0.5$ and $-0.10 < \Delta\phi < 0.05$. The electron identification uses the following parameters: (1) Hadron leakage defined by the ratio of E_T in the first layer of the hadronic calorimeter to E_T of the EM cluster, (2) Shower shape that is defined using the width and lateral energy deposit distribution using the first layer and the second layer of EM calorimeter, (3) Track conditions that contains number of hits in the ID and transverse impact parameter, (4) Likelihood probability based on transition radiation in the TRT, (5) Track cluster matching quality of $\Delta\eta$ and $\Delta\phi$ of the cluster and track, and the ratio of the cluster energy to the track momentum.

3.5 Data taking

3.5.1 Trigger

At the LHC-ATLAS experiment, about 20–60 pair of protons interacts per one bunch-crossing, where the rate of the bunch crossing is 40 MHz. That means the event rate exceeds 1 GHz. The data size of an event is about 1.5 MB. However, the available rate of the data recording is 300 MB/s. Because of that, the trigger system is needed to reduce the data recording rate up to $O(100)$ Hz with keeping the efficiency of the interesting events high enough.

The pile-up events are typically low energy interactions which we are not interested in from the point of view of the new physics searches or the precision measurements of Higgs boson, top quark, and electroweak physics. Therefore, we select the events using the momentum of the particles in the final states. To achieve the rate reduction of factor 10^5 , we use three stages of the trigger: level-1 (reduces to about 75 kHz), level-2 (reduces to about 1 kHz), Event-filter (reduces to about 100 Hz) as shown in Figure 3.8. The level-1 trigger is a hardware-based trigger which can select the specific events from the enormous number of events. The level-1 trigger decision is made if there is high p_T leptons or jets in the events based on the information of the muon trigger detectors (TGC and RPC) and the calorimeters. The level-2 trigger and the Event-filter are based on the software that reconstructs the muon and jets using combination of the detectors and measure the momentum precisely.

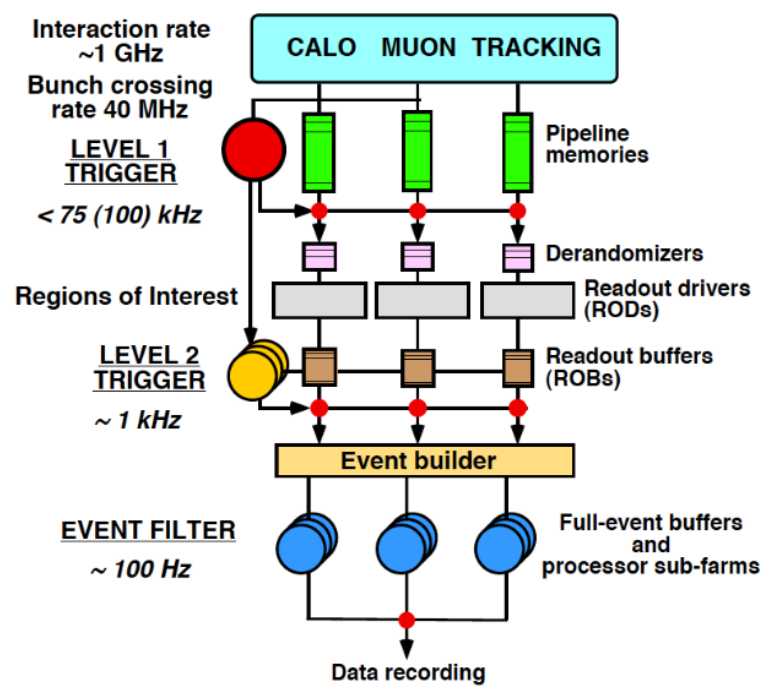


Figure 3.8: The schematic view of the trigger. [13]

Chapter 4

Search for the hh production in vector boson fusion

4.1 Signal and backgrounds

4.1.1 Signal topology

The signal of our interest has the topology like Figure 4.1. The Higgs bosons tend to be emitted in low $|\eta|$ region, while the light-quark jets (VBF jets) associated with the hh production distribute in high $|\eta|$ region.

4.1.2 Backgrounds

We have the background events whose the topology is similar to that of the signal. The most dominant background is the QCD multi-jet background that is produced by the strong interaction of qq , qg , and gg in the pp collision like the diagram in Figure 4.2. The secondary dominant background is $t\bar{t}$ production whose diagram is shown in Figure 4.3.

4.2 Collision data and used triggers

This analysis uses the collision data collected in 2016, 2017 and 2018 with $\sqrt{s} = 13$ TeV by the ATLAS detector. The amount of data is quantified by the integrated luminosity L , which is denoted using the total number of events N and the cross section of pp collision σ as,

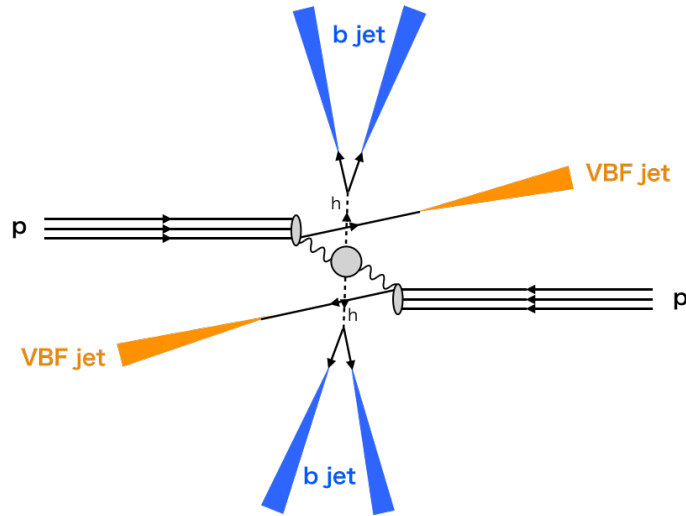
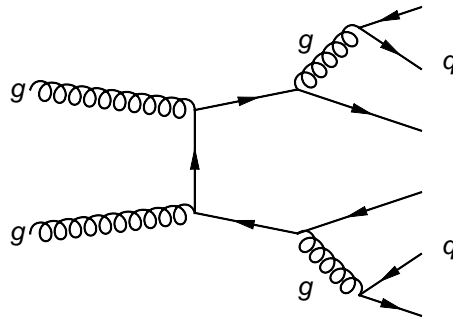
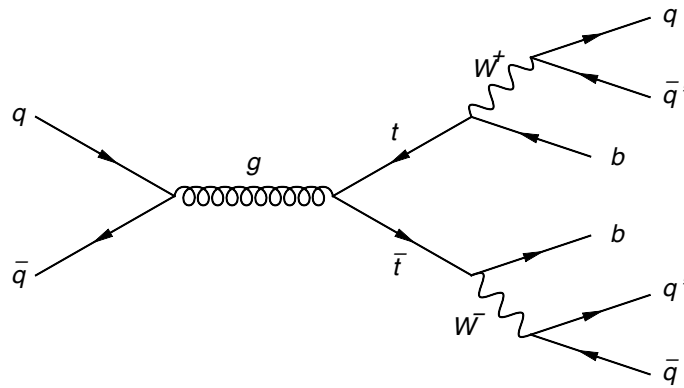
$$L = \int \mathcal{L} dt = \int \frac{N}{\sigma} dt \quad (4.1)$$

where \mathcal{L} is the instantaneous luminosity measured at specific time. The instantaneous luminosity can be written as

$$\mathcal{L} = \frac{\mu n_b f_r}{\sigma_{\text{inel}}} \quad (4.2)$$

where μ is the average number of inelastic interactions per bunch crossing, f_r is revolution frequency of the LHC ($= c/l_{\text{ring}} = 3 \times 10^8[\text{m/s}]/26659[\text{m}] = 11253[\text{Hz}]$, where c is the speed of light and l_{ring} is the circumference length of the LHC), n_b is number of bunch pairs colliding per revolution, and σ_{inel} is the pp inelastic cross-section.

The measurement of the interaction rate μ is derived from randomly-sampled colliding-bunch crossings, where only the data from the SCT and pixel detectors are read out, and the cross


 Figure 4.1: The topology of the VBF hh production.

 Figure 4.2: The diagram of the QCD multi-jet background. This diagram is the case that is initiated with the strong interaction of gg interaction. Other than this diagram, there are processes initiated with the strong interaction of qq and $q\bar{q}$.

 Figure 4.3: The diagram of the $t\bar{t}$ background.

section σ_{inel} is measured in the Van der Meer scan. The integrated luminosity is measured with 1.7% uncertainty [14].

The signal has $4b$ -jets in the final state. Therefore, a combination of multi- b -jet triggers generated by the High Level Trigger (HLT) performed in two stages of the Level-2 trigger and the Event Filter is used at the data taking. The used triggers in 2016, 2017, and 2018 are listed in Table 4.1, Table 4.2, and Table 4.3. The MV2 cut for the b -tagging at the trigger is selected so that the b -tagging efficiency become 60% for the b -jets. Combined, they provide high overall efficiency throughout the mass region searched which will be discussed in the Section 4.5. The b -jet trigger menu differs in 2016, 2017, and 2018, so as a result, the data periods are treated separately. A good quality of data taking depending on the status of each detector is required, then the total luminosity used in this analysis is 126.0 fb^{-1} .

Table 4.1: Investigated 2016 triggers. **bXX** indicates a b -tag, at the XX% working point of b -tagging efficiency that the online b -tagging performed in the stage of HLT, on the number of jets specified by the proceeding YjZ, where Y indicates the number of jets and Z the p_T threshold.

triggers	description
HLT_2j35_b60_2j35	2 b -tagged jets ($p_T > 35 \text{ GeV}$, b -tag WP: 60%), 2 jets ($p_T > 35 \text{ GeV}$)
HLT_j100_2j55_b60	2 b -tagged jets ($p_T > 55 \text{ GeV}$, b -tag WP: 60%), 1 jet ($p_T > 100 \text{ GeV}$)
HLT_j225_b60	1 b -tagged jet ($p_T > 225 \text{ GeV}$, b -tag WP: 60%)

Table 4.2: Investigated 2017 triggers. **bXX** indicates a b -tag, at the XX% working point of b -tagging efficiency that the online b -tagging performed in the stage of HLT, on the number of jets specified by the proceeding YjZ, where Y indicates the number of jets and Z the p_T threshold.

triggers	description
HLT_2j35_b40_2j35	2 b -tagged jets ($p_T > 35 \text{ GeV}$, b -tag WP: 40%), 2 jets ($p_T > 35 \text{ GeV}$)
HLT_j150_2j55_b70	2 b -tagged jets ($p_T > 55 \text{ GeV}$, b -tag WP: 70%), 1 jet ($p_T > 150 \text{ GeV}$)

Table 4.3: Investigated 2018 triggers. **bXX** indicates a b -tag, at the XX% working point of b -tagging efficiency that the online b -tagging performed in the stage of HLT, on the number of jets specified by the proceeding YjZ, where Y indicates the number of jets and Z the p_T threshold.

triggers	description
HLT_2j35_b40_2j35	2 b -tagged jets ($p_T > 35 \text{ GeV}$, b -tag WP: 40%), 2 jets ($p_T > 35 \text{ GeV}$)
HLT_j150_2j55_b70	2 b -tagged jets ($p_T > 55 \text{ GeV}$, b -tag WP: 70%), 1 jet ($p_T > 150 \text{ GeV}$)

4.3 MC simulations

4.3.1 Signal MC production

The MC signal samples of the heavy Higgs boson have been generated for 10 mass points of m_H from 260 to 1000 GeV using Powheg-Box v2 [15, 16, 17] interfaced to Pythia 8.186 for

parton shower and hadronization, with the Higgs boson mass, m_h , fixed to 125.0 GeV. The NNPDF23_lo parton distribution function (PDF) set [18] and the A14 set of tuned parameters [19] for underlying-event simulation were used. Table 4.4 shows the cross-section and branching ratio of the samples that are generated in the context of an extended Higgs sector, using the Type-II 2HDM. The width of the heavy Higgs boson (Γ_H) is chosen for the parameters of ($\tan\beta = 2.0$ and $\sin(\beta - \alpha) = 0.6$). The samples of heavy Higgs boson with narrow width (4 MeV) for inclusive search are generated with same conditions.

Table 4.4: The tested cross-section (σ), branching ratio (BR), and the width of the heavy Higgs boson (Γ_H) for the signal MC samples as a function of the heavy Higgs boson mass.

m_H (GeV)	Γ_H (GeV)	$\sigma(pp \rightarrow Hjj) \times \text{BR}(H \rightarrow hh)$ (fb)	$\text{BR}(h \rightarrow bb)$ (%)
260	3.110	47.45	71.6
280	4.381	76.96	71.6
300	5.924	90.62	71.6
400	19.60	84.08	71.6
500	44.51	60.97	71.6
600	81.67	44.12	71.6
700	133.6	32.15	71.6
800	202.7	23.66	71.6
900	291.7	12.87	71.6
1000	403.0	6.974	71.6

The samples of the non-resonant signal are listed in Table 4.5. The parameters of $\kappa_\lambda = 1$, $\kappa_{2V} = 1$, and $\kappa_V = 1$ corresponds to the SM. Non-resonant production of Higgs boson pairs was simulated with MadGraph5_aMC@NLO. The samples were generated at LO. The VBF production cross-section of non-resonant SM signal used is evaluated at next-to-next-to-next-to-leading order (N3LO) in QCD: $\sigma(pp \rightarrow hhjj) = 1.723^{+0.03\%}_{-0.04\%} \pm 2.1\%$ fb [20]. The N3LO to LO cross-section ratio at the SM value is 1.723 fb/1.639 fb and this factor is applied to the cross-sections at each κ_{2V} point.

Table 4.5: List of the tested cross-section and branching ratio for the non resonant MC samples. As a reminder, κ_{2V} is the ratio of the 4-point $VVhh$ coupling with that in SM, κ_V is the ratio of the three-point VVh coupling with that in SM, and κ_λ is the ratio of the trilinear hhh coupling, λ , with that in SM.

κ_λ	κ_{2V}	κ_V	$\sigma(pp \rightarrow hhjj)$ [fb]	$\text{BR}(h \rightarrow bb)$ (%)
1.0	0.0	1.0	18.71	58.2
1.0	0.5	1.0	6.765	58.2
1.0	1.0	1.0	1.723	58.2
1.0	1.5	1.0	2.836	58.2
1.0	2.0	1.0	10.88	58.2
1.0	4.0	1.0	109.6	58.2

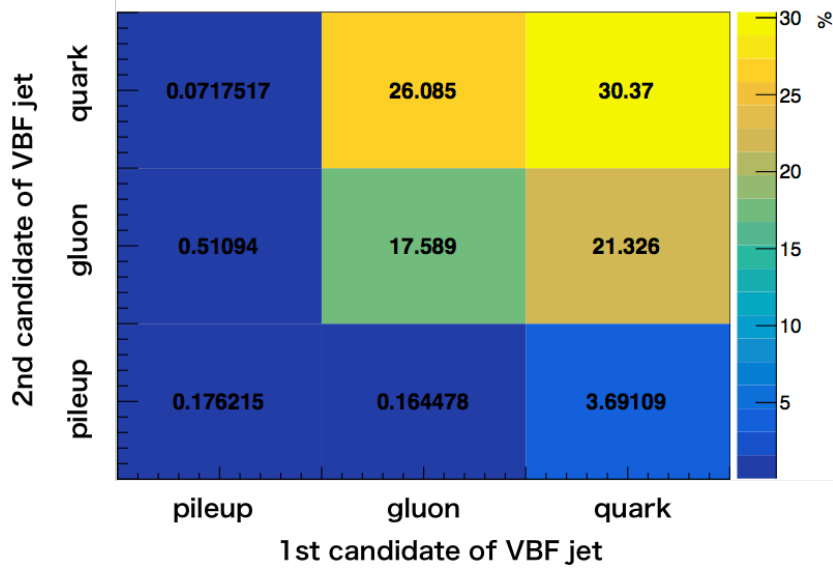


Figure 4.4: Origin of the additional selected VBF jets from the ggF sample. In the MC, when the $\Delta R = \sqrt{\Delta\eta^2 + \Delta\phi^2}$ where the $\Delta\eta$ and $\Delta\phi$ are the difference of the η and ϕ between the each VBF jet after the hadronization and the partons before the hadronization is less than 0.4, the corresponding parton is categorized as origin of the VBF jets. Each jet is labeled as coming from pileup, a gluon, or a quark. The normalization is arbitrary.

4.3.2 ggF contamination

The contamination from the events of hh production via ggF can also happen because of final state radiation, extra matrix-element jets, or pileup jets. At the SM value of the di-Higgs process (i.e. $\kappa_{2V} = 1$), the ggF signal has a 15 times higher cross-section than the VBF process. Our signal selection significantly which is described in Section 4.6 enhances the VBF signal over the ggF signal. However, the ggF yield is still expected to be 3 times higher than the VBF yield. The SM non-resonant production of Higgs boson pairs via ggF was simulated with MadGraph5_aMC@NLO at next-to-leading order (NLO) using the CT10 PDF set [21] and the FTAapprox method [22] to consider the effect of finite top-quark mass on the kinematics of the system rather than infinite top-quark mass approximation. Parton shower and hadronization were simulated with Herwig 7.0.4 [23]. The cross-section of the SM non-resonant production of Higgs boson pairs via ggF is evaluated at next-to-next-to-leading order (NNLO) with the FTAapprox method, it is equal to 31.05 fb.

Figure 4.4 shows origin of the jets selected as VBF jets in Figure 4.1 from the ggF sample. The jet is defined as a “truth jet” which is reconstructed using the anti- k_t algorithm with $R = 0.4$ before the simulation of the reconstruction by the detectors. The selection criteria is 2 jets of $|\eta| < 2.0$, $p_T > 30$ GeV and they have opposite sign of η , as summarized in Section 4.6. 70% of the events are in the non-quark-quark category; these events, since they have a different final state than the VBF signal, have no chance of interfering with the signal. The sample is generated with only one additional radiation in the matrix element, so the extra jets even in the quark-quark case must come from Final State Radiation (FSR), where again the interference is minimal. Therefore, the ggF contamination is taken as a background, since the signal we are searching for is the VBF process explicitly.

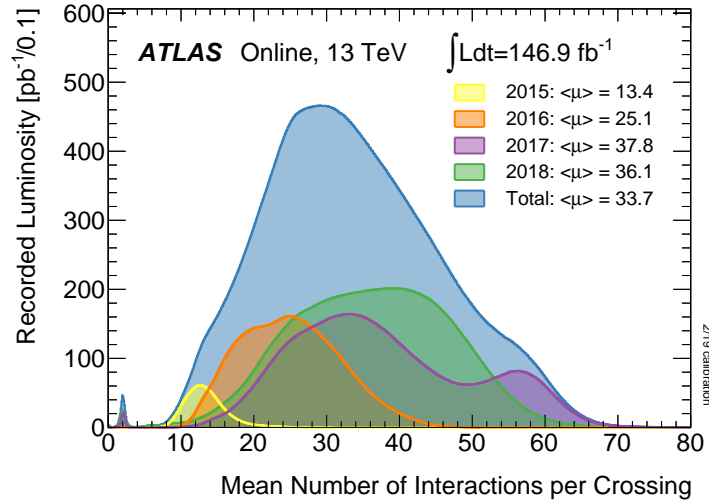


Figure 4.5: Number of Interactions per Crossing in each year. [29]

4.3.3 The samples for the background estimation

The dominant QCD multijet background (about 95% of total) is estimated using data. The details of the estimation procedure can be found in Section 4.7.

The second largest background, but much smaller contribution, arises from $t\bar{t}$ production. The $t\bar{t}$ background is modeled using large all-hadronic and non all-hadronic decay mode samples that have both been generated with Powheg and showered with PYTHIA 8. The top mass in both samples is set to 172.5 GeV. The prediction of the $t\bar{t}$ MC samples are normalized to the inclusive $t\bar{t}$ cross-section of 832^{+46}_{-51} pb [24] predicted by the NNLO with with the resummation at next-to-leading-logarithm (NLL) accuracy and multiplied by the all-hadronic branching ratio of 0.457 and non all-hadronic of 0.543 respectively.

4.3.4 Pile-up events implemented in the MC samples and the detector simulation

For all simulated events, c -hadron and b -hadron decays were handled by EvtGen 1.2.0 [25]. To simulate the impact of multiple pp interactions that occur within the same or nearby bunch crossings (pile-up), the events generated by Pythia 8.186 using the A2 set of tuned parameters [26] are overlaid on the hard-scatter process. The number of the interactions per bunch crossing is different among the years, due to the difference of the configuration of the proton bunch and the structure of the bunch train. The MC samples are generated with the pile-up events with reference to the measured number of that in each year as shown in Figure 4.5. The MC samples are generated and treated independently among the years.

After event generation and the addition of pileup, the response of particles passing through the detector elements is simulated with the GEANT4 toolkit [27, 28] and events are reconstructed using the same software used to reconstruct events in data.

4.4 Jet energy correction and jet selections

4.4.1 The b -jet energy regression

This analysis uses the jets that reconstructed using anti- k_t algorithm. These jets are formed from topological clusters of energy reconstructed in the calorimeter. The topological clusters are calibrated at the electromagnetic scale and formed into jets using a distance parameter of $R = 0.4$ using the anti- k_t algorithm. However, various effects impact the jet energy measurement because of the following effects:

- The neutrino is emitted from the leptonic decay of the B -hadron which forms b -jets. However, the neutrino cannot be detected and the b -jet energy is mis-measured by the missing energy. Since the branching fraction of the leptonic decay of the B -hadron is 30%, the resolution of the b -jet energy may be worth by this effect.
- Some decay particles from the decay of the B -hadron leak the out of cone $R = 0.4$. The decay products of the low energy b -jets tend to be spread in the plane $\eta \times \phi$ and the resolution of such b -jets would be worth because of the out-of-cone leakage.

These effects are not considered in the default ATLAS calibration procedure that is described in Section 3.4.1. In this analysis, we use the jet energy regression that is designed to correct the calibrated b -jet energy to account for the mis-measurements relevant for the b -jets and not considered in the default ATLAS calibration procedure. In the jet energy regression, we use a multivariate algorithm, Boosted Decision Trees (BDTs) provided by TMVA [30], to improve the b -jet energy scale and resolution.

Jets referred to as truth jets are reconstructed using the anti- k_t algorithm with $R = 0.4$ using stable final-state particles from MC generators as input. Candidate particles are required to have a lifetime greater than 10 ps. Neutrinos, electrons and muons as well photons associated to electrons and muons are not included except they stem from hadrons. Truth jets with $p_T > 20$ GeV and $|\eta| < 2.5$ are used. Reconstructed calorimeter jets are geometrically matched to truth jets. Muons reconstructed from a combination of measurements from the ID and the muon spectrometer are used to account for the uncaptured jet energy carried by high energy particles passing through the calorimeters without being fully absorbed.

In the BDT, the truth b -jets clustered from truth particles are used to define the target as a correction factor of the momentum. The ratio of the truth jet transverse momentum p_T^{truth} and the reconstructed jet transverse momentum p_T^{reco} is taken as target which is used to scale the momenta of reconstructed jets:

$$C = \frac{p_T^{\text{truth}}}{p_T^{\text{reco}}}. \quad (4.3)$$

Following variables are used as input to the BDT training to derive C :

- jet $\log(p_T)$: allows to take into account the momentum dependence of the jet mass resolution.
- jet MV2 score: is b -tagging discriminant that allows to tag the jet flavor.
- jet width: defined as the average p_T weighted distance ΔR of jet constituents j_i from the jet axis a :

$$\text{width} = \frac{\sum_{j_i} \Delta R(a, j_i) p_T^{j_i}}{\sum_{j_i} p_T^{j_i}}. \quad (4.4)$$

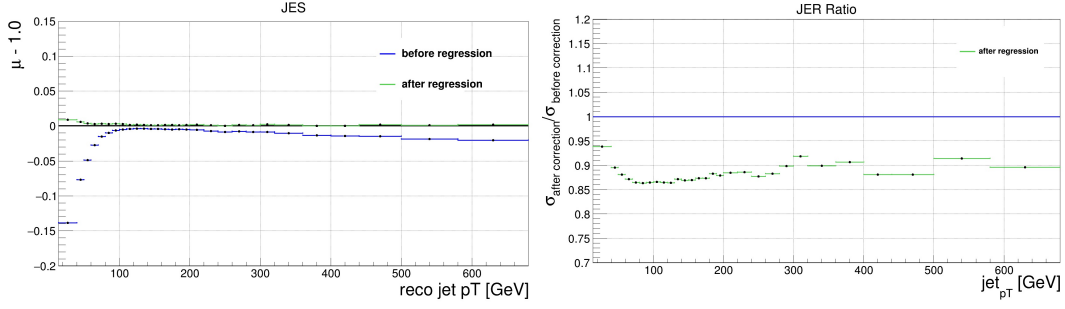


Figure 4.6: The b -jet energy scale (left) and energy resolution (right) as a function of the reconstructed jet p_T . The blue is the case before the b -jet energy regression is applied and the green is the case after the b -jet energy regression is applied.

The jet width is a measure of how collimated the jet constituents are within the jet. Jets with a large width could suffer from out-of-cone leakage because not all decay products will be caught within the jet cone and the energy of the original parton will be underestimated.

- p_T fraction: carried by tracks associated to the jet is defined as a scalar sum of transverse momenta of associated tracks divided by the jet p_T . On average 2/3 of the b -jet energy is carried by the charged particles, thus the transverse momentum of tracks is directly proportional to the b -jet p_T . In addition, the track p_T resolution at low momenta is better than calorimeter-based jet energy resolution.
- jet vertex discriminant: allows to distinguish between pile-up and hard-interaction jets.
- sum of close-by jets p_T 's: is the scalar sum of the transverse momenta of jets found within $0.4 < \Delta R < 1.0$ around the jet axis. It is a measure of the amount of hard radiation from the original parton.
- sum of lepton or muon p_T 's in jets: is a direct measure of energy from leptonic hadron decays. In case of muons, their energy is not accounted in the jet energy calculation and that has the largest effect on the underestimation of the original parton. Energy of electrons is considered in the jet energy calculation but not the energy of the escaping neutrinos. We use scalar p_T sum of muons in $\Delta R < 0.4$ as sum of muon p_T 's in jets and scalar p_T sum of electrons and muons in $\Delta R < 0.4$ as sum of lepton p_T 's in jets.

The sample for the training consists of about 8.6 million truth matched b -jets from $t\bar{t}$ decays. The $t\bar{t}$ sample with the final state of the non-all-hadronic was used. About 80% of jets are used for the BDT training and 20% for the performance evaluation. Note that the largest MC background is the all-hadronic contribution, there is no overlap between the training and evaluation dataset for the most important background.

The performance of the b -jet energy regression is evaluated by comparing the reconstructed b -jet transverse momentum and the truth b -jet transverse momentum. The reconstructed jet p_T is corrected by the b -jet regression correction factor C defined in Equation 4.3. Figure 4.6 shows the jet energy scale (μ) and the jet energy resolution as a function of the reconstructed jet p_T . The jet energy scale μ defined as the ratio of the reconstructed jet p_T to the truth jet p_T is almost at 1 after the application of regression over the whole p_T range. The jet energy resolution (σ) is improved by about 10%.

The impact of the b -jet regression on the reconstructed mass of the Higgs boson decaying into two b -quarks is tested using the $hh \rightarrow b\bar{b}b\bar{b}$ process. Figure 4.7 shows the ratio of the signal yields of $m_H = 400$ GeV with narrow width (4 MeV) and total background yields with the invariant

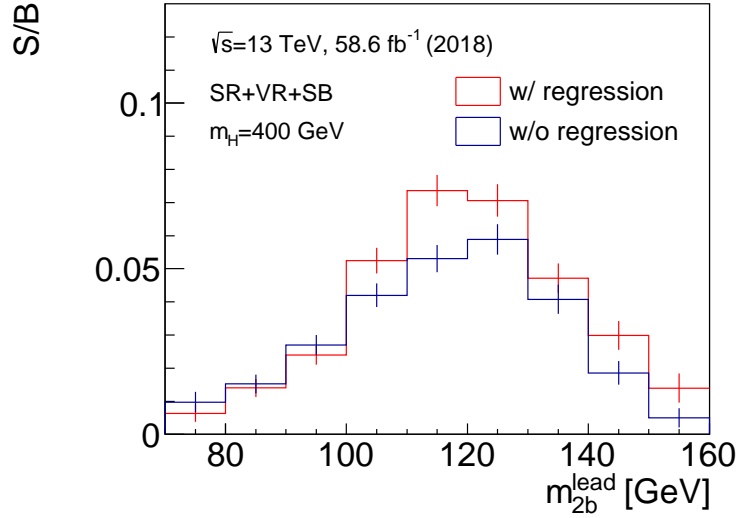


Figure 4.7: The ratio of the signal yields and the background yields with the invariant mass of two truth matched b -jets, m_{bb} , from $H \rightarrow hh \rightarrow b\bar{b}b\bar{b}$ decays. The mass of the heavy particle H with narrow width (4 MeV) is 400 GeV. The yields are normalized to the corresponding dataset of 58.6 fb^{-1} taken in 2018. At the bin of $110 < m_{bb} < 120$, the ratio of the signal yields and the background yields improved by about 40%.

mass of the Higgs candidates with leading momentum. At the mass peak position, the ratio of the signal yields and the background yields improved by about 40% of the case without the b -jet energy regression.

4.4.2 Selection for the jets

The selections for the jets are summarized in Table 4.6. Jets containing b -hadrons are identified with 70% efficient b -tagging working point, which is a requirement that the MV2 BDT score is greater than 0.83. Pileup jets are suppressed using the Jet Vertex Tagger (JVT) algorithm [31]. The JVT is constructed using two parameters of JVF and R_{pT} that are defined in the following as a 2-dimensional likelihood.

The JVF is the ratio of the transverse momentum sum can remove the pile-up jet:

$$\text{JVF} = \frac{\Sigma_k p_T^k(\text{PV}_0)}{\Sigma_l p_T^l(\text{PV}_0) + \frac{\Sigma_{n \geq 1} \Sigma_l p_T^l(\text{PV}_n)}{(k \cdot n^{\text{PU}})}}, \quad (4.5)$$

where $\Sigma_k p_T^k(\text{PV}_0)$ is the scalar p_T sum of the tracks that are associated with the jet and originate from the hard-scatter vertex. The term $p_T^{\text{PU}} \equiv \Sigma_{n \geq 1} \Sigma_l p_T^l(\text{PV}_n)$ denotes the scalar p_T sum of the associated tracks that originate from any of the pileup interactions. To correct for the linear increase of the average scalar sum p_T from pileup tracks associated with a jet, $\langle p_T^{\text{PU}} \rangle$, with the total number of pileup tracks per event (n^{PU}), we divide that term by $k \cdot n^{\text{PU}}$ with $k = 0.01$. The total number of pileup tracks per event is computed from all tracks associated with vertices other than the hard-scatter vertex. The scaling factor k is roughly taken as the slope of $\langle p_T^{\text{PU}} \rangle$ with n^{PU} .

The R_{pT} is defined as the scalar p_T sum of the tracks that are associated with the jet and originate from the hard-scatter vertex divided by the fully calibrated jet p_T , which includes

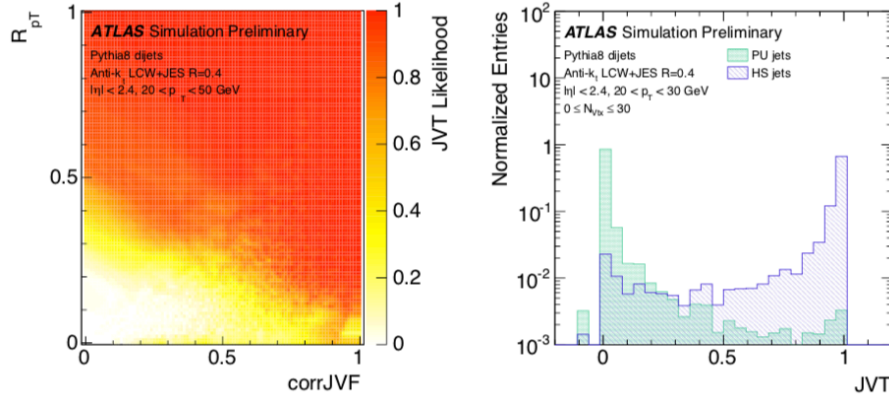


Figure 4.8: The 2-dimensional JVT likelihood as a function of JVF and R_{p_T} (left) and the distribution of JVT for pileup and hard-scatter jets with $20 < p_T < 30$ GeV (right). [31]

pileup subtraction:

$$R_{p_T} = \frac{\sum_k p_T^k(PV_0)}{p_T}. \quad (4.6)$$

R_{p_T} is peaked at 0 and steeply falling for pileup jets, where no or only little p_T from tracks from the hard-scatter vertex is expected. For hard-scatter jets, however, R_{p_T} has the meaning of a charged p_T fraction and its mean value and spread is larger than for pileup jets.

Figure 4.8 shows the 2-dimensional JVT likelihood as a function of JVF and R_{p_T} and the distribution of JVT for pileup and hard-scatter jets with $20 < p_T < 30$ GeV. In this analysis, these jets are required to pass the JVT requirement if the jets are in the range $p_T < 60$ GeV and $|\eta| < 2.4$. The JVT requirement has an inclusive efficiency of about 90% in that kinematic region.

Table 4.6: Summary of the jet selection used in the analysis.

Jet reconstruction parameters	
Selection requirements	
Observable	Requirement
p_T	> 40 GeV for Higgs candidates, > 30 for VBF candidates
$ \eta $	< 2.0 for Higgs candidates, > 2.0 for VBF candidates
JVT	> 0.59 for $p_T < 60$ GeV , $ \eta < 2.4$

4.5 Trigger efficiency

In this section, the efficiency of the signals for the multi- b -jet triggers listed in Section 4.2 are summarized. The MC efficiency of the individual triggers and their combination is investigated using the jet-level efficiency that is estimated using the data of the $t\bar{t}$ production. The procedure of the investigation and the results are described in the following.

4.5.1 Jet-level Trigger Efficiencies/Scale Factors

Leptonic top quark decays provide a clean, pure sample of b -jets from which the efficiency of the online b -tagging algorithm can be measured. Jet-level efficiencies and scale factors are measured using fully-leptonic $t\bar{t}$ events. Leptons emitted from $t\bar{t}$ are used to trigger and calibration chains are run which calculate the online b -tagging discriminants. The efficiency of the online b -tagging is then determined relative to jets that pass the offline b -tagging requirement. This sample is pure in b -jets ($>95\%$).

The jet-level efficiencies for the working point of the online b -tagging algorithm used in this analysis is shown in Figure 4.9. The efficiency is provided as a function of jet p_T . Other kinematic distributions, jet η , number of primary vertices, ΔR nearest jet, etc. were found to have little effect on the efficiency. For the jet p_T below 240 GeV, the uncertainty on these scale factors are dominated by the modeling of the impurities both before the online b -tagging requirement and after the online b -tagging requirement. These sources of uncertainty are fully correlated between p_T bins. For the jet p_T above 240 GeV, the statistics in data begins to run out. Here the efficiencies are extrapolated using MC. The uncertainties associated with this extrapolation begins to dominate at higher p_T . These uncertainties are also fully correlated between p_T bins. In the following, the jet-level uncertainties are assumed to be 100% correlated.

To apply the b -tag scale factors, it is necessary to convert the individual jet weights to an event-level weight. This is done following “Method 1” and “Method 2” described in the next Section 4.5.2. The difference between the trigger decision directly from simulation and this result (where the individual jets are considered separately, and the decision is emulated) can be considered a non-closure of the technique. This is a few % at most. The non-closure of the OR of the triggers is applied as an additional systematic uncertainty on the analysis, applied to MC-based samples.

4.5.2 Calculating the event-level efficiency

This section describes the procedure for deriving event-level efficiencies from the jet-level inputs. Two closely related methods are described: “Method-1” and “Method-2”. Method-2 uses Method-1 as a sub-routine and the final results and uncertainties are obtained with Method-2.

Method-1

Trigger decisions are provided for events passing a basic selection requiring two reconstructed Higgs candidates. These events have four offline b -tagged jets with $p_T > 40$ GeV.

The logic in Method-1 is as follows:

- Assign each of the four Higgs candidates jets a random number between 0 and 1.
- Interpret the numbers produced randomly at the previous stage less than $(1 - \epsilon_{\text{jet}})$ as failing the online b -tagging requirement, where ϵ_{jet} is the p_T -dependent trigger efficiency corrected to data.
- Count jets considered as passing the online b -tagging requirement above the various p_T thresholds to derive event-level decisions. The event-level decision is made based on the OR of all trigger decisions, i.e.: HLT_2j35_b60_2j35, HLT_j100_2j55_b60, and HLT_j225_b60 for 2016.

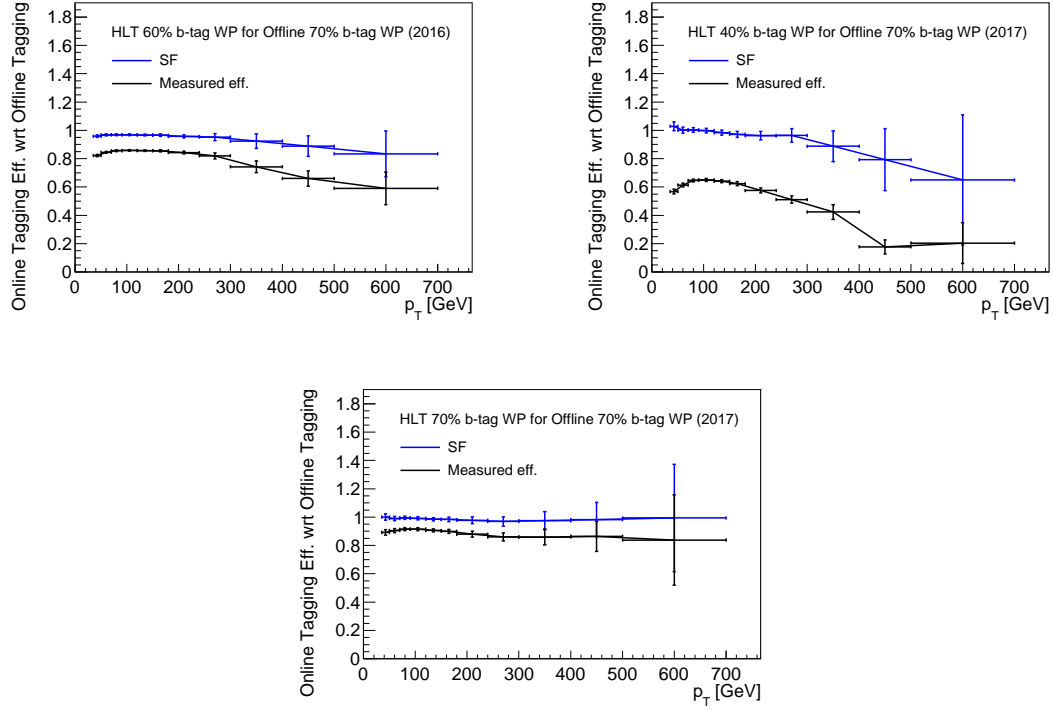


Figure 4.9: 2016 jet-level efficiency at 60% online b -tagging working point for offline jets at 70% offline b -tagging working point (upper left), 2017 jet-level efficiency at 40% online b -tagging working point for offline jets at 70% offline b -tagging working point (upper right), and 2017 jet-level efficiency at 70% online b -tagging working point for offline jets at 70% offline b -tagging working point (lower one). The black plots show the measured efficiency, and the blue plots show the scale factor as the ratio of simulated efficiency in MC and the measured efficiency.

Method-2

Method-1 yields a yes/no decision for each MC event; MC events that fail the trigger are not used. Method-2 presents a more optimal way of using the MC events to calculate the trigger efficiency. The logic in Method-2 is as follows:

- Repeat Method-1 N -times.
- Use the fraction of times the event passes the trigger according to Method-1 as estimate of the trigger efficiency.
- Weight the MC event by this estimated trigger efficiency

Method-2 has the advantage of using all the MC statistics and, as discussed below, can be extended to assess the systematic uncertainty on the event-level trigger efficiency.

The results of applying the trigger scale factors are shown in Figures 4.10 and 4.11 for the resonant and non-resonant signals. In all plots, the data-corrected simulation is shown with thicker lines, and is slightly lower than the MC-only simulation.

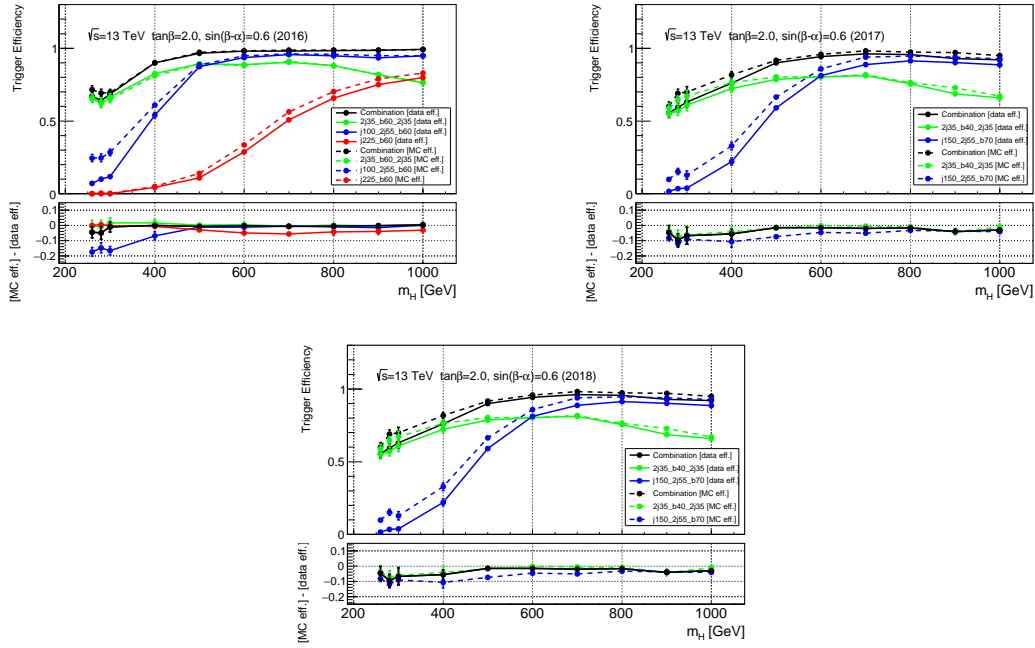


Figure 4.10: Trigger efficiency of 2016 trigger, 2017 trigger, and 2018 trigger comparing the online trigger decision simulation and b -tagging SF for resonant signal.

Calculating the uncertainty of the event-level efficiency

The uncertainty on the combined event-level trigger efficiency due to the uncertainty on the jet-level trigger efficiencies can be derived using Method-2. The procedure is as follows:

- Run Method-2 using ϵ_{jet} smeared by the measured uncertainty $\delta\epsilon_{\text{jet}}$.
- Repeat M-times to get a distribution of ϵ_{Event}
- Take the average of the measured event-level distribution as the event-level efficiency
- Take the RMS of the measured event-level distribution as the event-level uncertainty

The smearing of the jet-level efficiencies is done with a random number (g) drawn from unit Gaussian. For a given iteration of Method-2, the same g is used for all jets and all p_T bins, explicitly building in the correlation in the jet-level efficiencies. This procedure propagates jet-level uncertainties to the event-level including the proper correlations among the jets and the different trigger items. This event-level uncertainty is added in quadrature with the uncertainty coming from the non-closure of the method assumption discussed above.

4.6 Event selection

Optimization of the event selection criteria is performed using the $m_H = 600$ GeV mass point of the resonant signal, as it is in the middle of the considered mass range. Moreover, the resonant signal of the $m_H = 600$ GeV distributes in the middle of the m_{4b} (invariant mass of the $4b$ -jets) of the $\kappa_{2V} = 1$ and $\kappa_{2V} = 2$ point as shown in Figure 4.12, where the analysis has potential sensitivity to exclude the $\kappa_{2V} = 2$ point.

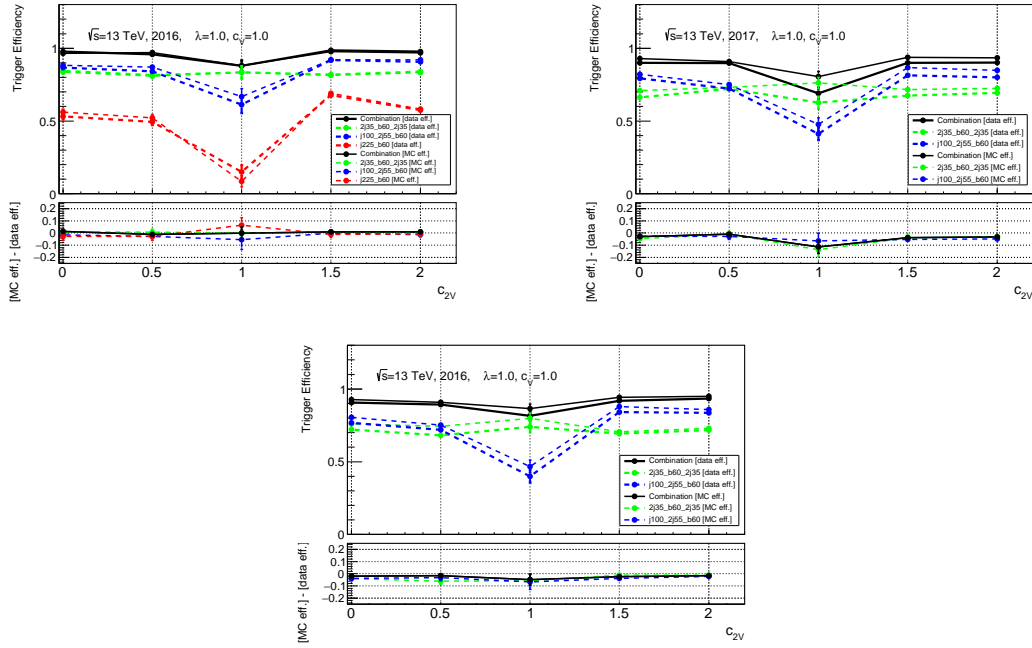


Figure 4.11: Trigger efficiency of 2016 trigger, 2017 trigger, and 2018 trigger comparing the online trigger decision simulation and b -tagging SF for non-resonant signal.

Events are required to contains at least four b -tagged anti- k_t $R = 0.4$ jets with $p_T > 40$ GeV and $|\eta| < 2.0$. The η distribution of the b -tagged jets are shown in Figure 4.13. The acceptance times efficiency of this requirement is shown in Figure 4.25 as the curve labelled " $4b$ $p_T > 40$ GeV, $|\eta_b| < 2.0$ ".

Two Higgs boson candidates are reconstructed from the $4b$ -jets. Three possible candidates are considered to reconstruct two pairs of $h \rightarrow b\bar{b}$ candidate. The angle between the decay products of the Higgs boson in the lab frame is dependent on the Lorentz boost of the Higgs boson and thus on the invariant mass of the four b -jet system, m_{4b} . High mass resonances would generally produce Higgs bosons with sufficient boost to ensure their respective decay products are nearby in η and ϕ . For resonances with masses closer to $2 \times m_h$, the pairing of jets to construct Higgs boson candidates is more ambiguous. Accordingly, of the three possible pairings of jets into Higgs boson candidates, only those which satisfy the following requirements are used:

$$\begin{cases} \frac{360 \text{ GeV}}{m_{4b}} - 0.5 < \Delta R_{bb,\text{lead}} < \frac{653 \text{ GeV}}{m_{4b}} + 0.475 \\ \frac{235 \text{ GeV}}{m_{4b}} < \Delta R_{bb,\text{subl}} < \frac{875 \text{ GeV}}{m_{4b}} + 0.35 \end{cases} \quad \text{if } m_{4b} < 1250 \text{ GeV}, \quad (4.7)$$

$$\begin{cases} 0 < \Delta R_{bb,\text{lead}} < 1 \\ 0 < \Delta R_{bb,\text{subl}} < 1 \end{cases} \quad \text{if } m_{4b} > 1250 \text{ GeV}. \quad (4.8)$$

The leading (sub-leading) Higgs boson candidate is defined to be the candidate with the (second) highest scalar sum of jet transverse momenta. In those expressions, $\Delta R_{bb,\text{lead}} \equiv \sqrt{\Delta\eta_{bb}^2 + \Delta\phi_{bb}^2}$ is the angular distance between jets for the leading Higgs boson candidate and $\Delta R_{bb,\text{subl}}$ for the sub-leading Higgs boson candidate.

In the absence of energy loss through semi-leptonic b -hadron decays, the optimal choice would be the combination most consistent with the decays of two particles of equal mass. To account for energy loss, the choice is modified to the pairing that minimizes the distance, D_{hh} , from a

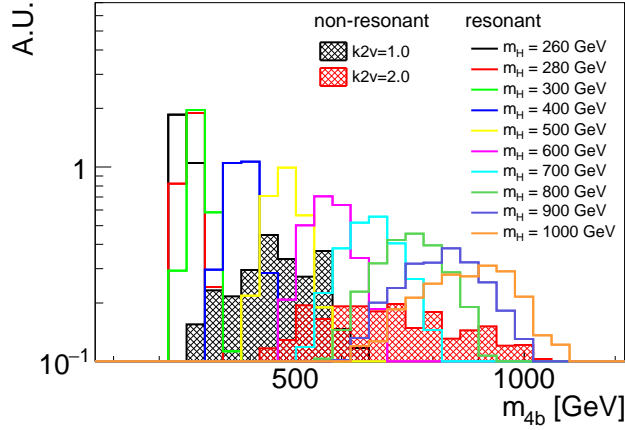


Figure 4.12: The m_{4b} distribution of wide resonant signals for the parameters of $\tan \beta = 2.0$ and $\sin(\beta - \alpha) = 0.6$ in the Type-II 2HDM, and the non resonant signal with $\kappa_{2V} = 1.0, 2.0$.

line connecting $(0 \text{ GeV}, 0 \text{ GeV})$ and $(123.7 \text{ GeV}, 116.5 \text{ GeV})$ which is the center point of the signal region defined later:

$$D_{hh} = \sqrt{(m_{2b}^{\text{lead}})^2 + (m_{2b}^{\text{subl}})^2} \left| \sin \left(\tan^{-1} \left(\frac{m_{2b}^{\text{lead}}}{m_{2b}^{\text{subl}}} \right) - \tan^{-1} \left(\frac{116.5}{123.7} \right) \right) \right|, \quad (4.9)$$

where m_{2b}^{lead} is the mass of the leading Higgs boson candidate and m_{2b}^{subl} is the mass of the sub-leading candidate. The punch picture of D_{hh} is shown in Figure 4.14 for reference.

In addition, events are required to have two leading forward anti- k_t $R = 0.4$ jets with $p_T > 30 \text{ GeV}$, $|\eta| > 2.0$ and opposite sign of η . The η regions for b-jets and VBF jets are completely separated to avoid weird behavior of pseudo-tagging in $2b/4b$ extrapolation used for the estimation of the QCD multi-jet background which is described in Section 4.7.1. Figure 4.15 shows the η distribution before the η cut in the signal. The optimization of the η -requirement is described in Appendix A. The η distribution of forward jets after the cut is shown in Figure 4.16. To discriminate the signal from the multijet background, two forward jets are required to have $\Delta\eta_{jj} > 5.0$ and the invariant mass of the two forward jets to be $m_{jj} > 1000 \text{ GeV}$. The $\Delta\eta_{jj}$ and the m_{jj} distributions are shown for the multi-jet background and signal in Figures 4.17 and 4.18, respectively. The acceptance times efficiency of these requirements are shown in Figure 4.25 as the curve labelled " $\Delta\eta_{2\text{VBF-jets}}$ " and " $m_{2\text{VBF-jets}}$ ", respectively.

This analysis searches for the non-resonant signal and for resonances over a wide range of masses, $260 \text{ GeV} < m_H < 1000 \text{ GeV}$. Event selection criteria that vary as a function of the reconstructed resonance mass are used to enhance the analysis sensitivity across the whole mass range. Mass-dependent requirements are made on the leading Higgs boson candidate transverse momentum, p_T^{lead} , and the sub-leading Higgs boson transverse momentum, p_T^{subl} :

$$\begin{aligned} p_T^{\text{lead}} &> 0.5m_{4b} - 90 \text{ GeV} \\ p_T^{\text{subl}} &> 0.33m_{4b} - 70 \text{ GeV}, \end{aligned} \quad (4.10)$$

where m_{4b} is again expressed in GeV. The QCD multi-jet background is further suppressed by the m_{4b} -independent cut on difference of the pseudo rapidity between the two Higgs boson candidates, $|\Delta\eta_{hh}| < 1.5$. The distribution of $\Delta\eta_{hh}$ before the cut is shown in Figure 4.19.

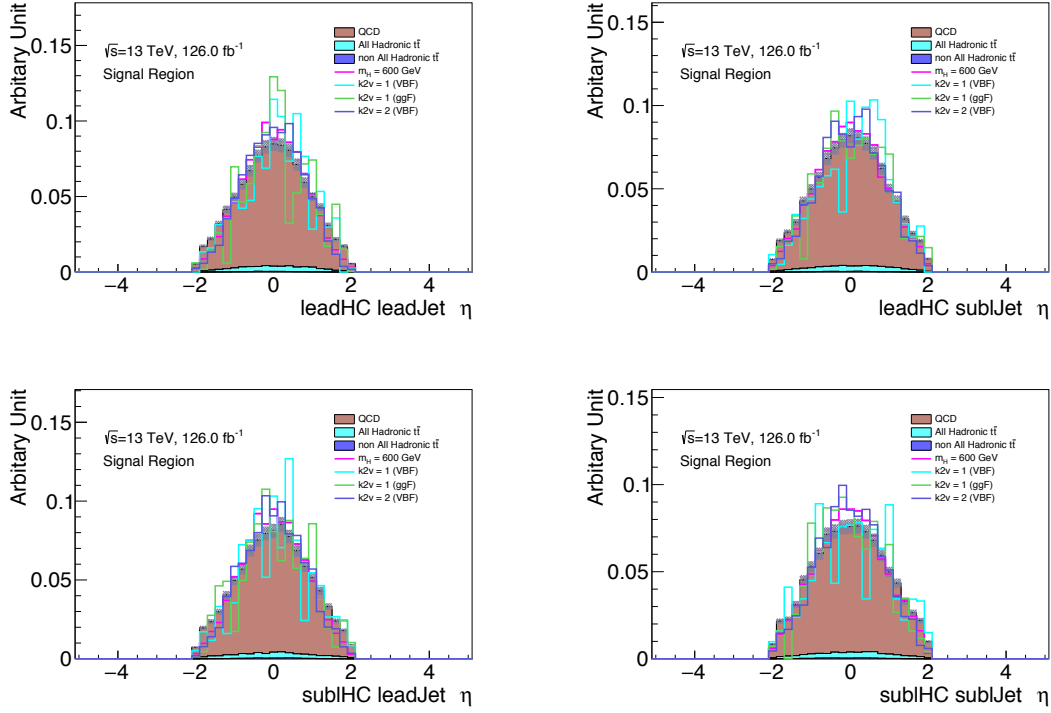


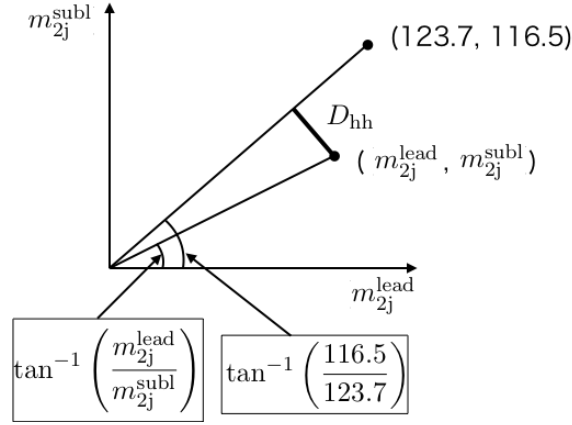
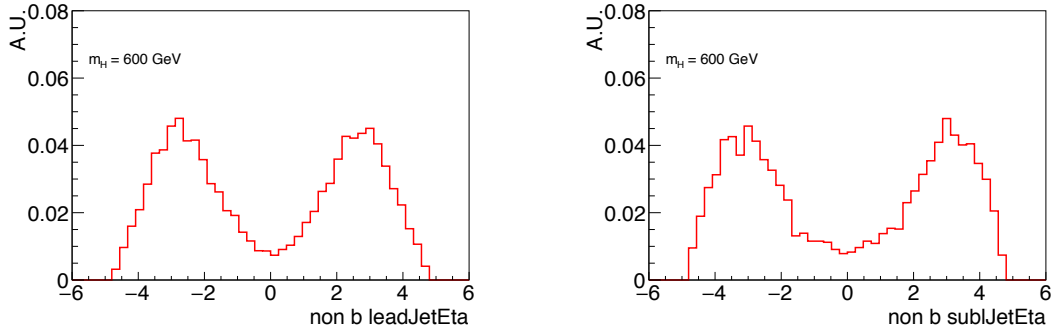
Figure 4.13: Jet η distributions for the backgrounds (QCD multi-jet and $t\bar{t}$) and the signal ($m_H = 600$ GeV). The leading jet from the leading Higgs boson candidate (upper left), the sub-leading jet from the leading Higgs boson candidate (upper right), the leading jet from the sub-leading Higgs boson candidate (lower left), and the sub-leading jet from the sub-leading Higgs boson candidate (lower right) are shown.

Since the multi-jets background has larger jet multiplicity than the signal as shown in Figure 4.20, magnitude of the vector sum of the four b -tagged jets and the two forward jets shown in Figure 4.21 is required to be less than 60 GeV. The QCD background has a larger value, because the vector sum of the 6 selected jets does not fully balance in the transverse plane. For the signal, since each selected jets fully correspond to one of the b -jets from h decays or jets from VBF, the system has no significant transverse momentum.

The $t\bar{t}$ background is reduced by applying the selection of X_{Wt} defined in the equation 4.11. All combinations of three jets out of 6 jets (where at least one is part of the Higgs candidates) are considered. A jet with the highest MV2 score of the three jets is chosen as the b -jet from the top decay, and the other two are chosen as the hadronically decaying W -boson.

$$X_{Wt} = \sqrt{\left(\frac{m_{jj} - 80.4}{0.1m_{jj}}\right)^2 + \left(\frac{m_{bjj} - 172.5}{0.1m_{bjj}}\right)^2}, \quad (4.11)$$

where m_{jj} is the invariant mass of two non- b jets and m_{bjj} is the invariant mass of b -jet and two non- b jets. The smallest X_{Wt} in all combinations is chosen for each event. Events with $X_{Wt} < 1.5$ are regarded as top quark events and rejected. Figure 4.22 shows the X_{Wt} distribution before the X_{Wt} cut in the signal region.


 Figure 4.14: The punch picture of the D_{hh} .

 Figure 4.15: Jet η distribution of leading (left) and sub-leading (right) VBF jets for the signal with $m = 600$ GeV, before the cut.

A requirement on the Higgs boson candidate masses is used to define the signal region:

$$X_{hh} = \sqrt{\left(\frac{m_{2b}^{\text{lead}} - 123.7 \text{ GeV}}{11.55 \text{ GeV}}\right)^2 + \left(\frac{m_{2b}^{\text{subl}} - 116.5 \text{ GeV}}{18.05 \text{ GeV}}\right)^2} < 1.6, \quad (4.12)$$

where the values of 123.7 GeV and 116.5 GeV are the center point of the leading and sub-leading Higgs boson candidate mass, and the values of 11.55 GeV and 18.05 GeV in the denominator represent the widths of the leading and sub-leading Higgs boson candidate mass. Those values are derived by maximizing the signal significance according to the 2D distribution in $(m_{2b}^{\text{lead}}, m_{2b}^{\text{subl}})$. The signal region in the 2D distribution of masses of Higgs candidates is shown in Figure 4.23. These values are closer to the true value of the Higgs boson mass compared to the values used for the previous ggF analysis (120 GeV and 110 GeV) because of the b -jet energy regression applied in this VBF analysis. The distribution of the X_{hh} is shown in Figure 4.24.

The acceptance times efficiency for requirements discussed above including the signal region requirement described in Equation 4.12 are summarized in Figure 4.25 for the non-resonant signal as a function of the κ_{2V} coupling modifier and for the resonant signal models as a function of the generated mass. For the non-resonant signals, the acceptance times efficiency ranges from 1% at large deviation from $\kappa_{2V} = 1$ of the SM hypothesis, to 0.1% at $\kappa_{2V} = 1$. For the resonant signals, the acceptance times efficiency ranges from 1% at high mass, to 0.1% at low mass.

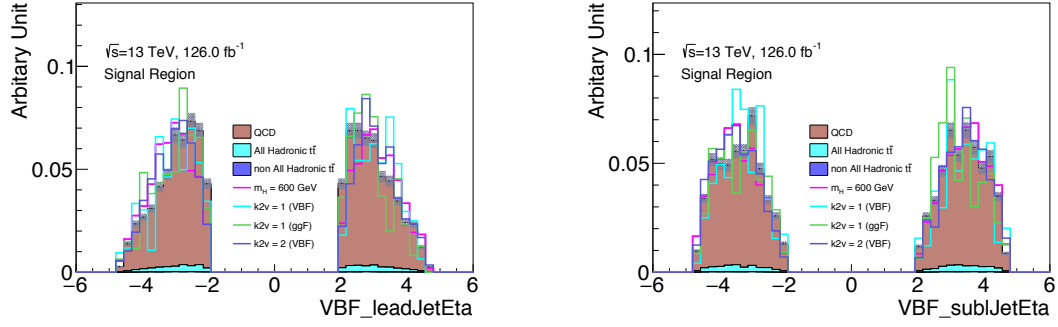


Figure 4.16: Jet η distribution of leading (left) and sub-leading (right) VBF jets for multi-jet background and signal ($m_H = 600$ GeV) after the cut.

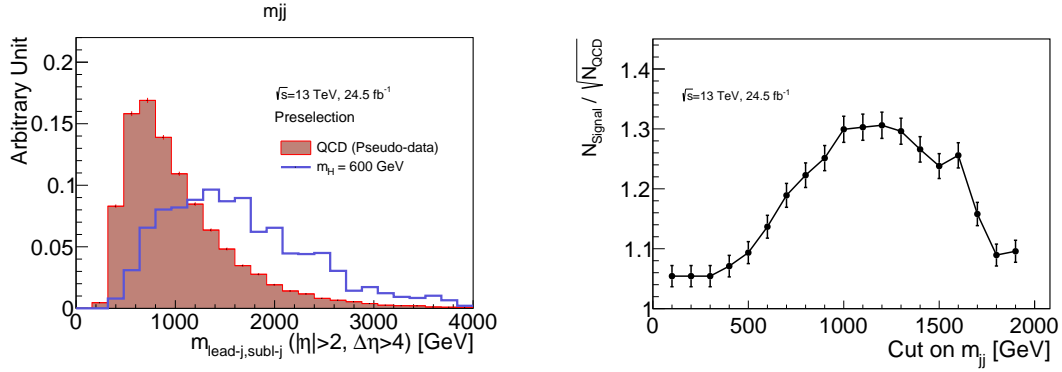


Figure 4.17: The m_{jj} distribution for multi-jet background and signal ($m_H = 600$ GeV) is shown on the left. The significance as a function on the m_{jj} cut is shown on the right.

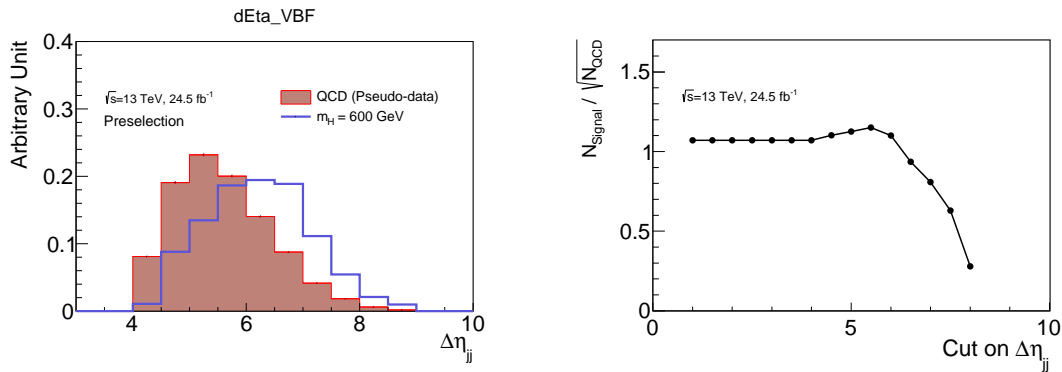


Figure 4.18: The $\Delta\eta_{jj}$ distribution for multi-jet background and signal ($m_H = 600$ GeV) is shown on the left. The significance as a function on the $\Delta\eta_{jj}$ cut is shown on the right.

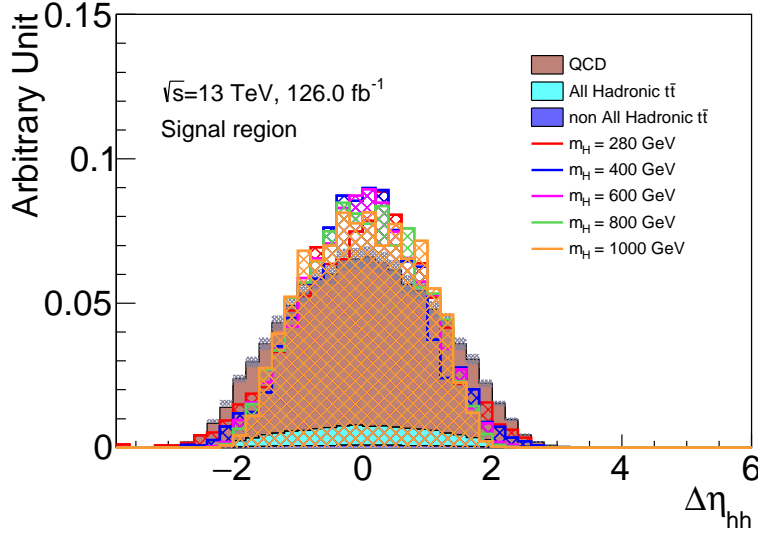


Figure 4.19: The distribution of the $\Delta\eta_{hh}$ of the resonant signals and the backgrounds. The cut of $|\Delta\eta_{hh}| < 1.5$ will be applied to this distribution.

To estimate and evaluate the background in the signal region, we use the regions that the kinematics are similar to the signal region but the signal yields is negligible. The sideband region for the background estimation and validation region for the evaluation of the estimation results are respectively defined by:

$$\sqrt{(m_{2b}^{\text{lead}} - (123.7 \text{ GeV}))^2 + (m_{2b}^{\text{subl}} - (116.5 \text{ GeV}))^2} < 45 \text{ GeV}, \quad (4.13)$$

$$\sqrt{(m_{2b}^{\text{lead}} - (123.7 \text{ GeV}))^2 + (m_{2b}^{\text{subl}} - (116.5 \text{ GeV}))^2} < 30 \text{ GeV}. \quad (4.14)$$

The signal region and the validation region are excluded in the sideband region and the signal region is excluded in the validation region. Figure 4.23 shows the signal region, validation region, and sideband region in the two-dimensional mass plane with the distribution of the non-resonant hh signal and the QCD multi-jet background.

4.7 Background estimation

4.7.1 QCD multijet background modelling

The QCD multi-jet background is modeled using an independent data sample enriched in the QCD multi-jet background. This data sample is selected using events where only two of the selected jets are b -tagged, the " $2b$ region". The Higgs boson candidates are built and the same event selection used to define the signal region is applied. The jets used to form Higgs boson candidates in this $2b$ region are selected based on their MV2 ordering.

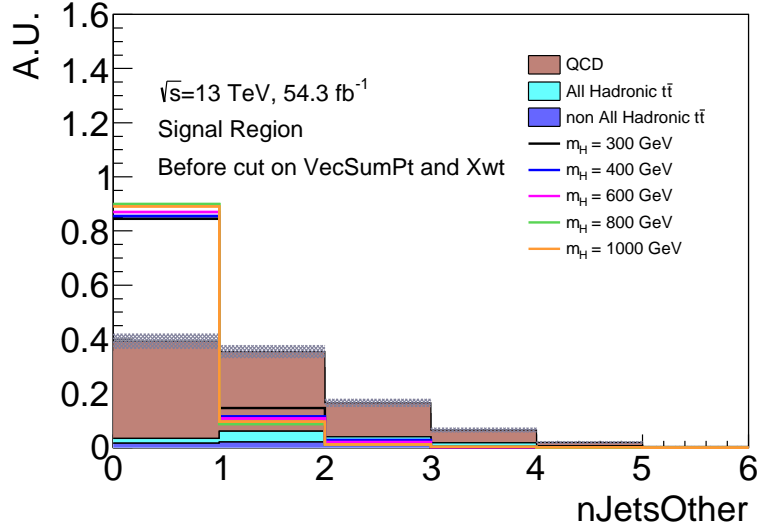


Figure 4.20: The distribution of the number of jets except for the four b -jets in the region of $|\eta| < 2.0$.

Higgs boson candidates in $2b$ region

As a reminder, events in the signal region are pre-selected to have at least four b -tagged jets. The selected jets are then paired to form Higgs boson candidates following the procedure described in Section 4.6.

The QCD multi-jet background passing the signal selection is modeled using events with fewer number of b -tagged jets. The working assumption is that the yield and kinematics of events selected with a b -tagged jet (" t ") can be modeled by scaling events selected using the same criteria but with the b -tagged jet replaced with a non- b -tagged jet (" n "):

$$f \cdot n \xrightarrow{\text{models}} t, \quad (4.15)$$

where f is a scale factor that relates a non- b -tagged jet to a b -tagged jet. In other words, events selected using the $X + (t)$ criteria can be modeled using events selected using $X + (n)$ criteria and weighted by f , where X represents all other event selection criteria beside the b -tagging requirement. The non- b -tagged jet n is called "pseudo-tagged" jet after scaling the event weight by f and the event selection proceeds as if n passed the b -tagging requirement.

In this analysis, events with two b -tagged jets are used to derive the QCD multi-jet background model. Events in the $2b$ region are pre-selected to have at least four jets with $|\eta| < 2.0$, two of which satisfy the b -tagging requirement. After selecting jets to build Higgs boson candidates, the jet pairing and event selection proceeds exactly as in the signal region.

In the case of more than two non- b -tagged jets in an event, each potential assignment of the pseudo-tag to non- b -tagged jets has to be considered. The events are scaled by an appropriate scale factor to account for the probability to contain at least two pseudo-tagged jets. In the case where more than one assignment leads to at least two pseudo-tagged jets in the event, one of the assignments is picked at random using the relative probabilities of each assignment. For example, the probability of the each assignment is f^3 for the case that all three non-tagged jets are pseudo-tagged, and ${}_3C_2(1-f)f^2$ for the case that two of three non-tagged jets are

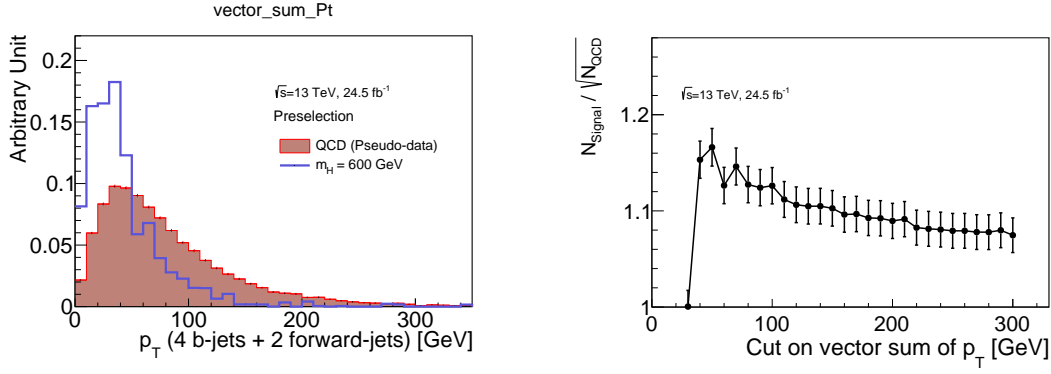


Figure 4.21: The transverse momentum of the vector sum of the four b -tagged jets and the two forward jets for the multi-jet background and signal ($m_H = 600$ GeV) is shown on the left. The significance as a function of the vector sum p_T is shown on the right.

Table 4.7: The results of the simultaneous binned fit of the pseudo-tag rate f and the QCD multi-jet normalisation a_{QCD} .

	f	a_{QCD}
2016 (24.5 fb $^{-1}$)	0.127 ± 0.043	0.322 ± 0.018
2017 (42.9 fb $^{-1}$)	0.129 ± 0.033	0.413 ± 0.017
2018 (58.6 fb $^{-1}$)	0.162 ± 0.034	0.294 ± 0.013

pseudo-tagged. Higgs boson candidates are then built from the two b -tagged jets and the two pseudo-tagged jets following the same procedure as in the signal region. In particular, in the case where there are more than four b -tagged and pseudo-tagged jets¹, the jets are ordered by their MV2 discriminant and the four jets with the highest MV2 score are selected for Higgs boson candidate building. The weights for each multiplicity are:

- 2-tag + 2 non-tagged events scale with weight: f^2
- 2-tag + 3 non-tagged events scale with weight: ${}_3C_2(1-f)f^2 + f^3$
- 2-tag + 4 non-tagged events scale with weight: ${}_4C_2(1-f)^2f^2 + {}_4C_3(1-f)f^3 + f^4$

The notation for e.g. ${}_3C_2$ means "3 choose 2" in the usual statistical sense.

The number of additional jets, $n_{\text{JetsOther}}$, is fitted to derive the scale factor f ("pseudo-tag rate") in the sideband region for each data-taking year separately. The number of events as a function of $n_{\text{JetsOther}}$ is defined as $N_{n_{\text{JetsOther}}}^i$ ($n_{\text{JetsOther}} = 0, 1, 2, \dots; i = 2b, 4b$). The scale factor f and the QCD multi-jet normalization factor, a_{QCD} , are free parameters in the binned fit. The post-fit $n_{\text{JetsOther}}$ distributions are shown in Figure 4.26 and the fit results are summarized in Table 4.7. The pseudo-tag rate f is obtained with statistical uncertainty of about 5%. The shapes of the data and the estimated backgrounds agree very well.

Figure 4.27 shows a few kinematic distributions: the invariant mass of the two forward jets (m_{jj}), the $\Delta\eta$ between the two forward jets ($\Delta\eta_{jj}$) and the p_T of the vector sum of 4 b -jets and

¹In other words, the case with more than two pseudo-tagged jets. Note that this assures that the two b -tagged are always selected for Higgs candidate building.

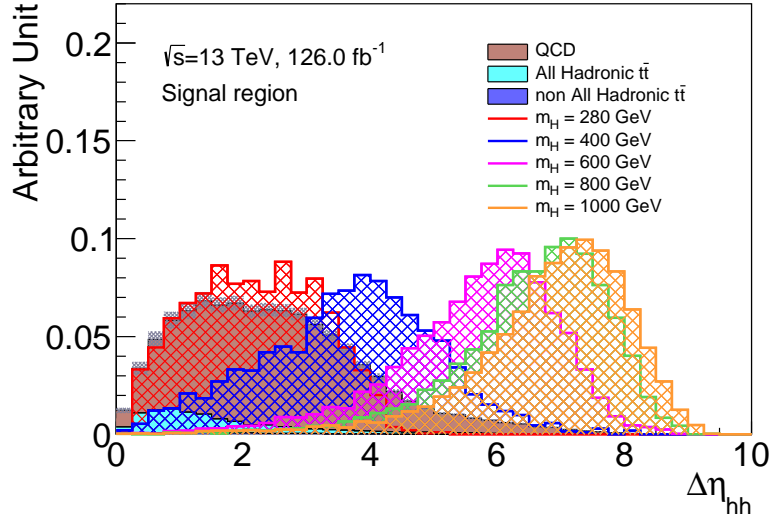

 Figure 4.22: The X_{Wt} distribution before the X_{Wt} cut in the signal region.

 Table 4.8: The results of the straight line fit ($y = Ax + B$) to the ratio of data and estimated background in the sideband region.

	A	B	χ^2/NDF
$ \Delta\eta_{jj} $ (VBF jets)	$(-1.1 \pm 1.9) \times 10^{-2}$	1.06 ± 0.11	0.95
m_{jj} (VBF jets)	$(-8.0 \pm 3.0) \times 10^{-5}$	1.08 ± 0.04	1.15
p_T (bbbb+VBFs)	$(-2.2 \pm 2.2) \times 10^{-4}$	1.01 ± 0.03	0.62

2 forward jets in the sideband region. The QCD multijet background is estimated using the method described above, with the pseudo-tagging applied. A good agreement between data and backgrounds is observed within the statistical uncertainty. Table 4.8 shows the result of a linear fit to the data/background ratio, which shows no significant slope. The uncertainties included are the statistical uncertainties and the uncertainty of the normalization in the CR.

Similar plots of the VBF related variables, and the same linear fit to the data/background ratio in the validation region, are shown in Figure 4.28 and Table 4.9. Again, the agreement is quite good, showing that the modeling of the VBF jets is very good using only the pseudo-tagging procedure previously described.

4.7.2 $t\bar{t}$ Background Modelling

All hadronic $t\bar{t}$

The shape of the all hadronic $t\bar{t}$ background is modeled with MC that requires only $2b$ -jets ($2b$ sample) in the final states as well as the QCD multi-jet background, reweighted with the same reweighting functions as derived for the QCD multi-jet background. This is because the statistics of the MC with requirement of $4b$ -jets are low. The pseudo tag rate is derived in such way that the yields of $4b$ and reweighted $2b$ samples are consistent at preselection level. All relevant kinematic distributions with or without the reweighting are modeled well as shown in

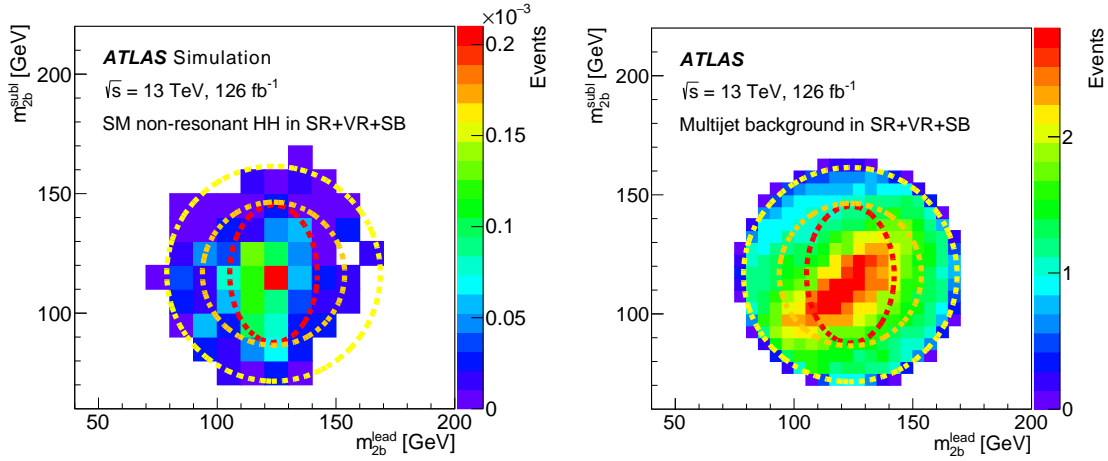


Figure 4.23: Two-dimensional mass regions used in the analysis. The signal region is inside the inner (red) dashed curve, the validation region is outside the signal region and within the intermediate (orange) circle, and the sideband is outside the validation region and within the outer (yellow) circle. The SM non-resonant hh process (left) and the estimated multi-jet background (right) are shown.

Table 4.9: The results of the straight line fit ($y = Ax + B$) to the ratio of data and estimated background in Validation region with loosened selection.

	A	B	χ^2/NDF
$\Delta\eta$ (VBF jets)	$(3.3 \pm 3.0) \times 10^{-2}$	0.96 ± 0.17	1.20
m_{jj} (VBF jets)	$(-4.0 \pm 4.0) \times 10^{-5}$	1.02 ± 0.06	1.05
p_T ($bbbb$ +VBF jets)	$(-3.2 \pm 3.3) \times 10^{-4}$	1.01 ± 0.04	0.97

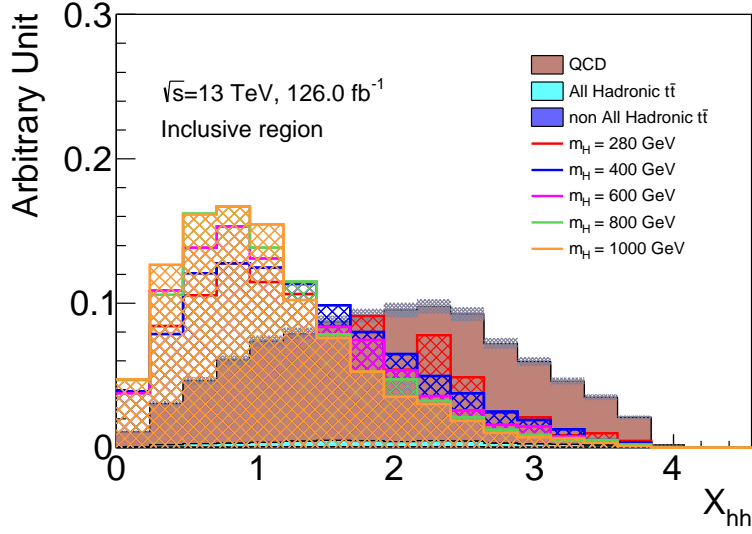
Appendix B.2.

Non all hadronic $t\bar{t}$

The shape of the $t\bar{t}$ events with single lepton or di-lepton in the final state (non-all hadronic $t\bar{t}$) is modeled using MC simulation. The 2b MC is used because the 4b statistics are low. All relevant kinematic distributions with/without the reweighting are modeled well as shown in Appendix B.1. The pseudo tag rate is derived in such way that the yields of 4b and reweighted 2b samples are consistent at preselection level.

4.7.3 Control regions for the normalization of backgrounds

The normalization of backgrounds (all hadronic $t\bar{t}$ and QCD multi-jet backgrounds) is determined by fitting the yields of each background events in two control regions. The QCD multi-jet control region is the region $0.75 < X_{Wt}$. The statistics and m_{4b} distribution in the QCD multi-jet control region are shown in Table 4.10, 4.11, 4.12 and Figure 4.29. Since the trigger menu are different for each year, the trigger efficiency of the data samples in the 4b region and 2b region are different

Figure 4.24: The X_{hh} distribution of the resonant signals and the backgrounds.

for each year. Therefore, the normalization of the pseudo-tagged $2b$ dataset is performed for each year, independently. Since the statistics in the QCD multi-jet control region with nominal selections on m_{jj} , $\Delta\eta_{jj}$, and VectorSum p_T are small, the region with loosened selection is used to normalize the QCD multi-jet background with uncertainty of less than about 10%.

We use for the region $X_{Wt} < 0.75$ the control region for all hadronic $t\bar{t}$ background. The statistics and m_{4b} distribution in the control region are shown in Table 4.13, 4.14 and Figure 4.30. Since the trigger menu are different for each year, the trigger efficiency of the $4b$ sample and $2b$ sample are different for each year. Therefore, the normalization of the $2b$ sample is performed for each year, independently.

Table 4.10: Yields with nominal selection and loosened selection in control region for QCD multi-jet background for 2016 dataset.

selection	data	total bkg.	multi-jet	all had. $t\bar{t}$	non all had. $t\bar{t}$
$m_{jj} > 1000$ [GeV], $\Delta\eta_{jj} > 5$, VectorSum p_T < 60 [GeV]	87	102.5 ± 5.0	92.3 ± 4.5	9.5 ± 2.1	0.68 ± 0.14
$m_{jj} > 0$ [GeV], $\Delta\eta_{jj} > 4$, VectorSum p_T < 1000 [GeV]	611	614.4 ± 29.2	531.4 ± 23.9	76.5 ± 16.8	6.5 ± 1.3

Table 4.11: Yields with nominal selection and loosened selection in control region for QCD multi-jet background for 2017 dataset.

selection	data	total bkg.	multi-jet	all had. $t\bar{t}$	non all had. $t\bar{t}$
$m_{jj} > 1000$ [GeV], $\Delta\eta_{jj} > 5$, VectorSum p_T < 60 [GeV]	184	175.3 ± 5.6	165.1 ± 5.0	8.6 ± 2.6	1.6 ± 0.3
$m_{jj} > 0$ [GeV], $\Delta\eta_{jj} > 4$, VectorSum p_T < 1000 [GeV]	1061	1074.5 ± 37.8	976.6 ± 29.3	79.6 ± 23.9	18.3 ± 0.4

Table 4.12: Yields with nominal selection and loosened selection in control region for QCD multi-jet background for 2018 dataset.

selection	data	total bkg.	multi-jet	all had. $t\bar{t}$	non all had. $t\bar{t}$
$m_{jj} > 1000$ [GeV], $\Delta\eta_{jj} > 5$, VectorSum p_T < 60 [GeV]	177	225.6 ± 9.6	197.9 ± 5.9	25.1 ± 7.5	2.6 ± 0.5
$m_{jj} > 0$ [GeV], $\Delta\eta_{jj} > 4$, VectorSum p_T < 1000 [GeV]	1238	1249.9 ± 40.0	1158.4 ± 34.8	62.9 ± 18.9	28.6 ± 5.6

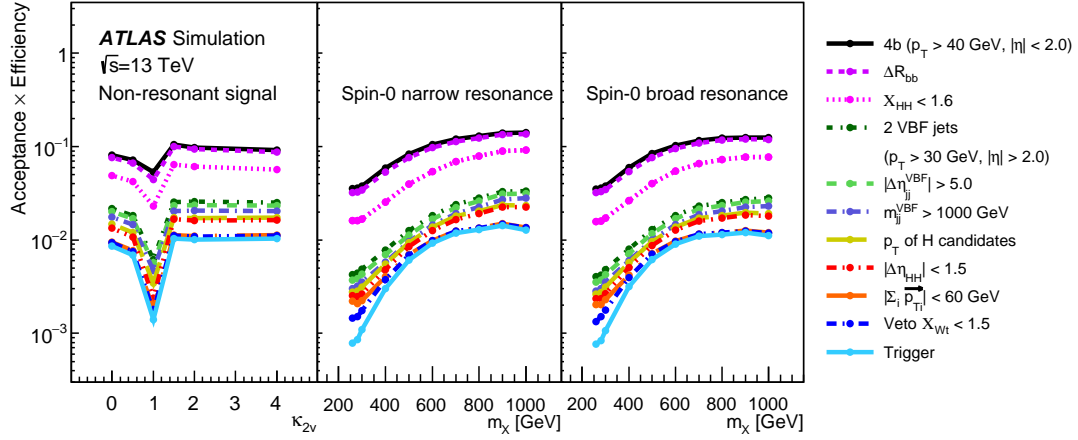


Figure 4.25: Cumulative acceptance times efficiency at each stage of the event selection. The number of events surviving the selection divided by the number of generated events is reported separately for the non-resonant signal as a function of the κ_{2V} coupling modifier and for the narrow- and broad-width resonance production hypotheses as a function of the generated mass.

Table 4.13: Yields with nominal selection and loosened selection in control region for all hadronic $t\bar{t}$ background 2016 dataset.

selection	data	total bkg.	multi-jet	all had. $t\bar{t}$	non all had. $t\bar{t}$
$m_{jj} > 1000$ [GeV], $\Delta\eta_{jj} > 5$, VectorSum $p_T < 60$ [GeV]	8	8.68 ± 0.35	5.90 ± 0.27	2.66 ± 0.53	0.12 ± 0.02
$m_{jj} > 0$ [GeV], $\Delta\eta_{jj} > 4$, VectorSum $p_T < 1000$ [GeV]	73	70.5 ± 5.5	43.3 ± 1.9	25.8 ± 5.2	1.4 ± 0.3

Table 4.14: Yields with nominal selection and loosened selection in control region for all hadronic $t\bar{t}$ background 2017 dataset.

selection	data	total bkg.	multi-jet	all had. $t\bar{t}$	non all had. $t\bar{t}$
$m_{jj} > 1000$ [GeV], $\Delta\eta_{jj} > 5$, VectorSum $p_T < 60$ [GeV]	15	13.2 ± 0.7	10.8 ± 0.32	2.05 ± 0.62	0.30 ± 0.06
$m_{jj} > 0$ [GeV], $\Delta\eta_{jj} > 4$, VectorSum $p_T < 1000$ [GeV]	112	104.2 ± 7.7	76.2 ± 2.3	24.4 ± 7.3	3.6 ± 0.7

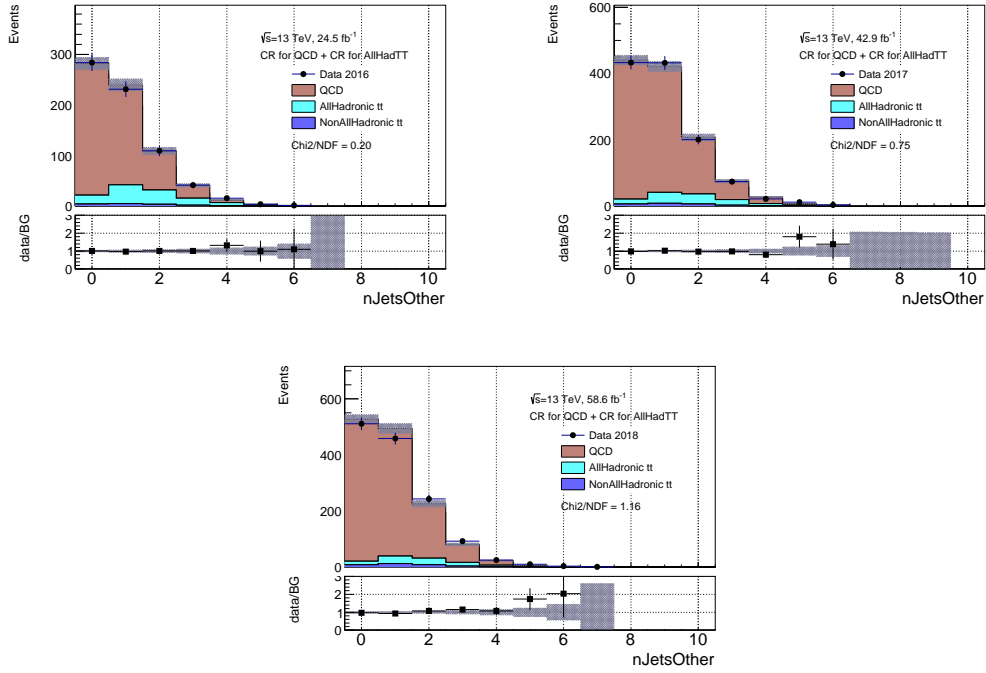


Figure 4.26: The post-fit distribution of number of additional jets, $nJetsOther$, in $|\eta| < 2.0$ in the sideband region for each year. The black dots in the plots shows the $4b$ data which contains $4b$ -jets and other additional jets in $|\eta| < 2.0$ (Note that the jets from VBF in $|\eta| > 2.0$ are not contained in these plots.). The QCD multi-jet background (reddish brown histogram) is derived in the $2b$ region using the pseudo-tagging method described in Section 4.7.1. The applied scale factors f and the QCD multi-jet normalization are summarized in Table 4.7.

Table 4.15: Yields with nominal selection and loosened selection in control region for all hadronic $t\bar{t}$ background 2018 dataset.

selection	data	total bkg.	multijet	all had. $t\bar{t}$	non all had. $t\bar{t}$
$m_{jj} > 1000$ [GeV], $\Delta\eta_{jj} > 5$, VectorSum $p_T < 60$ [GeV]	16	16.4 ± 2.0	10.1 ± 0.3	5.9 ± 2.0	0.44 ± 0.09
$m_{jj} > 0$ [GeV], $\Delta\eta_{jj} > 4$, VectorSum $p_T < 1000$ [GeV]	105	107.9 ± 6.3	83.2 ± 2.5	18.9 ± 5.7	5.8 ± 1.2

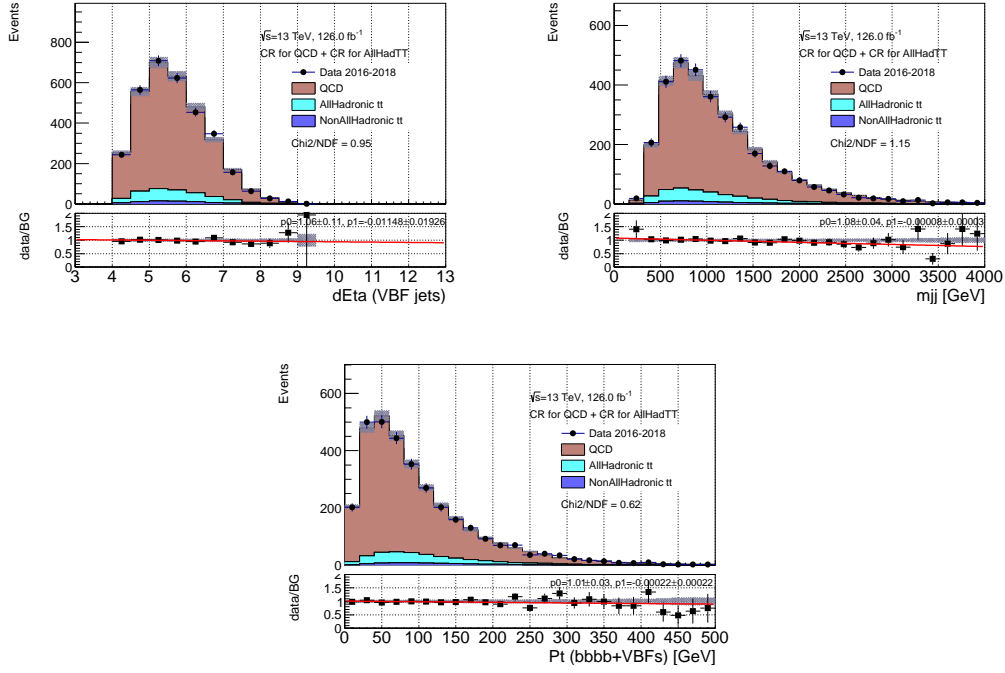


Figure 4.27: Some kinematic distributions in the $4b$ sideband region. The QCD multi-jet background is derived in the $2b$ region using the method described in Section 4.7.1.

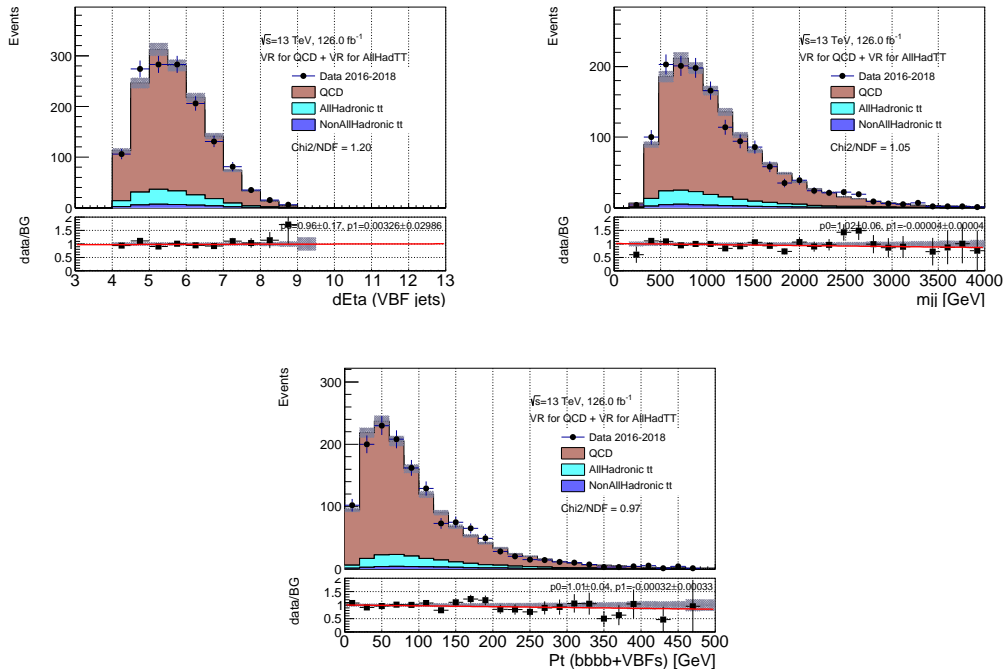


Figure 4.28: Comparison of $4b$ data and $2b$ data reweighted by pseudo tag rate f in Validation region with loosened selection.

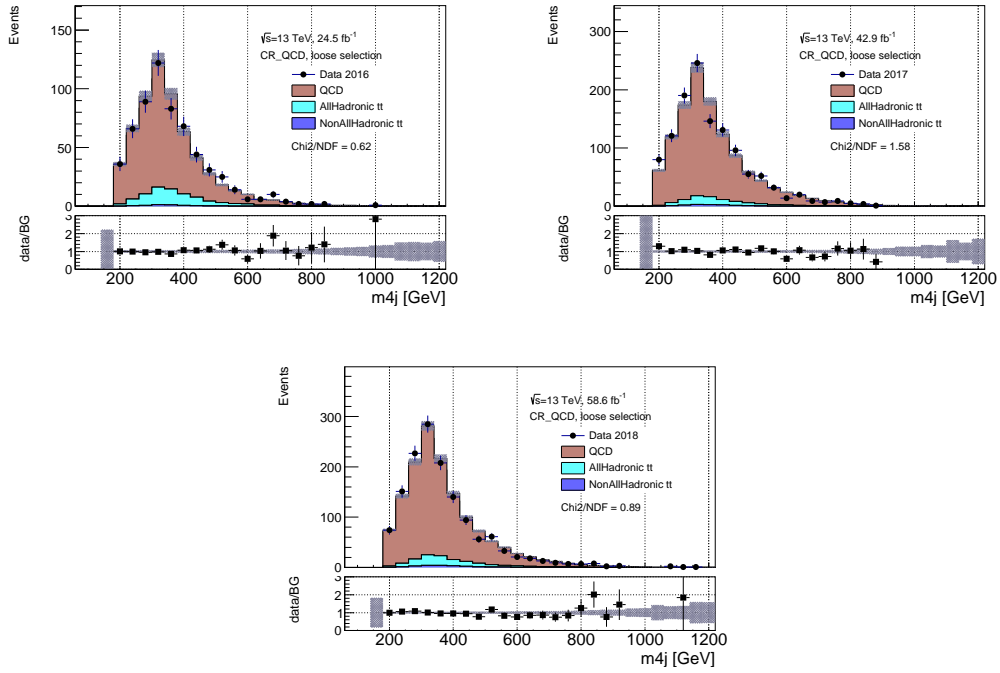


Figure 4.29: The distributions of the invariant mass of four b -jets, m_{4j} , with loosened selection [$m_{jj} > 0$ [GeV], $\Delta\eta_{jj} > 4$, VectorSum $p_T < 1000$ [GeV]] (right) in control region for QCD multi-jet background for each year.

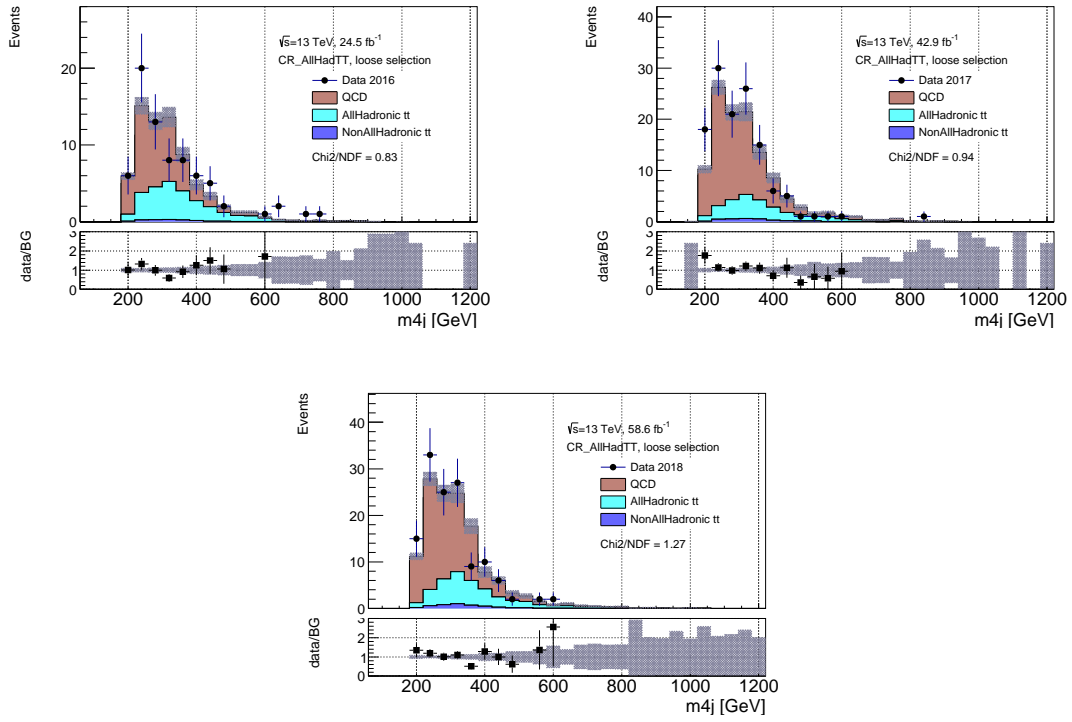


Figure 4.30: m_{4j} distributions with loosened selection [$m_{jj} > 0$ [GeV], $\Delta\eta_{jj} > 4$, VectorSum $p_T < 1000$ [GeV]] in control region for all hadronic $t\bar{t}$ background of each year.

4.7.4 The kinematic reweighting

Jets are b -tagged in this analysis both online in the trigger and offline in the final reconstruction with a flat cut on the jet MV2 score. In both cases the b -tagging efficiency is a function of p_T and η . On the other hand, the pseudo-tagging is performed by the multiplying the constant scale factor f to the dataset in the $2b$ region. For this reason, kinematic quantities from object level distributions to event level correlations in the two and four tag selections are expected to differ. Figure 4.32 shows the relevant kinematic distributions in the sideband region after the pseudo-tagging, which includes the following object level distributions:

1. 4th leading jet p_T from the Higgs candidate which is relevant to the pseudo-tagged jets, up to 80 GeV.
2. 2nd leading jet p_T from the Higgs candidate which is relevant to the pseudo-tagged jets.
3. Mean of the $|\eta|$ of 4 b -jets: $\langle |\eta_i| \rangle = \frac{1}{4} \sum_{i=1}^{i=4} |\eta_i|$.
4. ΔR_{bb} of the two closest jets out of the four selected for Higgs Candidate (HC) construction.
5. ΔR_{bb} of the other two HC jets.

As we can see the χ^2/NDF of the distributions in Figure 4.32, these five variables have slight mis-modeling, where the largest χ^2/NDF is 3.95 for the ΔR_{bb} . In results, the m_{4b} distribution might have slight mis-modeling, which means a 2.7σ deviation is observed in the bin at $m_{4b} = 350$ GeV and the χ^2/NDF is 2.63. To improve the agreement between the dataset in the $4b$ region and pseudo-tagged dataset in the $2b$ region, a “kinematic reweighting” procedure using the above five variables is performed. The procedure is as follows:

1. Fill histograms of the five reweighting distributions separately for two and four b -tag data and $t\bar{t}$ MC. Weight the histogram entries in the $2b$ region with a product over the reweighting functions from previous iterations:

Let F_i^a denote the reweighting functions where $a \in A$ specifies the reweighting distribution from the set of five variables A , and i specifies the iteration starting from 0. For a given event let x_a be the value of the kinematic variable denoted by a . Let I be the current iteration.

The simplest method is:

$$w(x_1, x_2, \dots, x_5) = \text{nJetWeight} \times \prod_{i=0}^{i<I} \prod_{a \in A} F_i^a(x_a) \quad (4.16)$$

2. Normalize the all hadronic $t\bar{t}$ and the QCD multi-jet background in the Control region
3. Subtract the two and four tag $t\bar{t}$ MC histograms from the two and four tag data respectively.
4. Take the ratio of (four tag $t\bar{t}$ subtracted)/(two tag $t\bar{t}$ subtracted) reweighting histograms
5. Smooth the ratio to reduce impact of local statistical fluctuations and define the smoothed line as F_i^a
6. Repeat steps 1-5 until $F_i^a(x_a) \approx 1$ for all $a \in A$

Where $p_{T\ i}$, η_i denote the transverse momentum and pseudo rapidity of the i th jet among four jets selected to build Higgs candidates sorted by p_T . The reweighting of $p_{T\ 4}$, $p_{T\ 2}$ and $\langle|\eta_i|\rangle$ are motivated primarily by the p_T and η dependence of b -tagging efficiency while the ΔR_{bb} 's are reweighted to account for differences in di-jet correlations from the underlying scattering processes.

The kinematic reweighting has been executed for 2016–2018 dataset. Since the pseudo-tag rate for datasets of all years are consistent with 1σ according to Table 4.7, the kinematics reweighting factor has been derived using combination of datasets of all years to perform the reweighting with enough statistics. Figure 4.31 shows the distribution of invariant mass of the 4 b-jets for each number of iterations. The ratio plots shows the ratio of the m_{4j} at iteration of i and $i - 1$. The reweighting converges with iteration 3, sufficiently. Figure 4.33 shows the distributions of observables at iteration 3. Table 4.16 summarizes the χ^2/NDF of the distributions of the five variables used for the reweighting and m_{4b} at each iteration of the reweighting. The χ^2/NDF becomes close to 1 after the reweighting. The distributions of the corresponding observables in validation region at iteration 0 and 3 are shown in Figure 4.34 and Figure 4.35. The χ^2/NDF of the distributions in the validation region is improved after the reweighting, too.

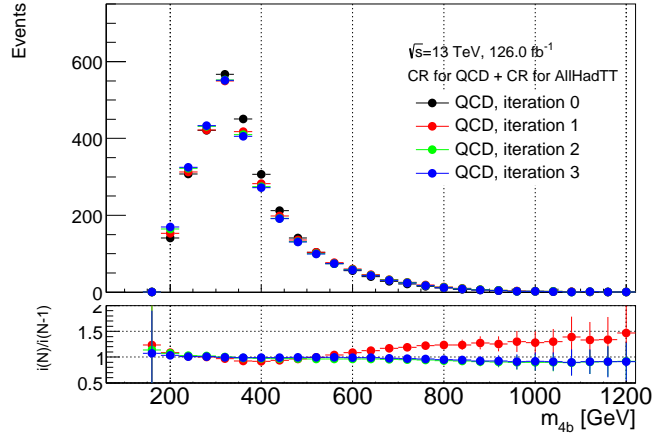


Figure 4.31: The distribution of invariant mass of the 4 b-jets of QCD background for each number of iterations.

Table 4.16: χ^2/NDF of the distributions in the sideband region for each iteration.

	iter. 0	iter. 1	iter. 2	iter. 3
m_{4b}	2.63	2.40	1.81	1.60
$p_{T\ 4}$, up to 80 GeV	0.93	0.94	0.85	0.83
$p_{T\ 2}$	1.24	1.50	0.95	0.78
$\langle \eta_i \rangle = \frac{1}{4} \sum_{i=1}^{i=4} \eta_i $	1.71	1.44	1.39	1.38
ΔR_{jj} of the two closest HC jets	2.50	0.41	0.41	0.42
ΔR_{jj} of the other two HC jets	3.95	1.34	0.77	0.62

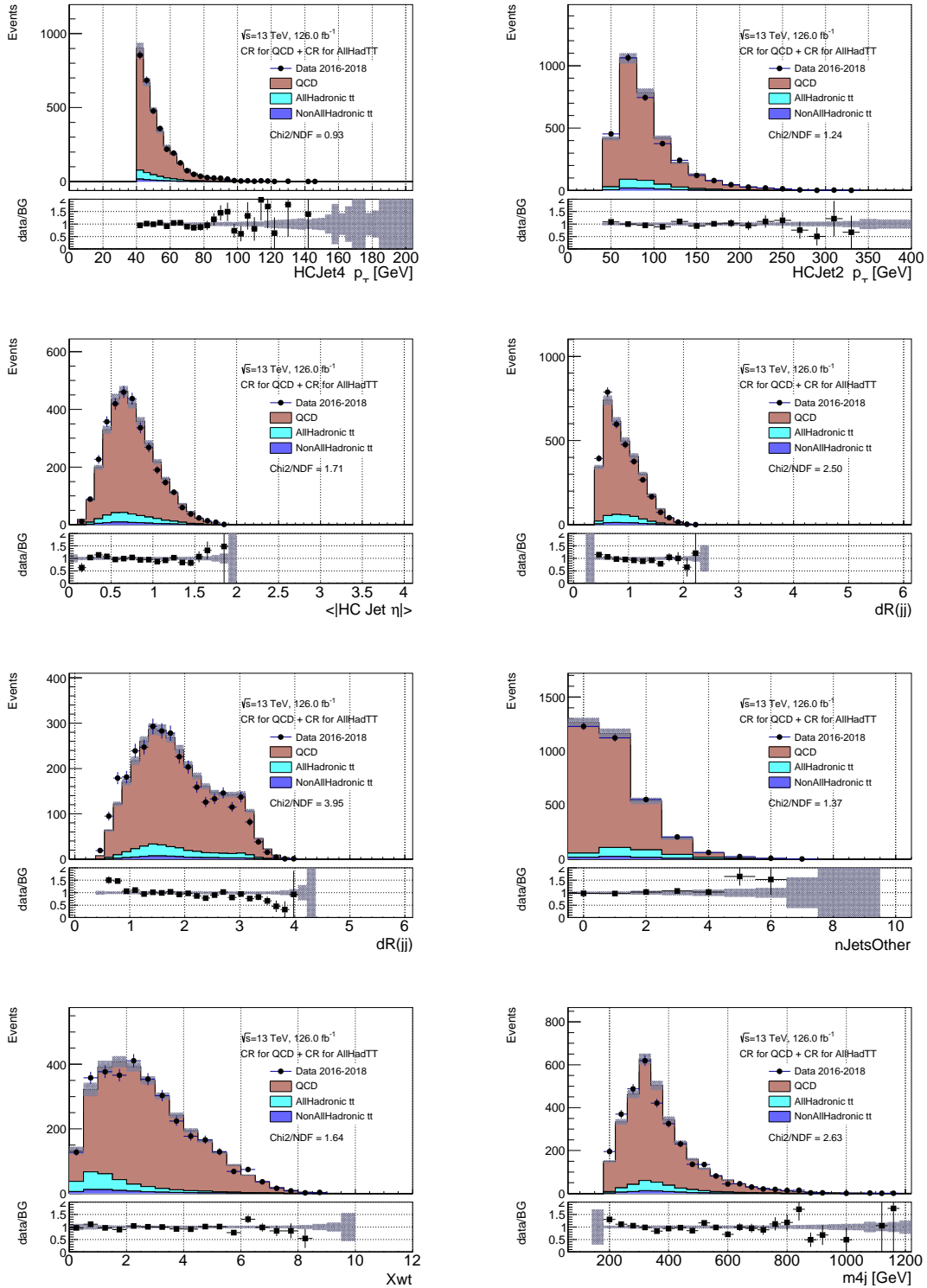


Figure 4.32: Distributions in sideband region before kinematic reweighting. Starting from the top and moving left to right, the distributions are: (a) 4th leading jet p_T of the Higgs jets, (b) Sub-leading jet p_T of the Higgs jets (c) The average of the eta of 4 HC jets, (d) ΔR of the two closest jets out of the four selected for Higgs candidate construction, (e) ΔR of the other two HC jets (f) nJetOther (non Higgs jets in the central η region), (g) X_{wt} , the top identification variable, (h) m_{4j} , the invariant mass of the Higgs candidates.

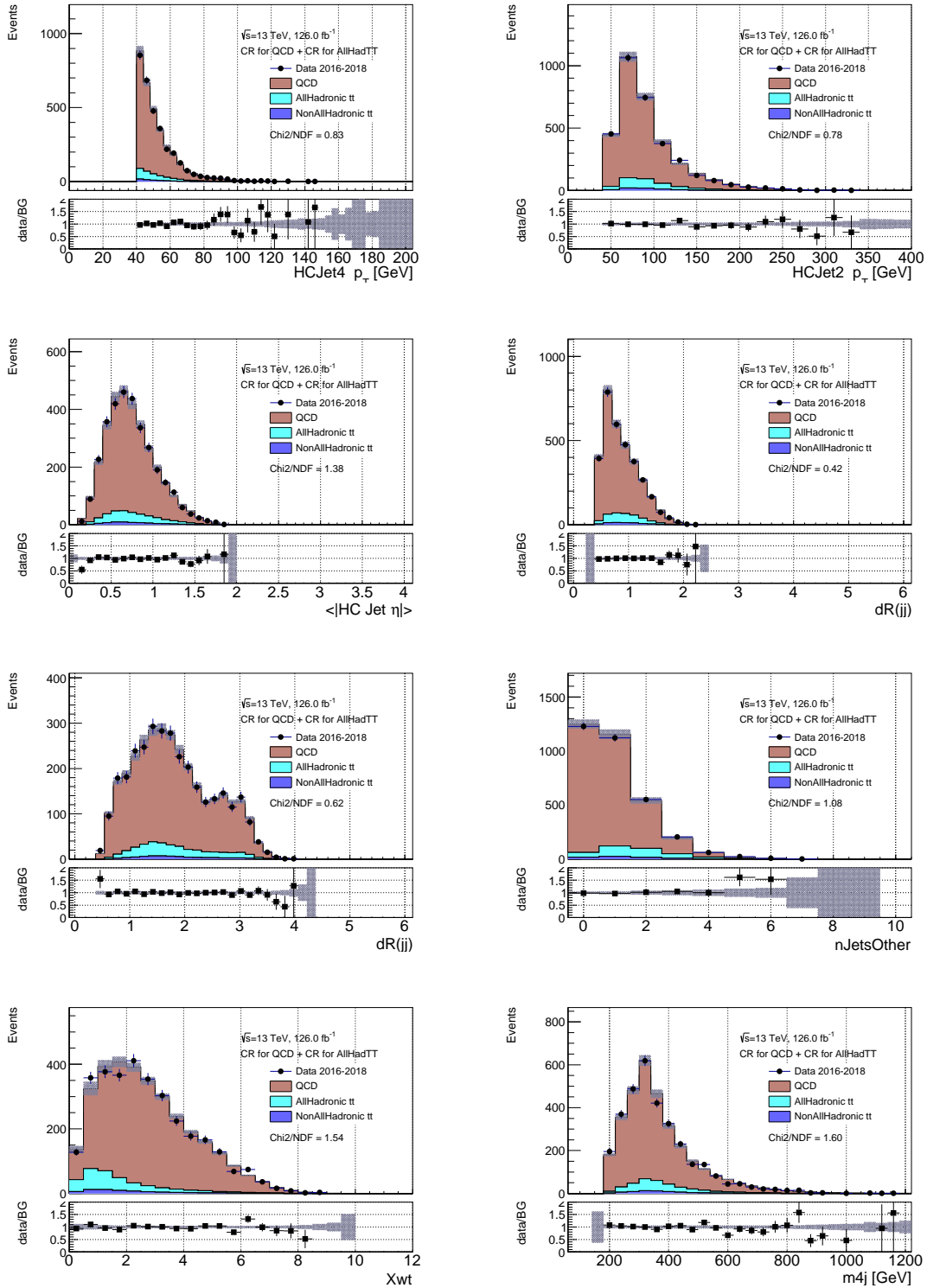


Figure 4.33: Distributions in sideband region after kinematic reweighting with iteration 3. Starting from the top and moving left to right, the distributions are: (a) 4th leading jet p_T of the Higgs jets, (b) Sub-leading jet p_T of the Higgs jets (c) The average of the eta of 4 HC jets, (d) ΔR of the two closest jets out of the four selected for Higgs candidate construction, (e) ΔR of the other two HC jets (f) nJetOther (non Higgs jets in the central η region), (g) X_{Wt} , the top identification variable, (h) m_{4j} , the invariant mass of the Higgs candidates.

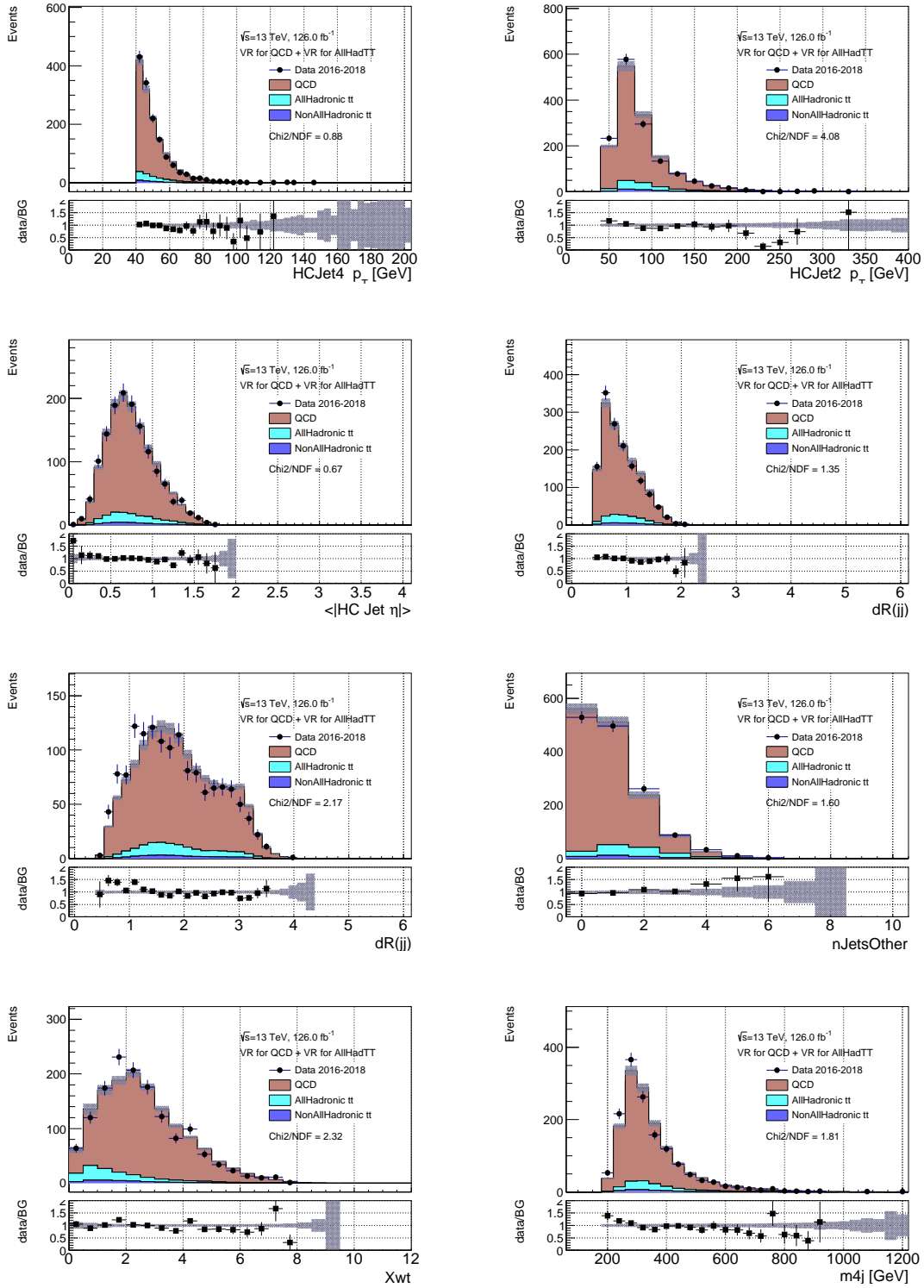


Figure 4.34: Distributions in validation region before kinematic reweighting. Starting from the top and moving left to right, the distributions are: (a) 4th leading jet p_T of the Higgs jets, (b) Sub-leading jet p_T of the Higgs jets (c) The average of the eta of 4 HC jets, (d) ΔR of the two closest jets out of the four selected for Higgs candidate construction, (e) ΔR of the other two HC jets (f) nJetOther (non Higgs jets in the central η region), (g) X_{wt} , the top identification variable, (h) m_{4j} , the invariant mass of the Higgs candidates.

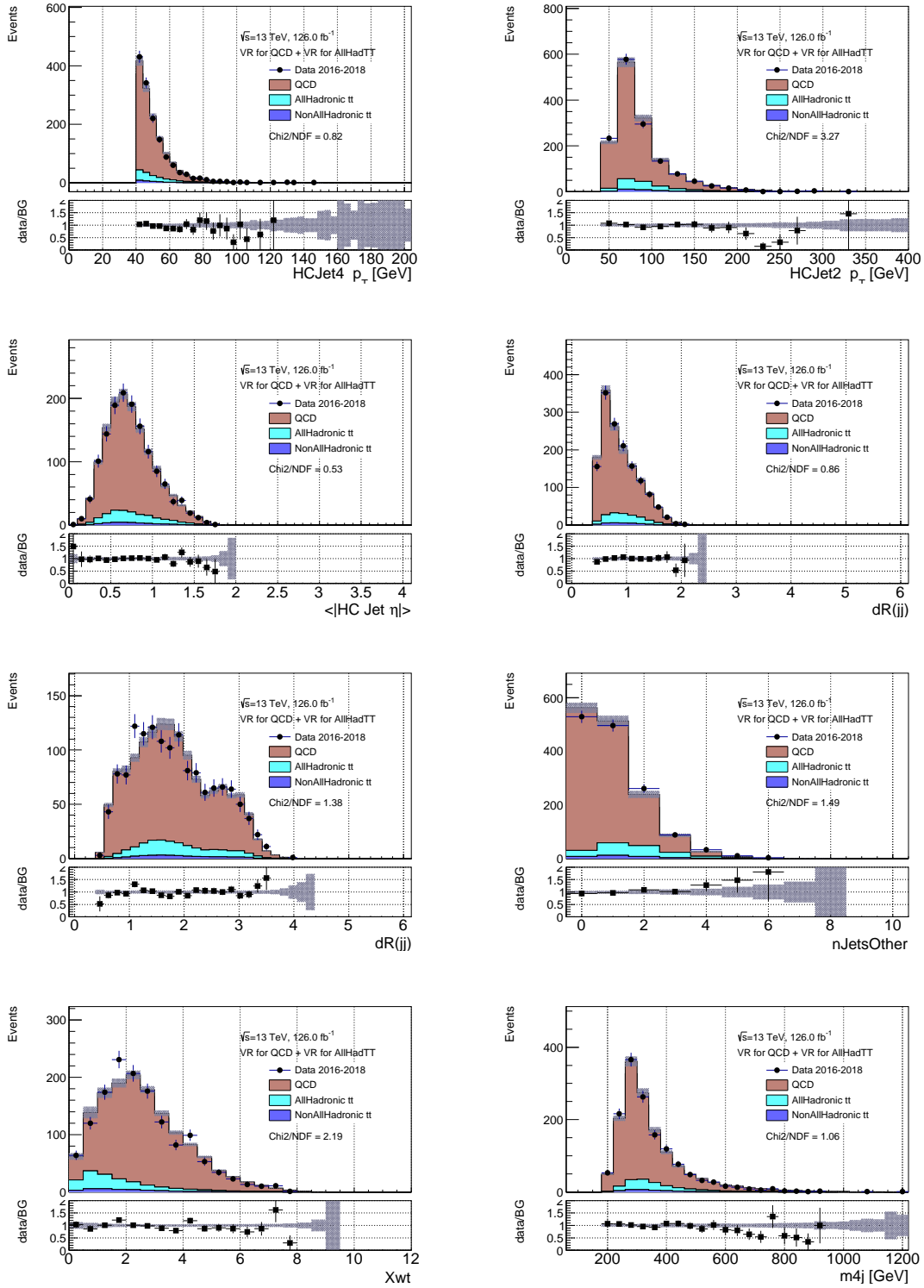


Figure 4.35: Distributions in validation region after kinematic reweighting with iteration 3. Starting from the top and moving left to right, the distributions are: (a) 4th leading jet p_T of the Higgs jets, (b) Sub-leading jet p_T of the Higgs jets (c) The average of the eta of 4 HC jets, (d) ΔR of the two closest jets out of the four selected for Higgs candidate construction, (e) ΔR of the other two HC jets (f) nJetOther (non Higgs jets in the central η region), (g) X_{wt} , the top identification variable, (h) m_{4j} , the invariant mass of the Higgs candidates.

4.7.5 The other backgrounds

Several small other backgrounds can potentially contribute. Hadronic Z decays, ttH production, and di-boson production, and ttZ production were tested in MC. The expected contribution in the signal region was largest for ttH semi-leptonic production at 0.17 events. All other contributions were significantly smaller. As these backgrounds are all negligible, they are not included in further studies.

4.7.6 Normalization in the control regions

The X_{Wt} distributions of 2016-2018 dataset with loosened selections are shown in Figure 4.36. As a reminder, the region of $X_{Wt} < 0.75$ is defined as the control region for all hadronic $t\bar{t}$ and the region of $0.75 < X_{Wt}$ is defined as the control region for the QCD multi-jet background. The "Negative Extended Log Likelihood" is minimized in the CRs for the QCD multi-jet background and the all hadronic $t\bar{t}$ background with binned fitting. The scale factors for the normalization are μ_{QCD} and μ_{AllHadTT} for the QCD multi-jet background and the all hadronic $t\bar{t}$ background, respectively, defined as below:

$$\mu_{\text{QCD}} = N_{(\text{QCD in } 4b)} / N_{(\text{data in } 2b; \text{ pseudo-tagged})}, \quad (4.17)$$

$$\mu_{\text{AllHadTT}} = N_{(t\bar{t} \text{ in } 4b)} / N_{(t\bar{t} \text{ MC in } 2b; \text{ pseudo-tagged})}, \quad (4.18)$$

where $N_{(\text{QCD in } 4b)}$ and $N_{(t\bar{t} \text{ in } 4b)}$ are the ideal yields of the QCD multi-jet background and $t\bar{t}$ background in the $4b$ region, respectively. The $N_{(\text{data in } 2b; \text{ pseudo-tagged})}$ and $N_{(t\bar{t} \text{ MC in } 2b; \text{ pseudo-tagged})}$ are the yields of pseudo-tagged QCD multi-jet background and $t\bar{t}$ background in the $2b$ region, respectively. The results of the fitting are summarized in Table 4.17. The statistical uncertainty of μ_{QCD} is $\sim 10\%$ relative to the central value. The yields of each backgrounds in the validation region and the signal region are shown in Table 4.18. In the both of signal region and CR, the QCD multi-jet background is $\sim 95\%$ of total. The value of μ_{AllHadTT} is somewhat large, and is driven by the larger yields in data of the X_{Wt} variable, though there is a large uncertainty. Overall agreement in the CRs and VRs remains very good.

Table 4.17: The results of normalization for 2016, 2017, and 2018 dataset.

dataset	μ_{QCD}	μ_{AllHadTT}
2016	0.331 ± 0.023	2.46 ± 0.98
2017	0.411 ± 0.021	2.84 ± 0.84
2018	0.301 ± 0.014	1.94 ± 0.63

Table 4.18: The statistics and roughly estimated background yields in the validation region (VR) and the signal region (SR).

region	Data	total bkg.	multi-jet	all hadronic $t\bar{t}$	non-all hadronic $t\bar{t}$
VR	189	176.3 ± 9.0	163.9 ± 8.1	10.4 ± 4.0	2.0 ± 0.1
SR	333	321.2 ± 16.1	296.6 ± 14.4	21.0 ± 4.6	3.7 ± 0.2

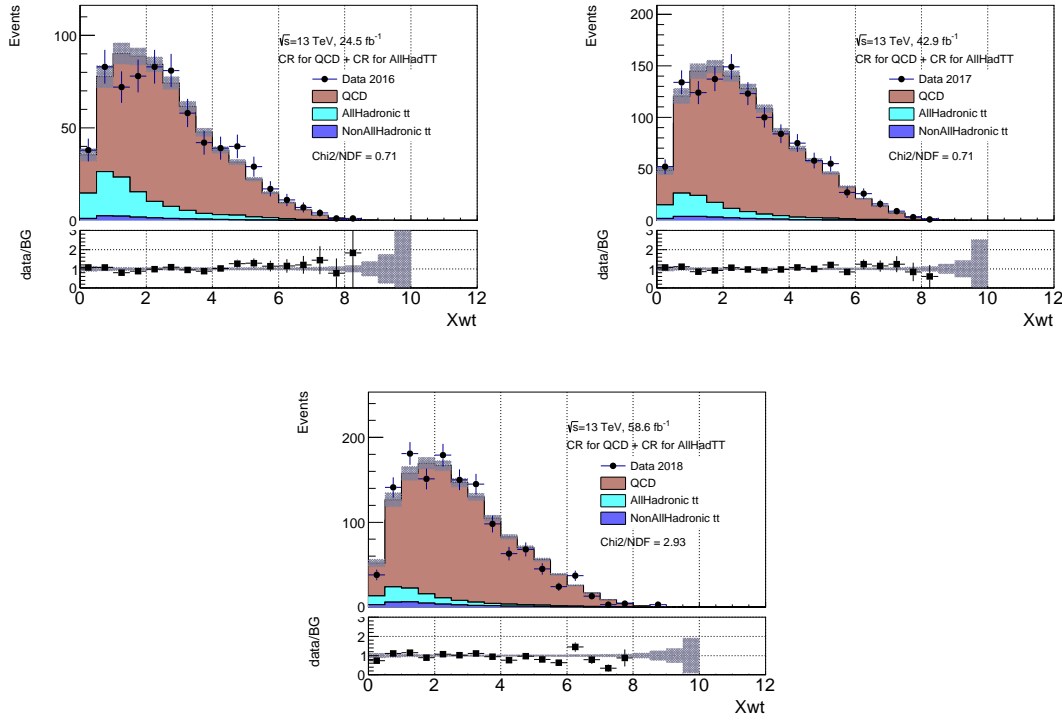


Figure 4.36: Post-fit X_{Wt} distributions with loosened selection [$m_{jj} > 0$ [GeV], $\Delta\eta_{jj} > 4$, VectorSum $p_T < 1000$ [GeV]] in sideband region for 2016, 2017, and 2018. The fit normalization is described in Section 4.7.6.

4.8 Systematic uncertainty

The possible systematics are listed below:

- Systematic from signals
 - Luminosity ($\pm 1.7\%$)
 - Detector-based uncertainties (Jet energy scale, Jet energy resolution, b -tagging, and b -trigger)
 - Theoretical uncertainties
- Systematic from QCD multi-jet background
 - Statistic uncertainty of normalization in CR
 - Shape uncertainties derived from the background model using data from the control region and sideband region
- Systematic from all hadronic $t\bar{t}$ background
 - Statistic uncertainty of normalization in CR
 - Shape uncertainties associated with the use of two-tag simulation to model $4b$ -tag distributions
 - Standard modeling uncertainties (generator, radiation, parton shower)

- Systematic from non all hadronic $t\bar{t}$ background
 - Luminosity ($\pm 1.7\%$)
 - Theoretical uncertainty on the cross-section from the variation of the renormalization and factorization factor
 - Detector-based uncertainties (Jet energy scale, Jet energy resolution, b -tagging, and b -trigger)
 - Shape uncertainties associated with the use of two-tag simulation to model $4b$ -tag distributions
 - Standard modeling uncertainties (generator, radiation, parton shower)

4.8.1 Systematic from signals

Detector-based uncertainties

The uncertainties from the Jet Energy Scale (JES) and Jet Energy Resolution (JER) that come from the jet calibration described in Section 3.4.1 are parametrized by 32 independent uncertainties modeled from each calibration step. These 32 uncertainties are treated as independent nuisance parameters in the statistical analysis. The m_{4b} distributions in the signal region with JES and JER uncertainties for resonant signals are shown in Figure 4.37 and 4.38, respectively. The JES and JER uncertainty is about 20%.

The b -tagging has also independent 40 uncertainties modeled from each algorithm. These uncertainties are treated as independent nuisance parameter in the statistical analysis too. The m_{4b} distributions in the signal region with b -tagging scale factors (SFs) are shown in Figure 4.40 and 4.41. The uncertainties comes from the estimation of the trigger efficiency that is described in Section 4.5 has been also included. The origin of the event-level uncertainty is the uncertainty of the measurement of the jet-level trigger efficiency that is described in Section 4.5. The m_{4b} distributions in the signal region with trigger SFs are shown in Figure 4.43 and 4.44 and 4.45. The impact of the b -tagging SFs and trigger SFs are found to be smaller than that of JES and JER uncertainties. The distributions with $\pm\sigma$ of each uncertainties are overlaid and the important point is contained in the ratios: none of the ratios show large variations of the MC with the systematic variation, especially in the regions with significant statistics. The uncertainties from the b -tagging SFs, trigger SFs, JES and JER are shown in the figures in the section 4.10 as `Signal_bSF*`, `Signal_TrigSF*`, and each name of the JES and JER nuisance parameters, respectively.

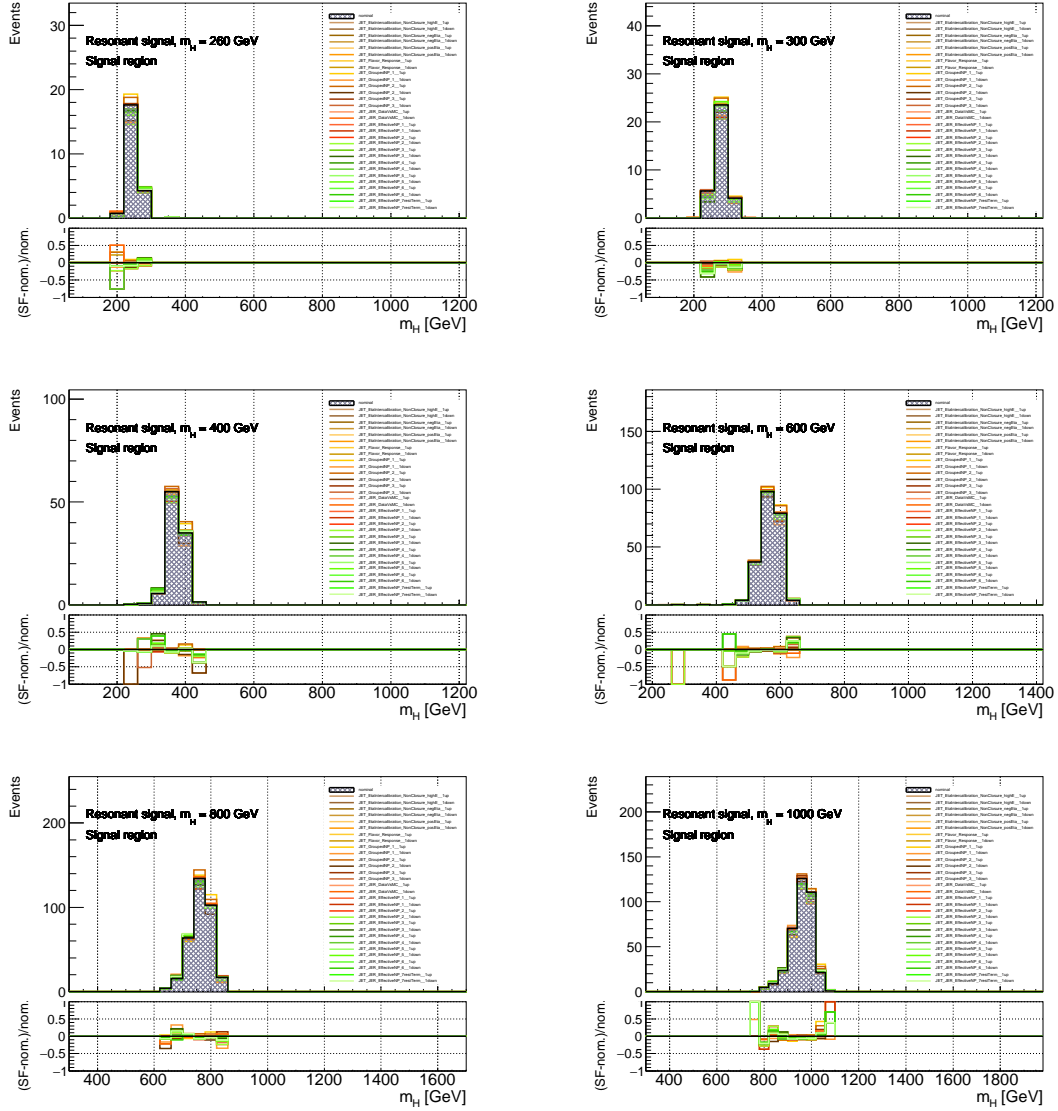


Figure 4.37: The distribution for the MC sample for 2016 of the resonant signal with narrow width (4 MeV) with JES and JER uncertainties. Each histogram is the case of $m_H = 260$ GeV (top left), $m_H = 300$ GeV (top right), $m_H = 400$ GeV (middle left), $m_H = 600$ GeV (middle right), $m_H = 800$ GeV (bottom left), and $m_H = 1000$ GeV (bottom right)

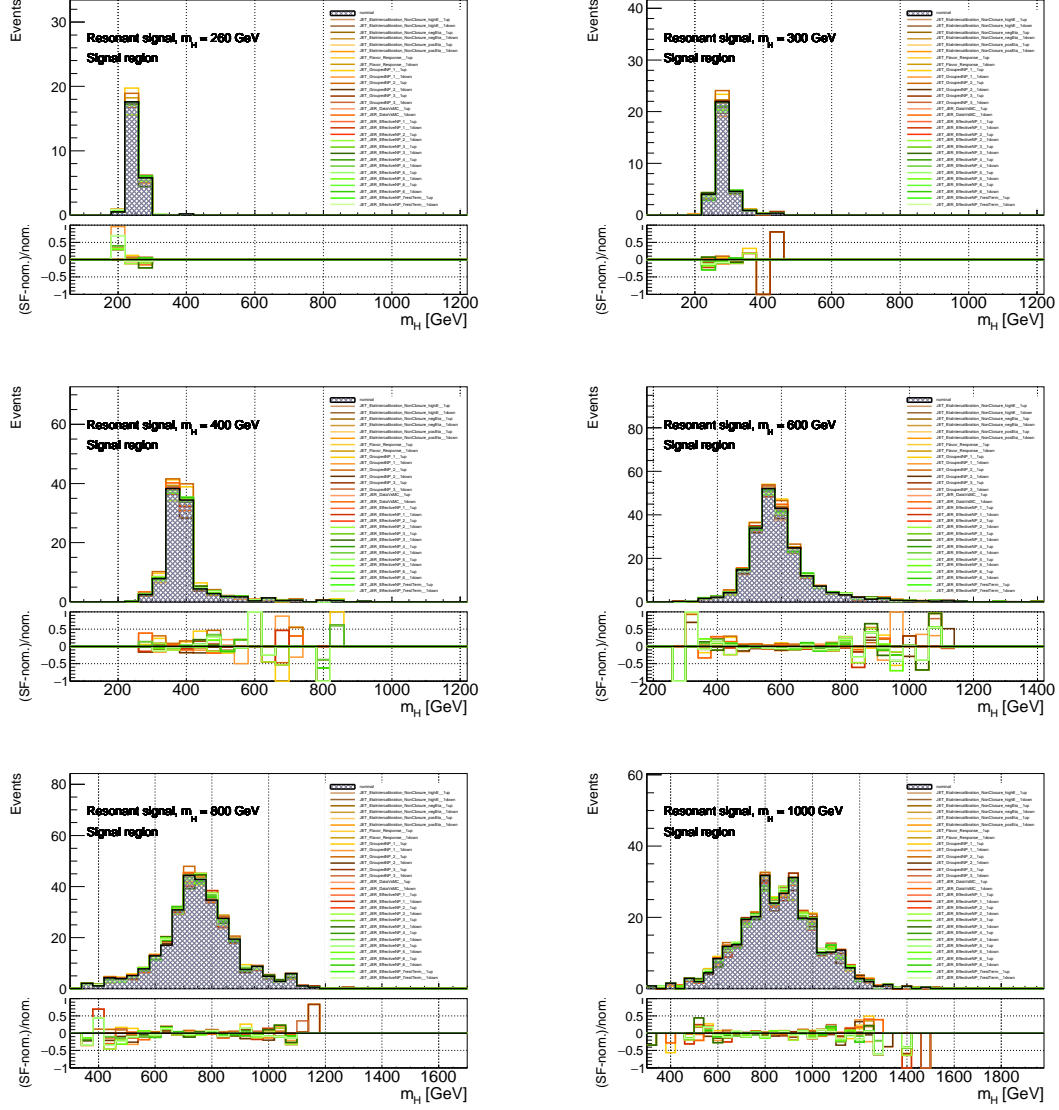


Figure 4.38: The distribution for the MC sample for 2016 of the resonant signal for $\tan \beta = 2.0$ and $\sin(\beta - \alpha) = 0.6$ in Type-II 2HDM with JES and JER uncertainties. Each histogram is the case of $m_H = 260$ GeV (top left), $m_H = 300$ GeV (top right), $m_H = 400$ GeV (middle left), $m_H = 600$ GeV (middle right), $m_H = 800$ GeV (bottom left), and $m_H = 1000$ GeV (bottom right).

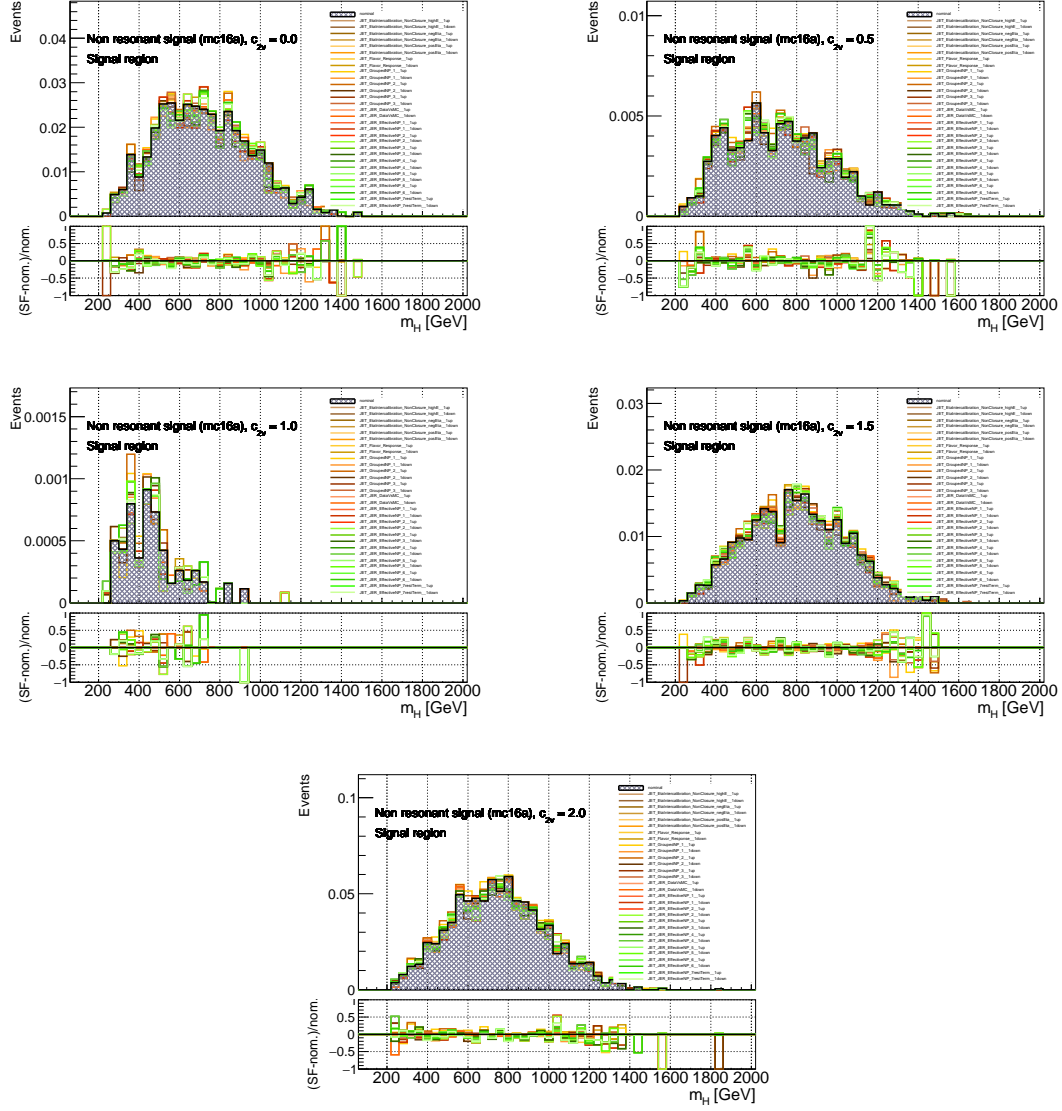


Figure 4.39: The distribution for the MC sample for 2016 of the non-resonant signal with JES and JER uncertainties. Each histogram is the case of $\kappa_{2V} = 0.0$ (top left), $\kappa_{2V} = 0.5$ (top right), $\kappa_{2V} = 1.0$ (middle left), $\kappa_{2V} = 1.5$ (middle right), and $\kappa_{2V} = 2.0$ (bottom).

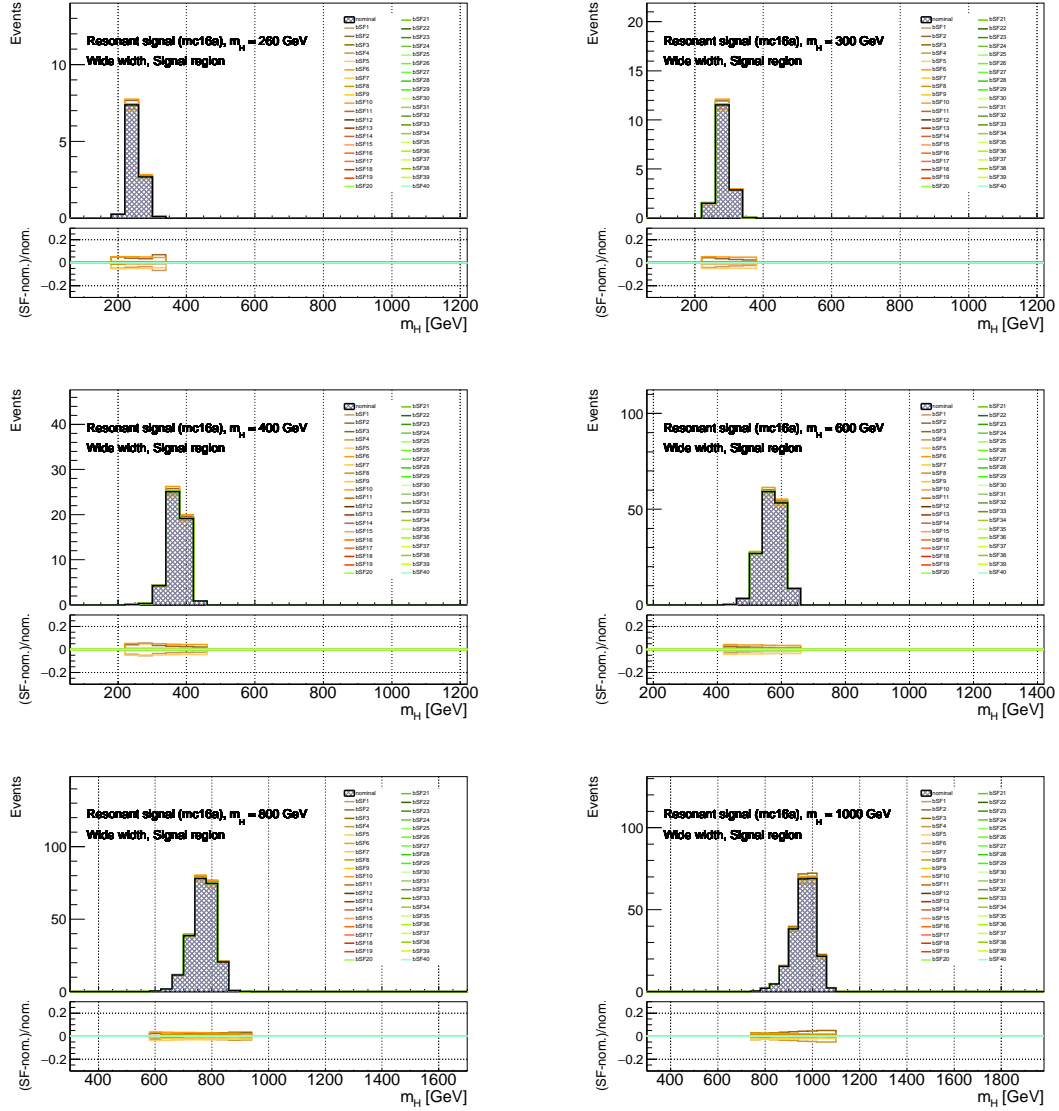


Figure 4.40: The distribution for the MC sample for 2016 of the resonant signal with narrow width (4 MeV) with b-tagging SFs. Each histogram is the case of $m_H = 260$ GeV (top left), $m_H = 300$ GeV (top right), $m_H = 400$ GeV (middle left), $m_H = 600$ GeV (middle right), $m_H = 800$ GeV (bottom left), and $m_H = 1000$ GeV (bottom right).

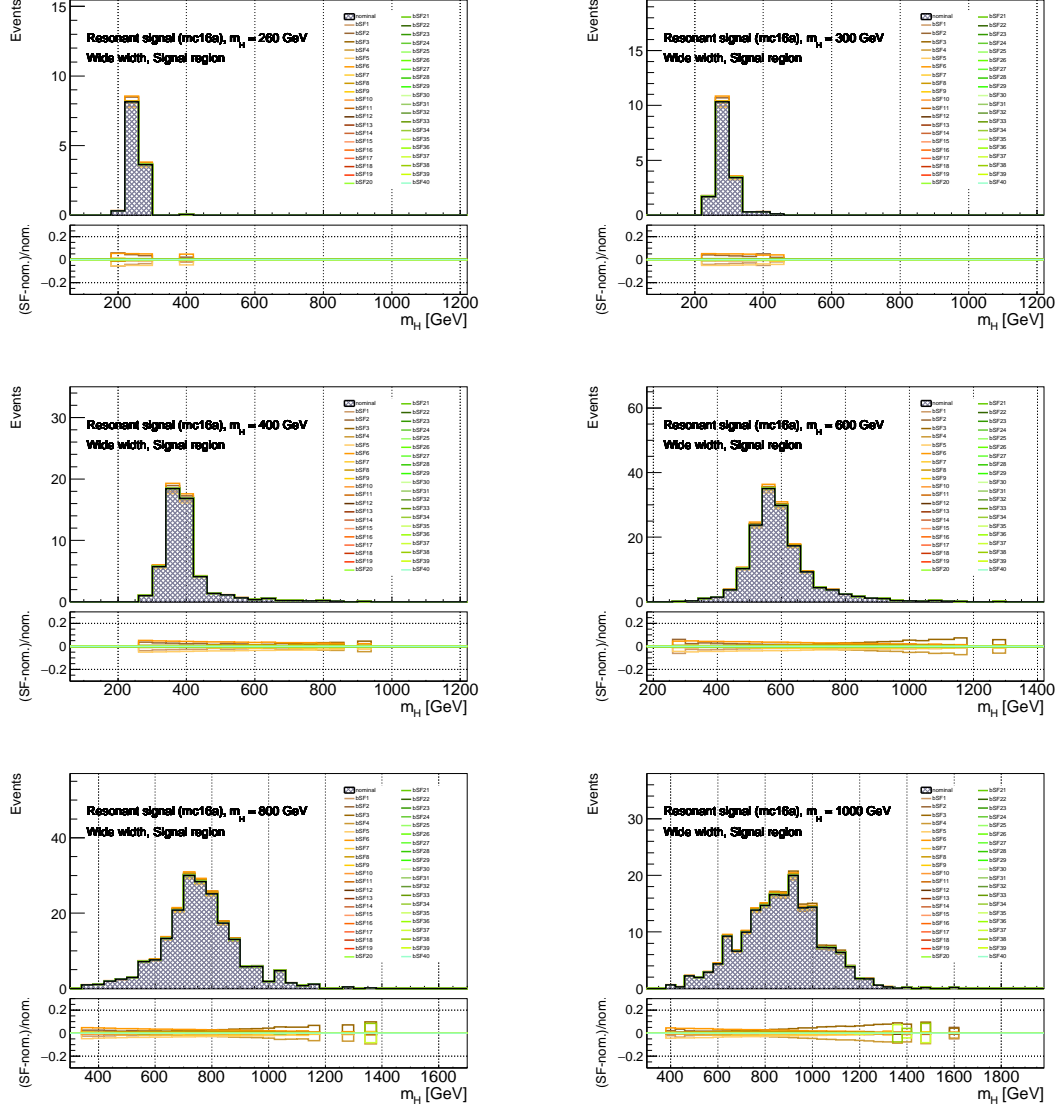


Figure 4.41: The distribution for the MC sample for 2016 of the resonant signal with wide width for $\tan \beta = 2.0$ and $\sin(\beta - \alpha) = 0.6$ in Type-II 2HDM with b-tagging SFs. Each histogram is the case of $m_H = 260$ GeV (top left), $m_H = 300$ GeV (top right), $m_H = 400$ GeV (middle left), $m_H = 600$ GeV (middle right), $m_H = 800$ GeV (bottom left), and $m_H = 1000$ GeV (bottom right).

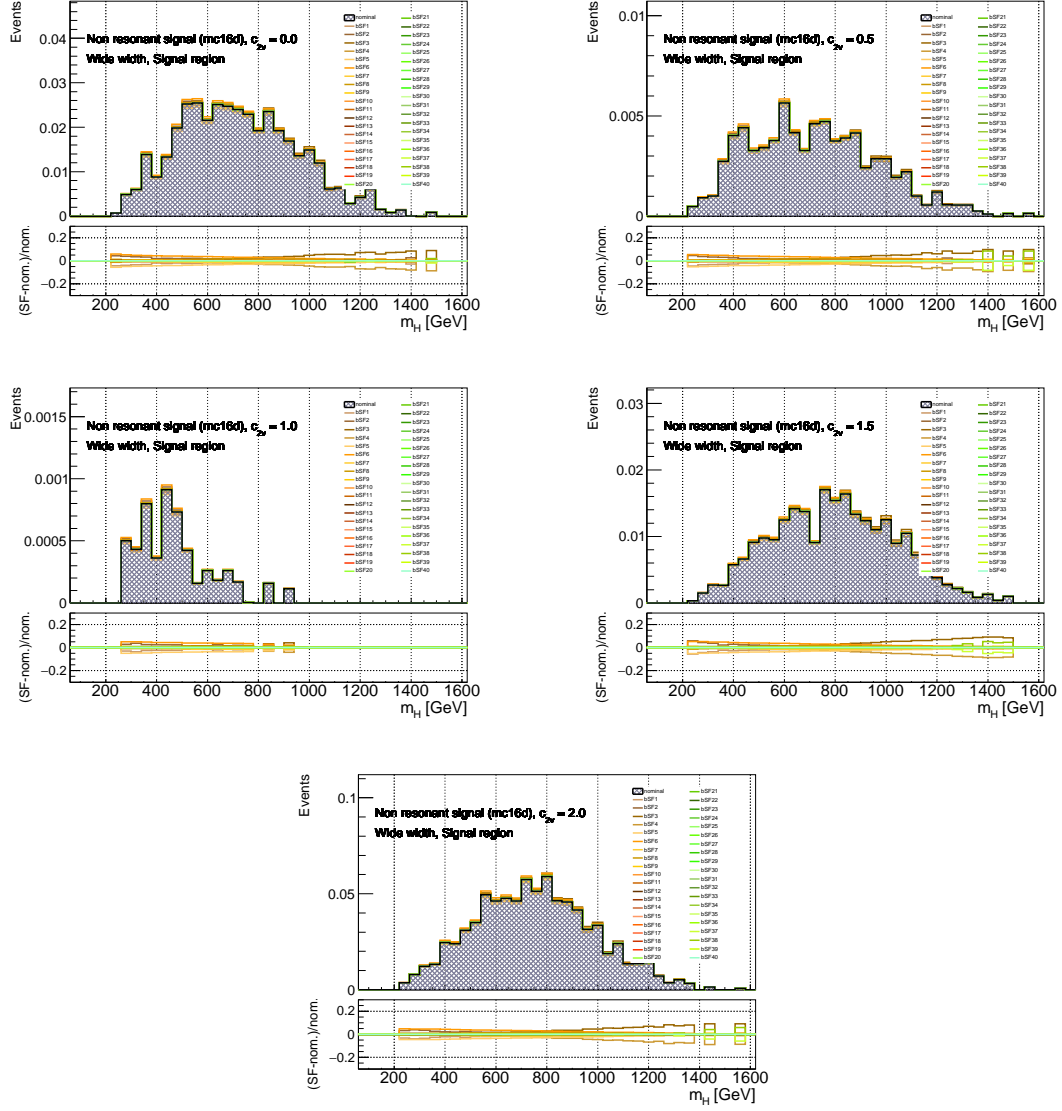


Figure 4.42: The distribution for the MC sample for 2016 of the non-resonant signal with b-tagging SFs. Each histogram is the case of $\kappa_{2V} = 0.0$ (top left), $\kappa_{2V} = 0.5$ (top right), $\kappa_{2V} = 1.0$ (middle left), $\kappa_{2V} = 1.5$ (middle right), and $\kappa_{2V} = 2.0$ (bottom).

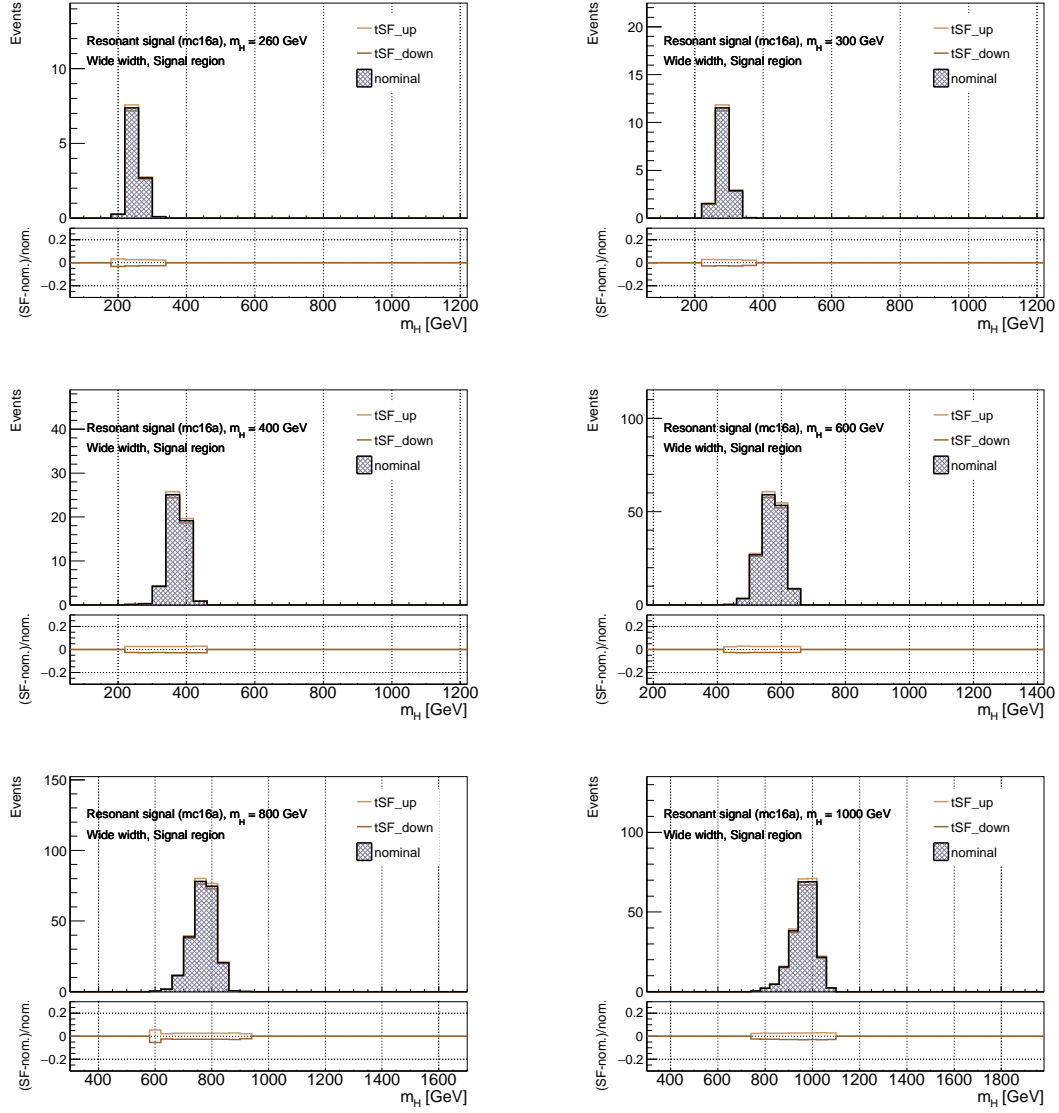


Figure 4.43: The distribution for the MC sample for 2016 of the resonant signal with narrow width (4 MeV) with jet-level trigger SF. Each histogram is the case of $m_H = 260$ GeV (top left), $m_H = 300$ GeV (top right), $m_H = 400$ GeV (middle left), $m_H = 600$ GeV (middle right), $m_H = 800$ GeV (bottom left), and $m_H = 1000$ GeV (bottom right).

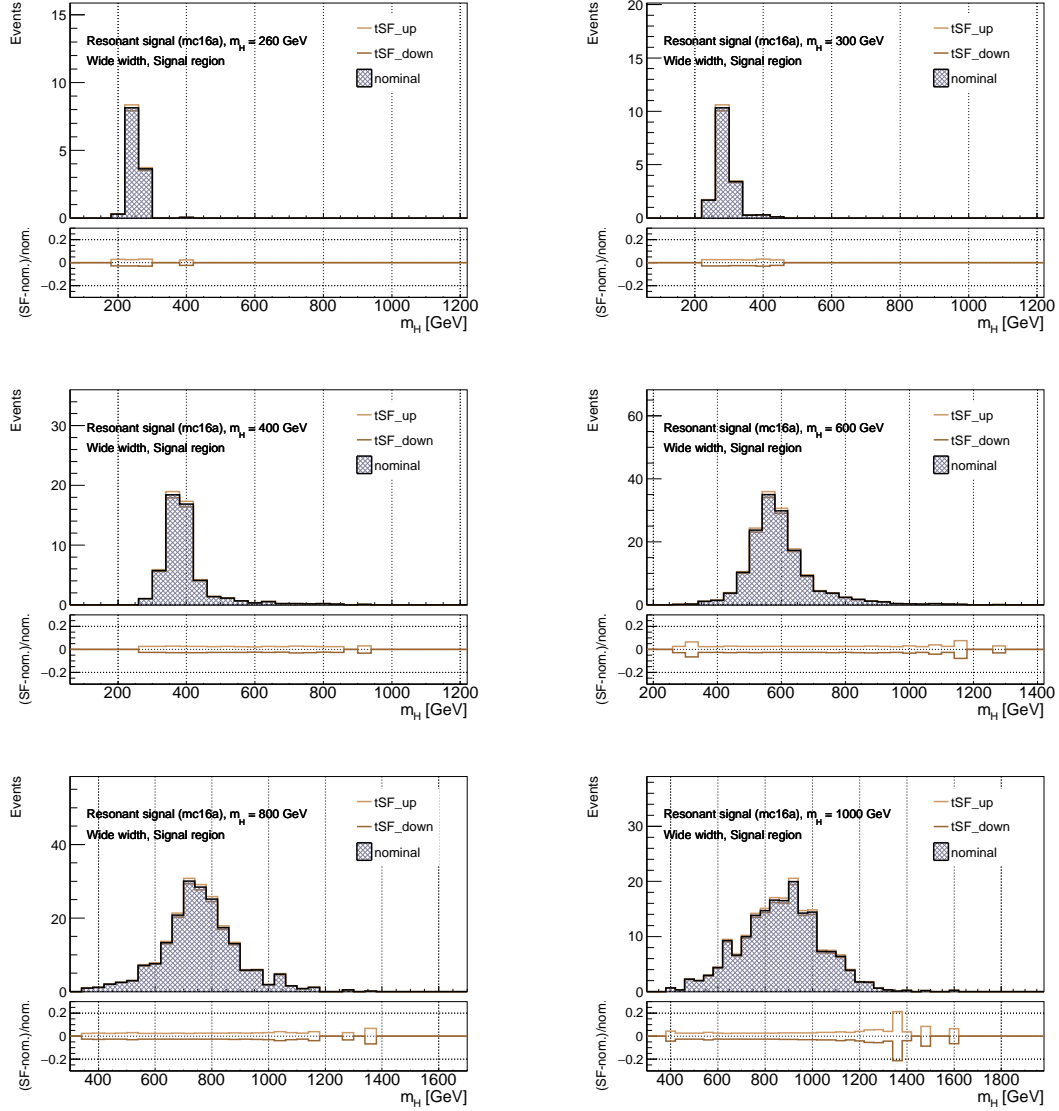


Figure 4.44: The distribution for the MC sample for 2016 of the resonant signal with wide width for $\tan\beta = 2.0$ and $\sin(\beta - \alpha) = 0.6$ in Type-II 2HDM with jet-level trigger SFs. Each histogram is the case of $m_H = 260$ GeV (top left), $m_H = 300$ GeV (top right), $m_H = 400$ GeV (middle left), $m_H = 600$ GeV (middle right), $m_H = 800$ GeV (bottom left), and $m_H = 1000$ GeV (bottom right).

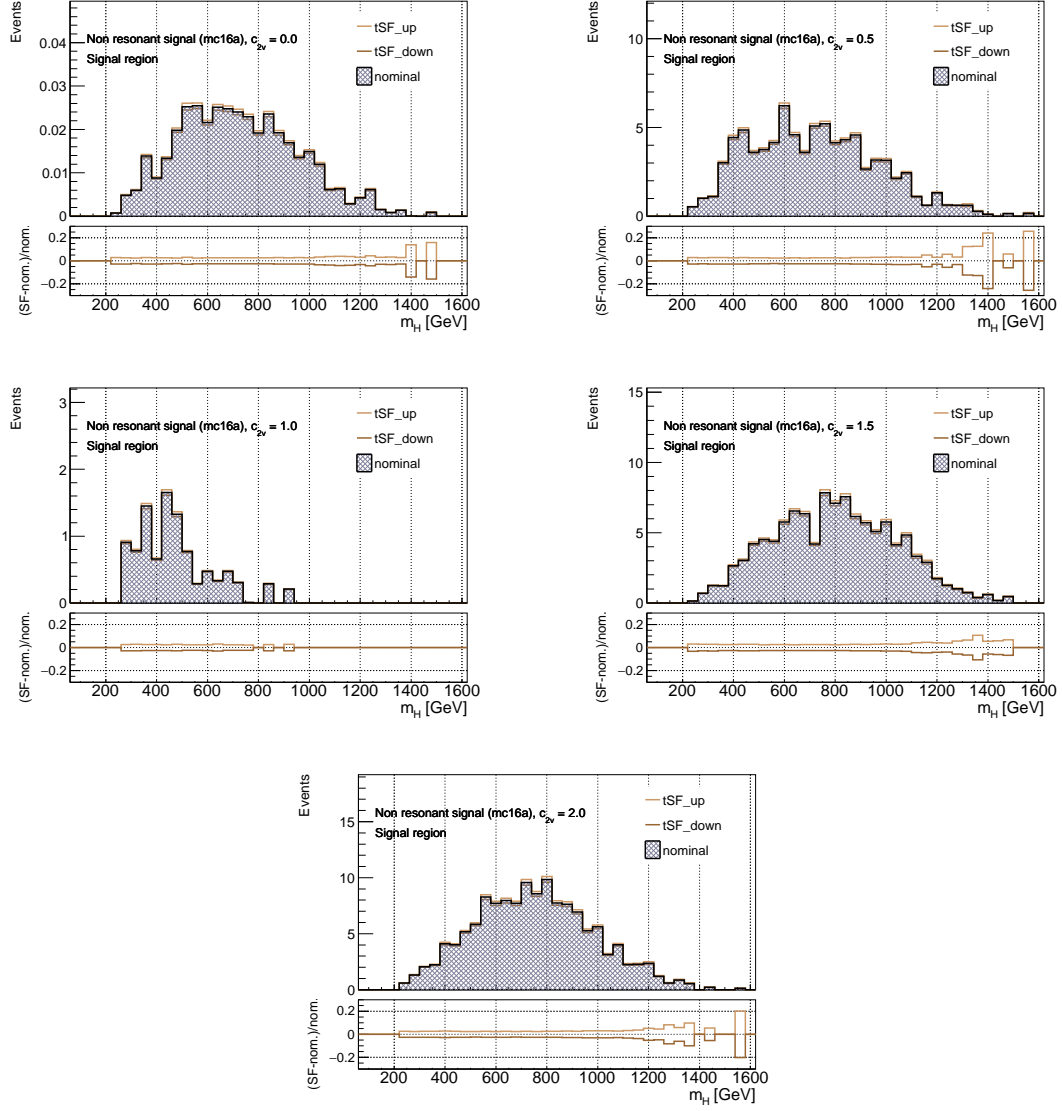


Figure 4.45: The distribution for 2016 of the non-resonant signal with jet-level trigger SFs. Each histogram is the case of $\kappa_{2V} = 0.0$ (top left), $\kappa_{2V} = 0.5$ (top right), $\kappa_{2V} = 1.0$ (middle left), $\kappa_{2V} = 1.5$ (middle right), and $\kappa_{2V} = 2.0$ (bottom).

Theoretical uncertainties

The theoretical uncertainty for the signal is investigated using truth samples with renormalization scale factor μ_R and factorization scale factor μ_F of 0.5/2.0 implemented in the generators. The m_{4b} distributions of the narrow width resonance with the variation of the factors are shown in Figure 4.46. The bin-by-bin non-closure derived from the ratio plots of nominal and systematics samples is included as systematics in the final fit. The ones of the wide width resonance and non-resonant signals are shown in Figure 4.47 and Figure 4.48, respectively. The uncertainties from the variation of the renormalization and factorization scale factors are shown in the figures in Section 4.10 as Signal_RF and Signal_FF, respectively.

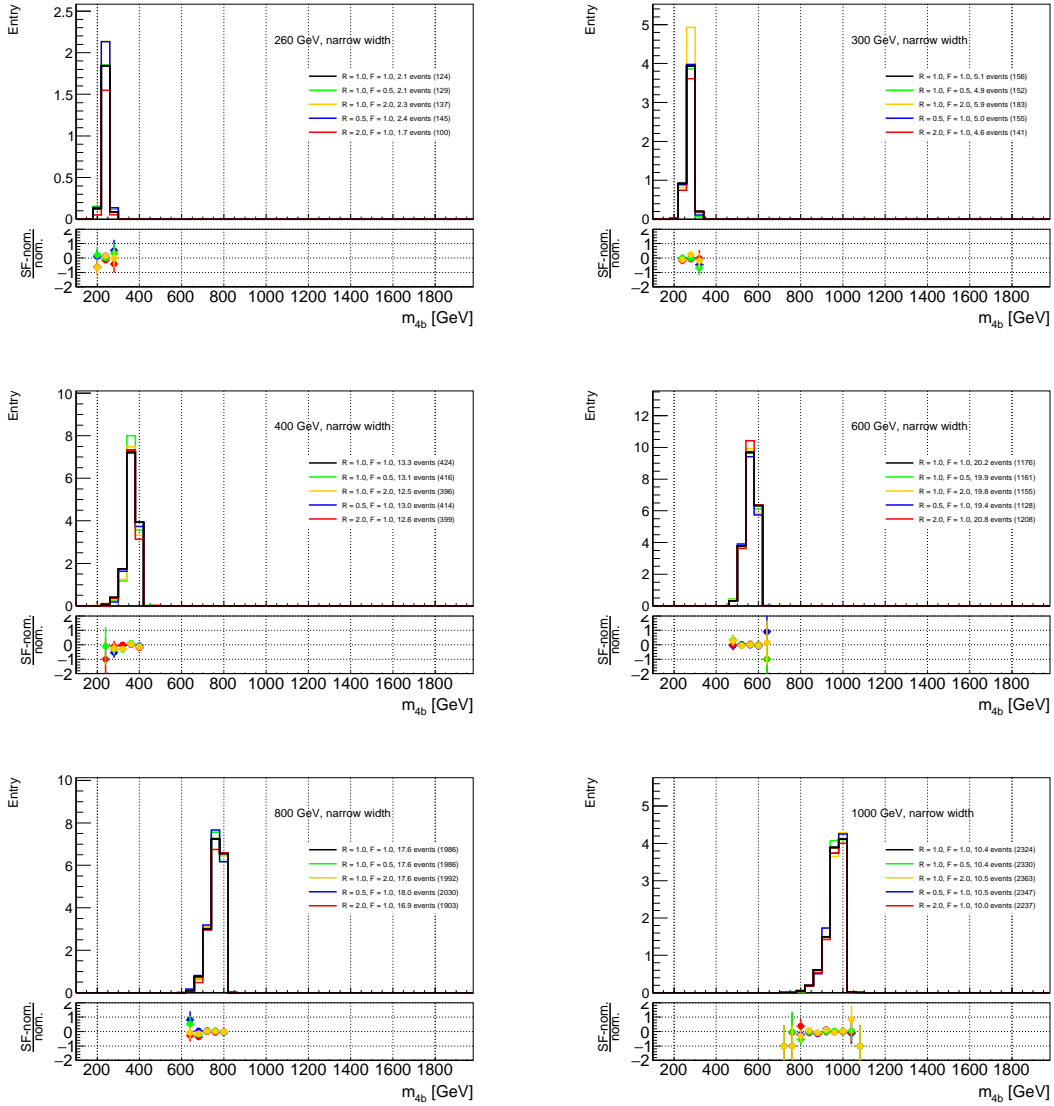


Figure 4.46: The m_{4b} distribution of truth samples of the resonant signal with narrow width (4 MeV) with the variation of the renormalization and factorization scale factor; $(\mu_R, \mu_F) = (1.0, 1.0), (1.0, 0.5), (1.0, 2.0), (0.5, 1.0), (2.0, 1.0)$. Each plot is the case of $m_H = 260$ GeV, 300 GeV, 400 GeV, 600 GeV, 800 GeV, and 1000 GeV.

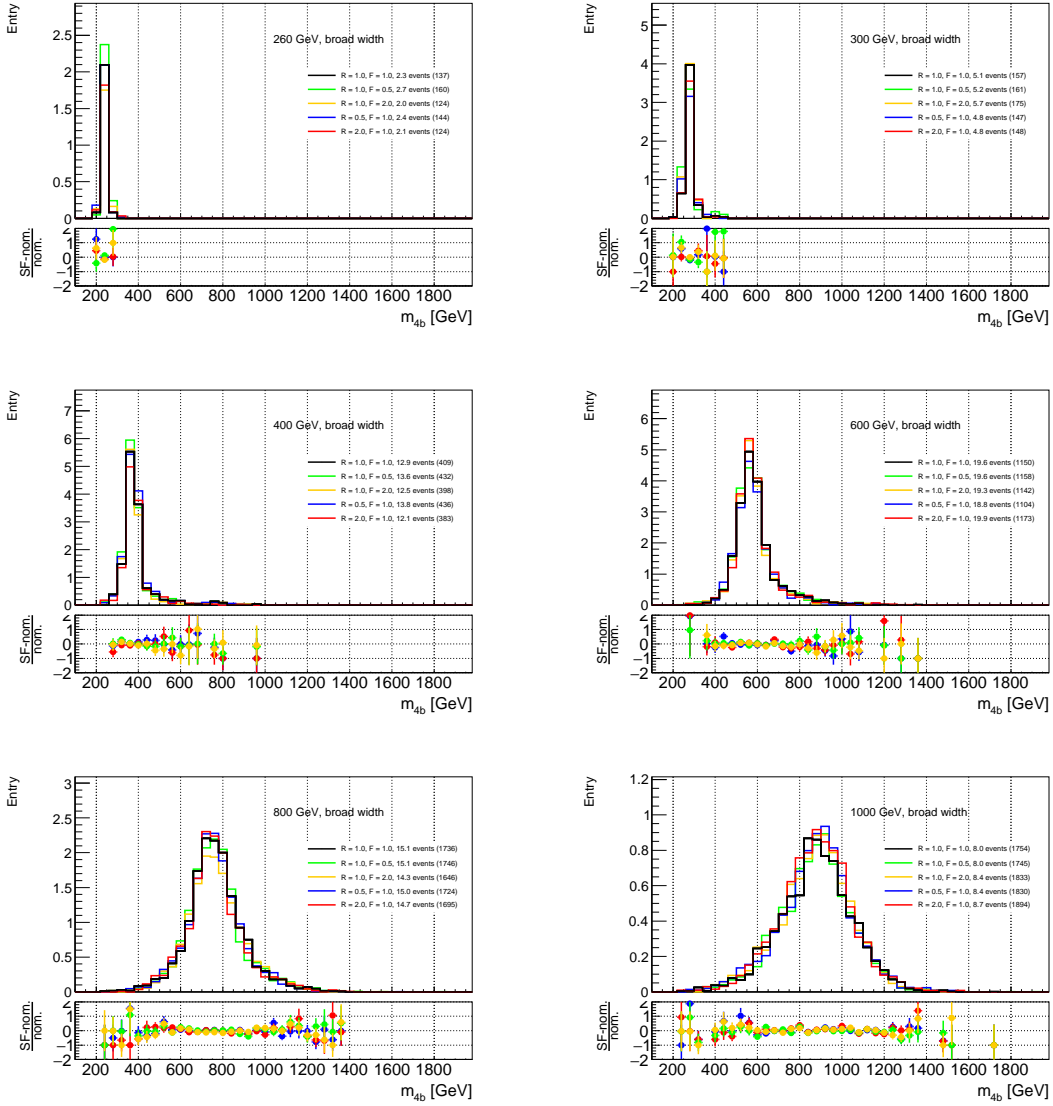


Figure 4.47: The m_{4b} distribution of truth samples of the resonant signal with wide width or $\tan\beta = 2.0$ and $\sin(\beta - \alpha) = 0.6$ in Type-II 2HDM with the variation of the renormalization and factorization scale factor; $(\mu_R, \mu_F) = (1.0, 1.0), (1.0, 0.5), (1.0, 2.0), (0.5, 1.0), (2.0, 1.0)$. Each plot is the case of $m_H = 260$ GeV, 300 GeV, 400 GeV, 600 GeV, 800 GeV, and 1000 GeV.

For the SM sample, the uncertainty from the parton shower generator is included. Figure 4.49 is the m_{4b} distribution of truth samples of non-resonant signals with two parton shower generators of Pythia8 and Herwig7. The uncertainty of the total yield is about 30%. This uncertainty is shown as Signal_Py8 in Section 4.10.

Trigger efficiency uncertainty

As described in Section 4.5, the uncertainty on the signal yields by the uncertainty from non-closure by assessing the difference between the emulated trigger result and the actual trigger simulation is $<10\%$. The uncertainties from that for the signals are shown in the figures in the section 4.10 as Signal_201*_trigNC.

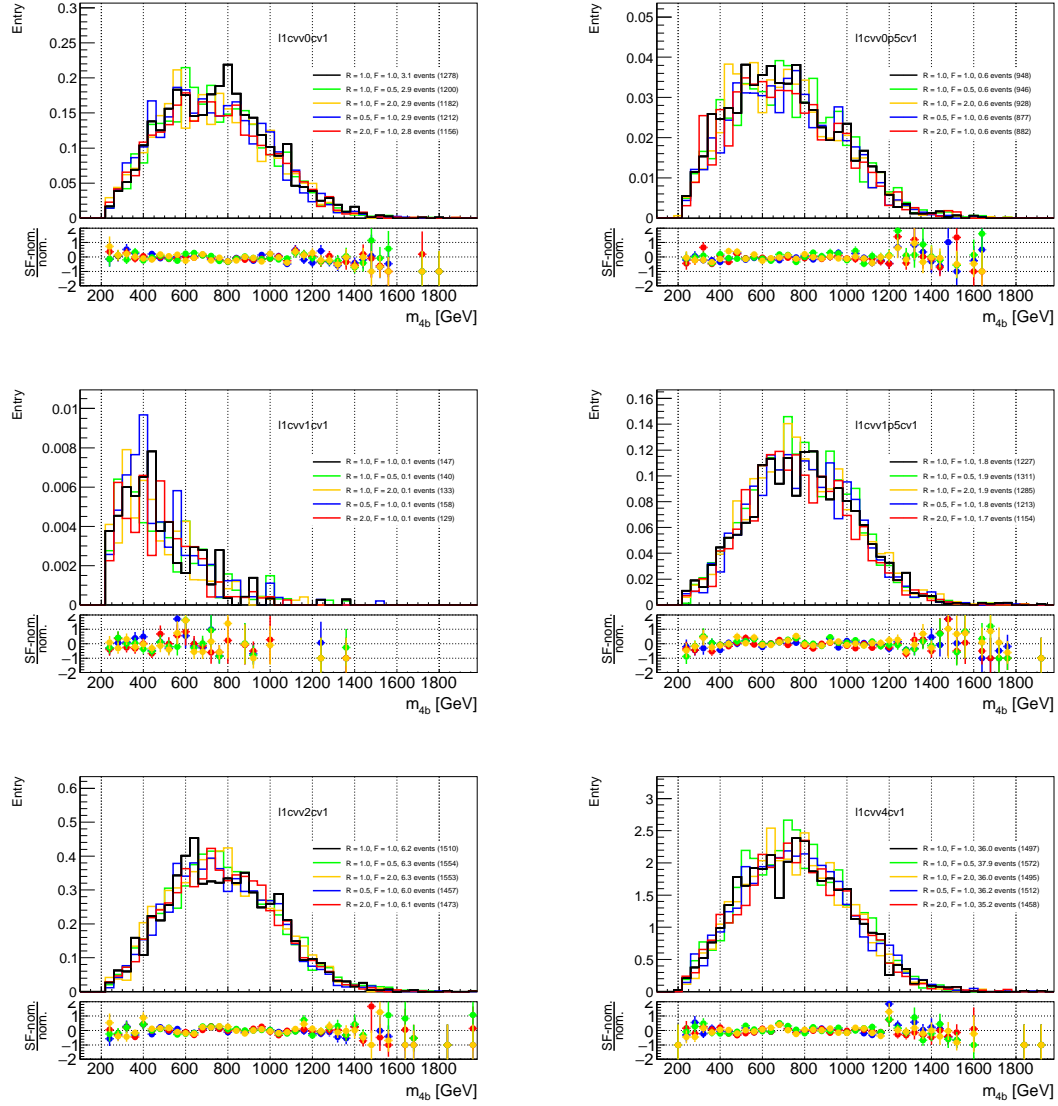


Figure 4.48: The m_{4b} distribution of truth samples of the non-resonant signals with the variation of the renormalization and factorization scale factor; $(\mu_R, \mu_F) = (1.0, 1.0), (1.0, 0.5), (1.0, 2.0), (0.5, 1.0), (2.0, 1.0)$. Each plot is the case of $\kappa_{2V} = 0.0, 0.5, 1.0, 1.5, 2.0, 4.0$.

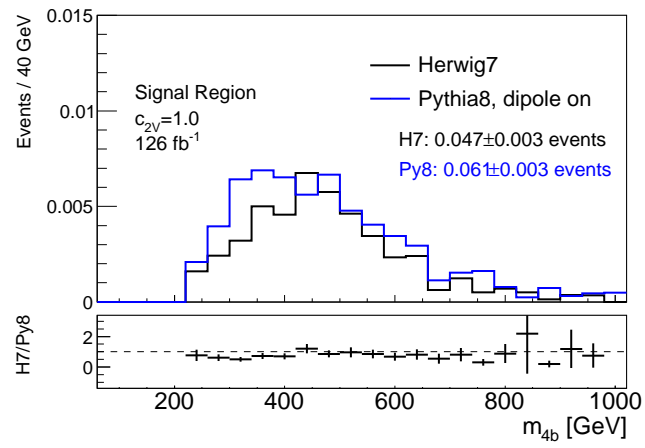


Figure 4.49: The m_{4b} distribution of truth samples of non-resonant signals with parton shower generator.

4.8.2 Systematic from backgrounds

Detector-based uncertainties

The backgrounds of all hadronic and non all hadronic $t\bar{t}$ are estimated using MC. Therefore, the estimation results have the uncertainties from the detector simulations. The m_{4b} distribution in the signal region with JES, JER, and b-tagging uncertainties for all hadronic and non all hadronic $t\bar{t}$ are shown in Figure 4.50 and Figure 4.51, respectively. The uncertainty from JES and JER is about 30%, which is comparable to the uncertainty of the normalization in CR for all hadronic $t\bar{t}$ and the theory uncertainty for non-all hadronic $t\bar{t}$. The impact of the b-tagging SFs is obtained to be much smaller than that of JES/JER uncertainties. The uncertainties from the JES and JER are shown in the figures in the section 4.10 as each name of the JES/JER nuisance parameters.

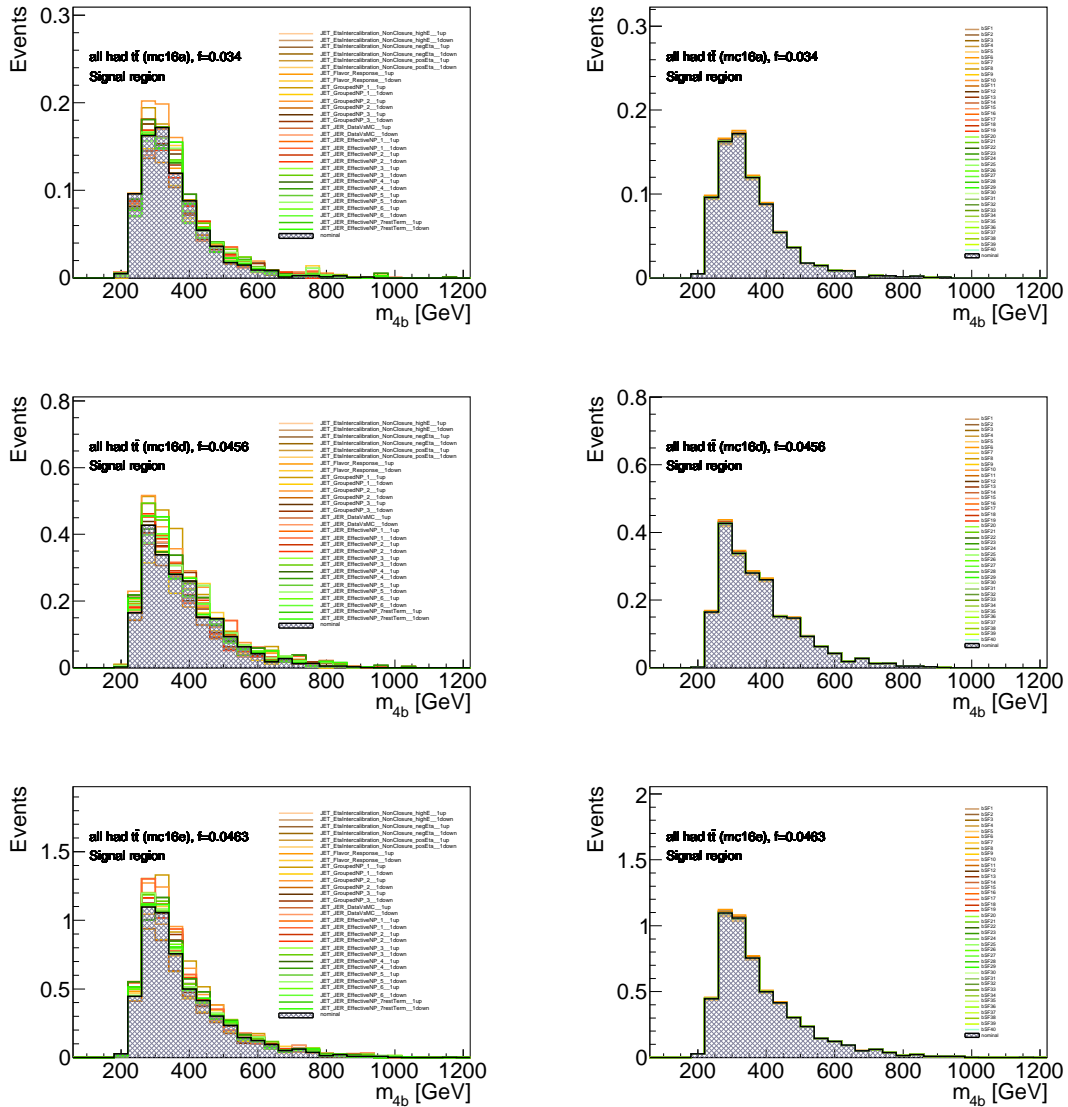


Figure 4.50: The distribution for 2016 (top), 2017 (medium), and 2018 (bottom) of all hadronic $t\bar{t}$ background with JES/JER uncertainties (left) and b-tagging SFs (right).

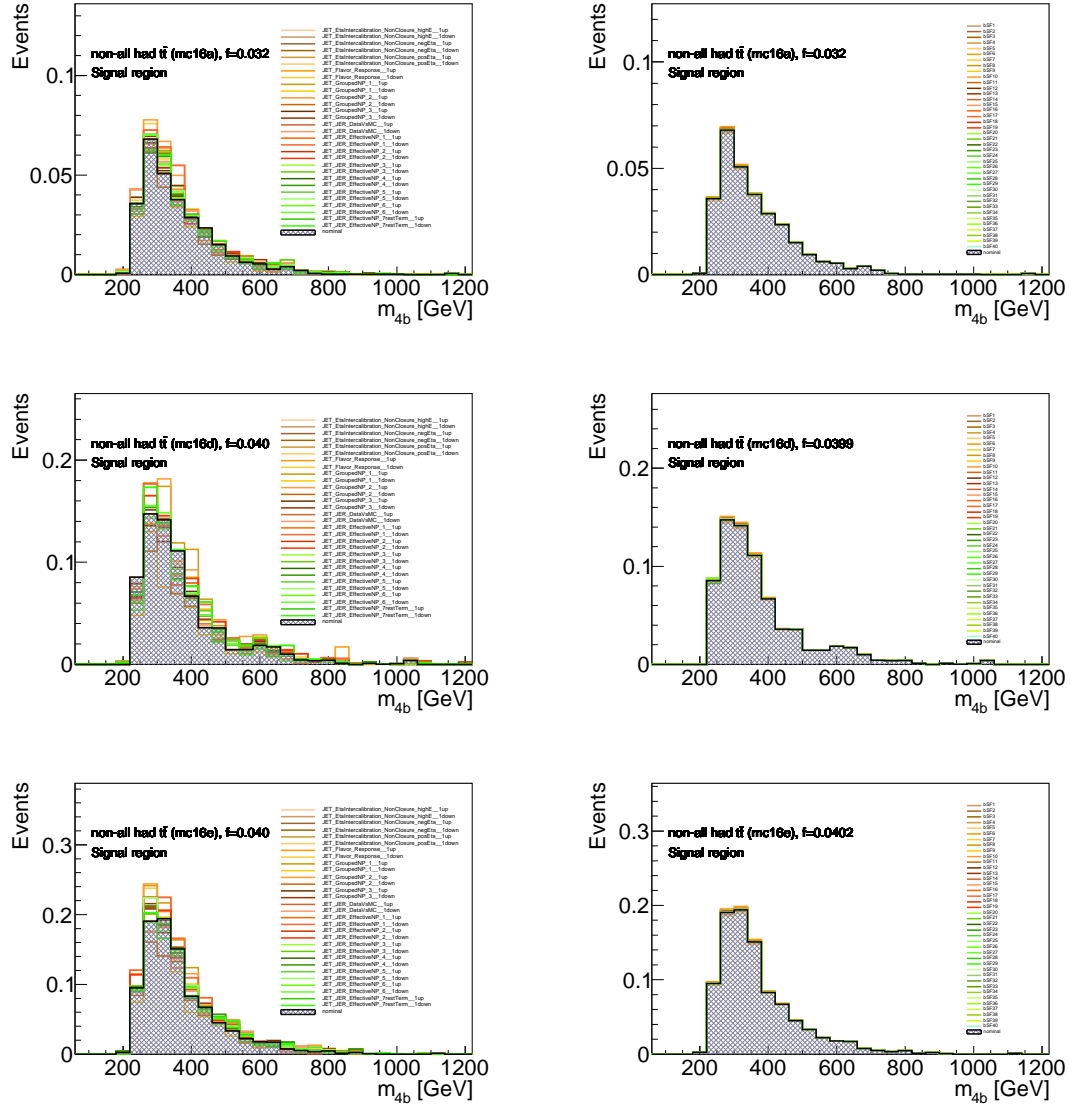


Figure 4.51: The distribution for 2016 (top), 2017 (medium), and 2018 (bottom) of non all hadronic $t\bar{t}$ background with JES/JER uncertainties (left) and b-tagging SFs (right).

Uncertainties from the modeling procedure of the QCD background

The yields and shape uncertainties are evaluated in VR. The m_{4b} distribution in VR is shown in Figure 4.52. To estimate the shape uncertainty, the straight line fit to the ratio of the data and background is executed. To avoid the situation that the shape uncertainty in the low mass region constraints that in the high mass region, the straight line fit is executed in two regions which are split at 400 GeV. The result of fit is shown as red line in the ratio plot in Figure 4.52. The fit results of the slope and the intercept are consistent with flat distribution. The green lines in Figure 4.52 is the fitted results with $+1\sigma$ and inverted slope of the one. When determining the uncertainty band, the normalization is kept fixed by varying the constant parameter of the fit. The m_{4b} distribution weighted with the two slopes while keeping the yields unchanged is taken into account for the systematic uncertainties. The shape uncertainties in the low mass region and high mass region are shown in the figures in the section 4.10 as QCD_Shape_lowmass and QCD_Shape_highmass, respectively.

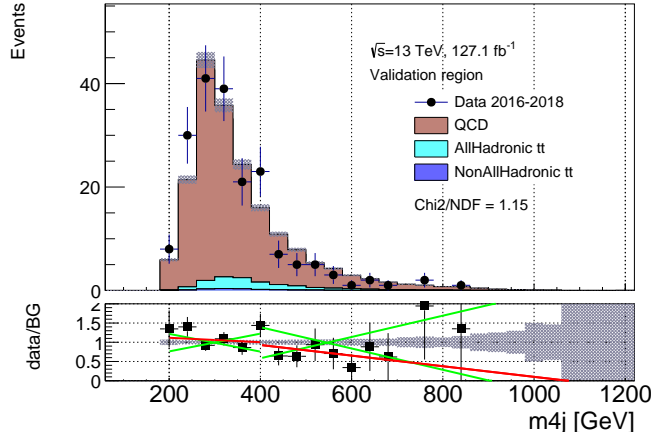


Figure 4.52: The m_{4b} distribution in VR. The fitted result is shown as red line in the ratio plot. The green lines in Figure 4.52 is the fitted results with $+1\sigma$ and inverted slope of the one.

The kinematic reweighting has some sensitivity to the region chosen to derive the reweighting. A systematic uncertainty for this choice is determined by deriving the full kinematic reweighting from the validation region, and comparing the result to the reweighting from the control region. The result on the signal region m_{4j} distribution is shown in Figure 4.53. The difference between the results is applied as an uncertainty (symmetrized). This uncertainty is shown in the figures in the section 4.10 as QCD_Shape_KRVR.

Uncertainty on QCD Background Normalization

One source of normalization uncertainty comes from the fit used to simultaneously normalize the all-hadronic $t\bar{t}$ and QCD. The uncertainties nominally are only the statistical uncertainty on the fit. However, as these two values are correlated, we first diagonalize the covariance matrix and create two independent normalization uncertainties that simultaneously vary the QCD and $t\bar{t}$ coherently to take into account the correlation correctly. These are labeled as NormCR uncertainties in the figures of section 4.10.

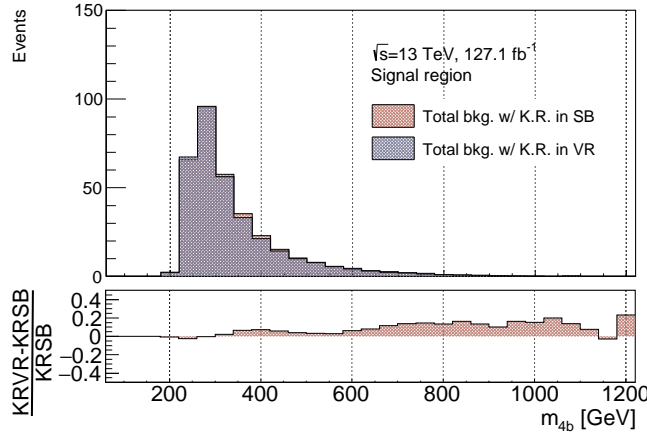


Figure 4.53: The m_{4b} distribution of the total background in SR. The red one is the result with kinematic reweighting in sideband region and the dark grey is the result with kinematic reweighting in validation region.

The validation region was used to determine a shape uncertainty, it is also used to determine a normalization uncertainty. As shown in Table 4.18 the data agrees with the multi-jet dominated (92%) background prediction, but the statistical uncertainty is 7.6%. This is taken as the systematic uncertainty on the QCD normalization. This uncertainty is shown in the figures in the section 4.10 as QCD_YieldVR. As the stats in the VR are lower than the CR, this uncertainty is somewhat larger than the NormCR.

Uncertainties from the modeling procedure of the $t\bar{t}$ background

The shape uncertainties of $t\bar{t}$ background is evaluated using $2b/4b$ ratio at preselection level (Just after 2 Higgs candidates and 2 VBF jets are selected.). The plots of the m_{4b} distribution of the $2b$ sample reweighted with the pseudo-tag rate f is compared to the $4b$ sample for the all had $t\bar{t}$ and non-all had $t\bar{t}$ are shown in Figure 4.54 (left and right). The result of fit is shown as red line in the ratio plot in Figure 4.52. The fit results of the slope and the intercept are consistent with flat distribution. The green lines in Figure 4.52 is the results of fit with $+1\sigma$ and inverted slope with $+1\sigma$. The m_{4b} distribution weighted with the two slopes while keeping the yields unchanged is taken as the systematic uncertainties. These two uncertainties for all hadronic and non all hadronic $t\bar{t}$ background are shown in the figures in the section 4.10 as (non)allhad_Shape.

Theoretical uncertainties of the $t\bar{t}$ MC

We use the sample of Powheg+Pythia8 as nominal sample to estimate $t\bar{t}$ background. To see the systematics from the difference of the PDF and parton shower generators, the difference among the samples of Powheg+Pythia8, Powheg+Herwig7, and aMcAtNlo+Pythia8 is investigated. Figure 4.55 shows the m_{4b} distribution of the all hadronic $t\bar{t}$ and non all hadronic $t\bar{t}$. The ratio plots of the nominal sample (Powheg+Pythia8) and the systematic samples (Powheg+Herwig7 and aMcAtNlo+Pythia8) are included as systematics

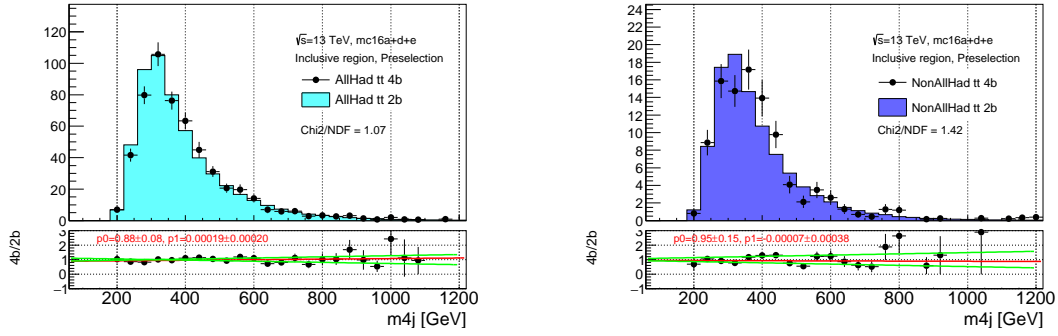


Figure 4.54: The 2b/4b comparison of the all hadronic $t\bar{t}$ and non-all hadronic $t\bar{t}$ at the preselection level. The fitted result is shown as red line in the ratio plot. The green lines in the figure is the fitted results with $+1\sigma$ and inverted slope of the one with $+1\sigma$.

in the final fit. These two uncertainties are shown in the figures in the section 4.10 as (non)allhad_PhH7 and (non)allhad_aMcAtNloPy8, respectively.

Uncertainties of ggF non resonant background

The non resonant hh production via ggF is treated as a background which is estimated using MC. Therefore, the theoretical uncertainty for the ggF non resonant background is investigated using truth samples with renormalization scale factor and factorization scale factor of 0.5/2.0. The m_{4b} distributions with the variation of the factors are shown in Figure 4.56. The bin-by-bin non-closure derived from the ratio plots of nominal and systematics samples is included as systematics in the final fit.

The m_{4b} distributions in the signal region with JES and JER uncertainties for non-resonant background are shown in Figure 4.57.

The m_{4b} distributions in the signal region with trigger SFs for ggF non resonant background are shown in Figure 4.57.

4.9 Statistical analysis

The statistical techniques used in this search are the same as adopted in [32] and summarized below for completeness. In all cases, the likelihood is defined as the usual Poisson likelihood over the m_{4b} distribution. Uncertainties are implemented as nuisance parameters (θ).

4.9.1 Search procedure

The statistical analysis of the data after unblinding consists first in a search for statistically significant deviation from the background model hypothesis. The test statistic used is a one sided profile likelihood ratio:

$$\tilde{q}_\mu \begin{cases} -2\ln \frac{L(0, \hat{\hat{\theta}}(0))}{L(\hat{\mu}, \hat{\theta})} & (\hat{\mu} > 0) \\ 0 & (\hat{\mu} < 0) \end{cases} \quad (4.19)$$

Where, μ is the value of the signal normalization considered, $\hat{\mu}$ is the maximum likelihood (ML) value of μ . θ are the set of nuisance parameters (NP), $\hat{\theta}$ is the ML value of θ and $\hat{\hat{\theta}}$ is the ML value of θ when μ is fixed at a particular value. L denotes the profile likelihood, $L(\hat{\mu}, \hat{\theta})$ is the likelihood where μ is allowed to take any value, the unconstrained likelihood. $L(0, \hat{\hat{\theta}})$ is the likelihood for the value of $\mu = 0$, the constrained likelihood.

This tests the compatibility of the data with the background-only hypothesis, $\mu = 0$. The local p-value of a set of data, p_0 , is defined as the probability for the background-only hypothesis to have a value of q_0 that is as high or higher than the value of q_0 in that data. In order to obtain p_0 , pseudo-experiments are generated with the background only model and the distribution of the test statistic, q_0 , is built up from the values of the pseudo-experiments.

If a local p_0 value is obtained that corresponds to a significance of greater than 3σ then a correction for the look elsewhere effect will be computed in order to obtain the global p-value. This correction is obtained using the distribution of the test statistic, q_0 , in background only pseudo-experiments. The average number of upwards crossings, $< N_{1\sigma} >$, across the mass range tested of q_0 at the value of q_0 corresponding to 1σ significance, $q_0^{1\sigma}$, is estimated using the average number from the background only pseudo-experiments and is used to obtain the correction to the local p-value using the equation:

$$p_0^{\text{global}} = p_0^{\text{local}} + N_{1\sigma} > e^{-(q_0^{\text{max}} - q_0^{1\sigma})/2} \quad (4.20)$$

Where p_0^{local} is the lowest p_0 value across the mass range tested, corresponding to a test statistic value of q_0^{max} .

4.9.2 Limit setting procedure

To evaluate an upper limit of σ ($pp \rightarrow Hjj \rightarrow hhjj \rightarrow b\bar{b}b\bar{b}jj$) or σ ($pp \rightarrow hhjj \rightarrow b\bar{b}b\bar{b}jj$) a frequentist method is used where a cross section is excluded on the basis of the statistic CL_s which is defined as the ratio of CL_{s+b} to CL_b . Where CL_{s+b} is defined as $P_{s+b}(q \leq q_{\text{obs}})$, i.e. the probability of the signal+background model to produce data with a value of q less than that observed. Where q is a test statistic, which tests the compatibility with the signal+background hypothesis, where low values indicate a high level of compatibility. $CL_b = P_b(q \leq q_{\text{obs}})$, i.e. the probability of the background model to produce data with the same or more compatibility with the signal+background model as that observed. Cross sections are excluded if they have a value of $CL_s \leq 0.05$.

In order to calculate the p-values used to determine CL_{s+b} and CL_b the test statistic chosen is a one-sided profile likelihood ratio defined as:

$$\tilde{q}_\mu \begin{cases} -2\ln \frac{L(\mu, \hat{\hat{\theta}}(\mu))}{L(0, \hat{\hat{\theta}}(0))} & (\hat{\mu} < 0) \\ -2\ln \frac{L(\mu, \hat{\hat{\theta}}(\mu))}{L(\hat{\mu}, \hat{\theta})} & (0 \leq \hat{\mu} < \mu) \\ 0 & (\hat{\mu} > \mu) \end{cases} \quad (4.21)$$

Where, μ is the value of the signal normalization considered, $\hat{\mu}$ is the maximum likelihood (ML) value of μ . θ are the set of nuisance parameters, $\hat{\theta}$ is the ML value of θ and $\hat{\hat{\theta}}$ is the ML value of θ when μ is fixed at a particular value. L denotes the profile likelihood, $L(\hat{\mu}, \hat{\theta})$ is the likelihood where μ is allowed to take any value, the unconstrained likelihood. $L(\mu, \hat{\hat{\theta}})$ is the likelihood for a particular fixed value of μ , the constrained likelihood.

The definition of the test statistic, \tilde{q}_μ , takes into account the fact that when searching for a resonance on top of a background the case where $\mu < 0$ is unphysical.

In order to obtain the distributions of the test statistic, \tilde{q}_μ , the asymptotic approximation is used in this analysis. The equations obtained in [33] are solved numerically. These equations can be derived using approximations of the distribution of $\hat{\mu}$ as Gaussian and the asymptotic approximation of the distribution of the profile likelihood ratio to a non-central chi-squared distribution.

4.10 Results

4.10.1 The unblinded SR

The m_{4b} distribution in unblinded SR is shown in Figure 4.59 of the post-fit result with zero signal hypothesis. No significant excess has been observed. The significance of the excess over the background-only prediction is quantified using the local p_0 -value, defined as the probability of the background-only model to produce a signal-like fluctuation at least as large as that observed in the data. The most extreme p_0 -value corresponds to a local significance of 1.5 standard deviations at $m_H = 550$ GeV with narrow width (4 MeV), which the post-fit result is shown in Figure 4.60.

4.10.2 Observed limits

The expected and observed 95% CL upper limits for the cross-section of resonant signals at 126.0 fb^{-1} are shown in Figure 4.61. The observed excluded region corresponding to $m_H > 666.9$ GeV, while the expected to $m_H > 497.0$ GeV for the benchmark point of $\tan\beta = 2.0$ and $\sin(\beta - \alpha) = 0.6$ in the Type-II 2HDM.

The expected and observed limit on the non resonant signal at SM hypothesis has been set as shown in Table 4.19. Limits are also calculated as a function of κ_{2V} as presented in Figure 4.62. To derive the limits at any κ_{2V} values, the theory line and the samples at any κ_{2V} are obtained by the reweighting method with the scale factors using the cross-section and the samples at $\kappa_{2V} = 0.0, 1.0, 2.0$:

$$|A(\kappa_V, \kappa_{2V}, \lambda)|^2 \sim \left(1 - \frac{3}{2}\kappa_{2V} + \frac{1}{2}\kappa_{2V}^2\right) |A(1, 0, 1)|^2 + (\kappa_{2V} - \kappa_{2V}^2) |A(1, 1, 1)|^2 + \frac{1}{2}(\kappa_{2V}^2 - \kappa_V) |A(1, 2, 1)|^2, \quad (4.22)$$

when we write the amplitude of the non-resonant signal as $A(\kappa_V, \kappa_{2V}, \lambda) = \kappa_V^2 \tilde{a} + \kappa_{2V} \tilde{b} + \kappa_V \lambda \tilde{c}$ ($\tilde{a}, \tilde{b}, \tilde{c}$: amplitude of the each diagram in Figure 2.5). The observed excluded region corresponds to $\kappa_{2V} < -0.56$ and $\kappa_{2V} > 2.89$, while the expected to $\kappa_{2V} < -0.67$ and $\kappa_{2V} > 3.10$.

Table 4.19: 95% C.L exclusion limits for SM non-resonant hh production in units of the SM prediction for $\sigma(pp \rightarrow hh \rightarrow bbbb)$ at 126.0 fb^{-1} .

-2σ	-1σ	expected	1σ	2σ	observed
290	390	540	750	1000	840

Figure 4.63 and 4.66 shows the ranking of the nuisance parameters in the fit. The largest difference between pre- and post-fit values is in the shape uncertainty from the $2b/4b$ modeling,

and the normalization in the CRs. The detector related uncertainties are shown to be very small. Figure 4.64 shows the correlation matrices for the three years analyzed separately. Some correlations between various background uncertainties are observed. Finally, Figure 4.65 and Figure 4.68 shows the pull plot. The pulls are observed to be consistent with zero within 1σ in this unblinded fit, though a small profiling is shown for the QCD modeling uncertainties.

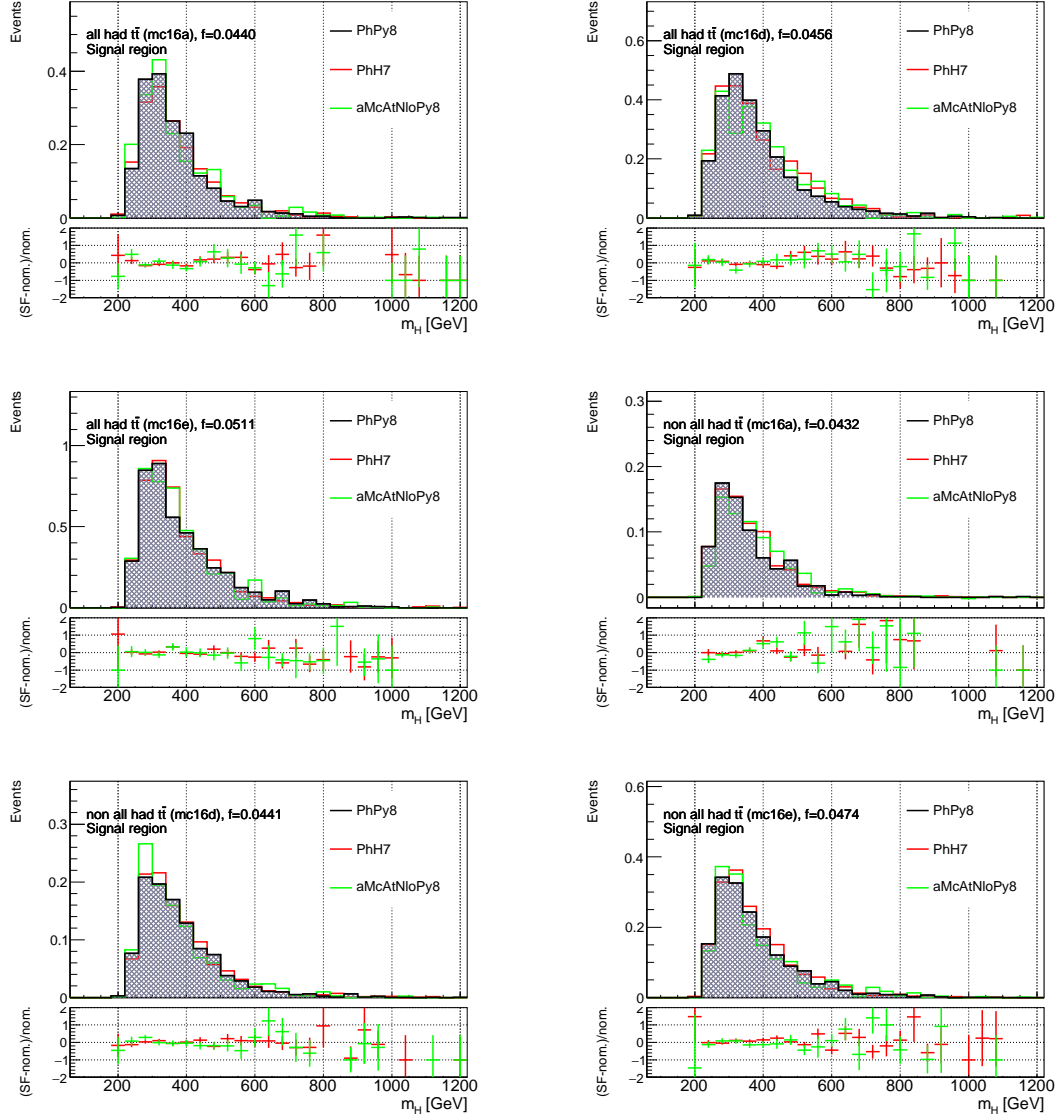


Figure 4.55: The distribution for the 2016 (top), 2017 (medium), and 2018 (bottom) of $t\bar{t}$ backgrounds with the variation of the generator and, shower and hadronization.

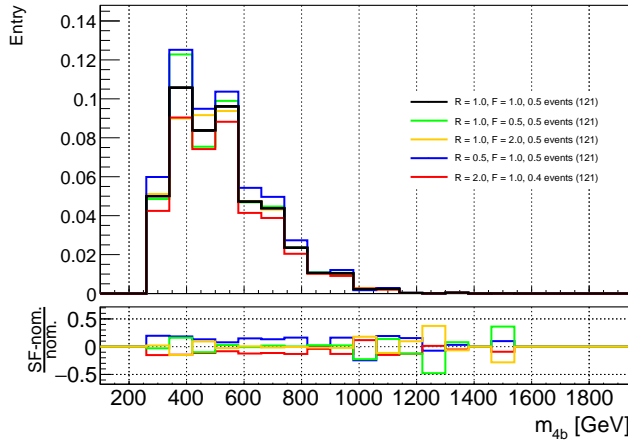


Figure 4.56: The m_{4b} distribution of truth samples of ggF non-resonant background.

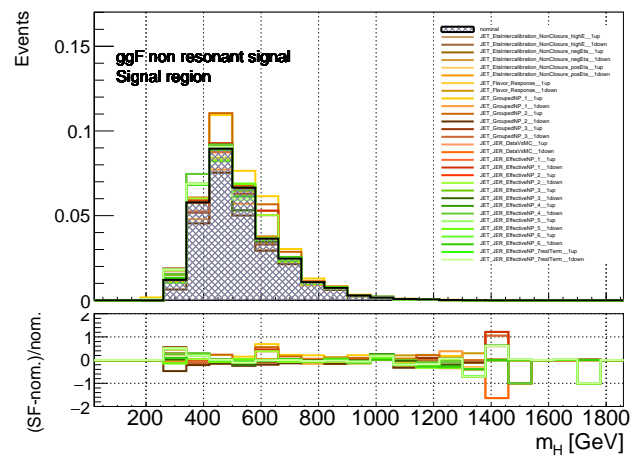


Figure 4.57: The m_{4b} distribution of the non-resonant signal with JES and JER uncertainties.

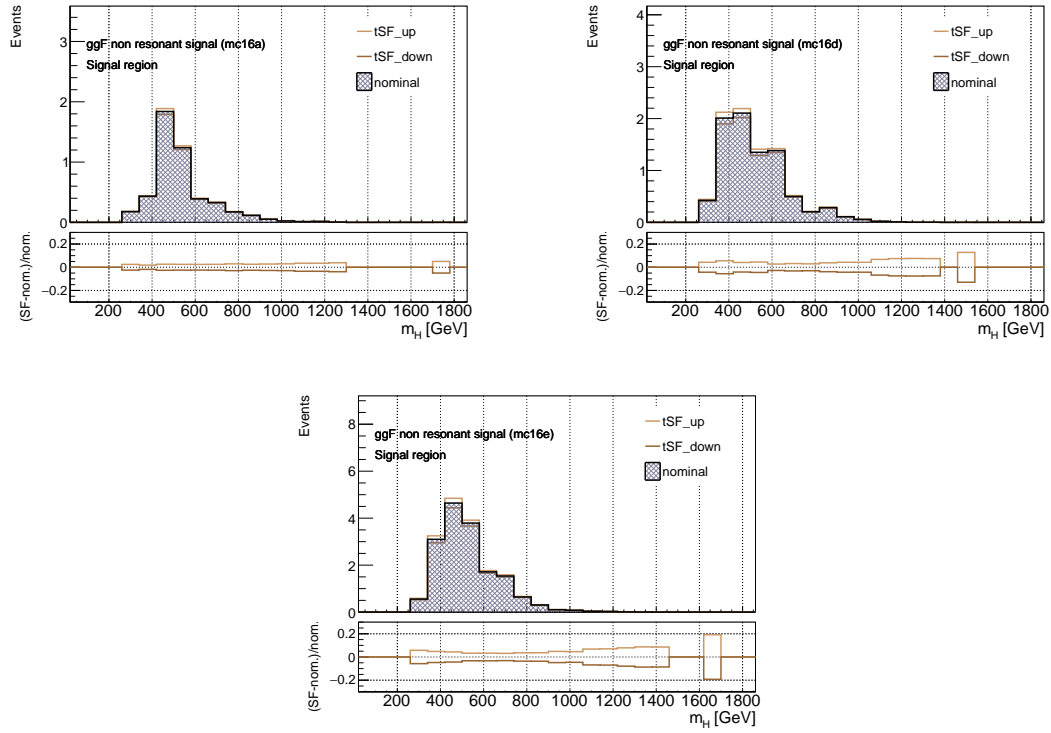
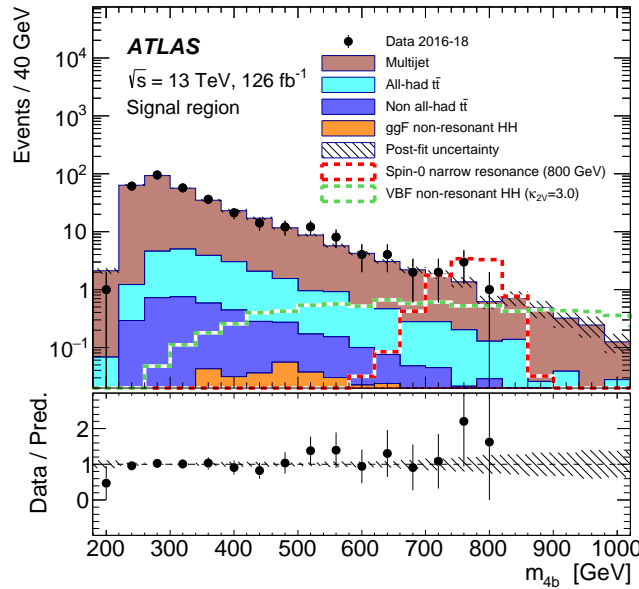
Figure 4.58: The m_{4b} distribution of the non-resonant signal with jet-level trigger SFs.

Figure 4.59: Post-fit mass distribution of the hh candidates in the signal region. The expected background is shown after the profile-likelihood fit to data with the background-only hypothesis, and the narrow-width resonant signal at 800 GeV and the non-resonant signal at $\kappa_{2V} = 3.0$ is overlaid, normalized to the observed upper limit on the cross-section. The lower panel shows the ratio of the observed data to the estimated SM background.

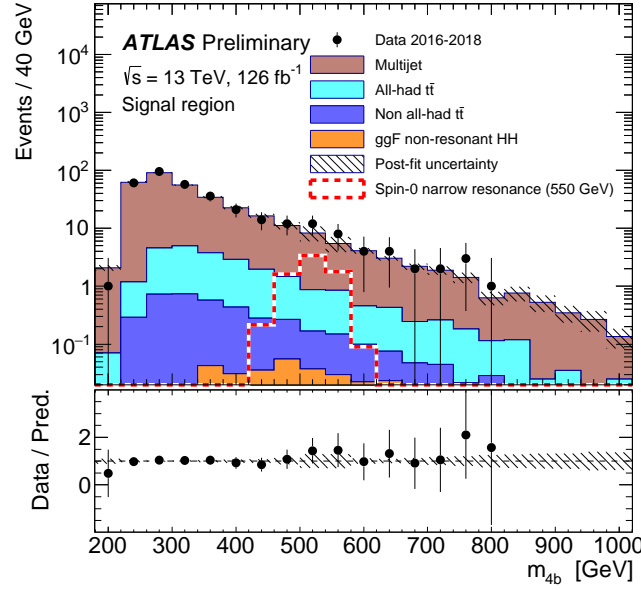


Figure 4.60: Post-fit mass distribution of the hh candidates in the signal region. The expected background is shown after the profile-likelihood fit to data with the background+signal hypothesis, where the signal is the narrow-width resonant signal at 500 GeV.

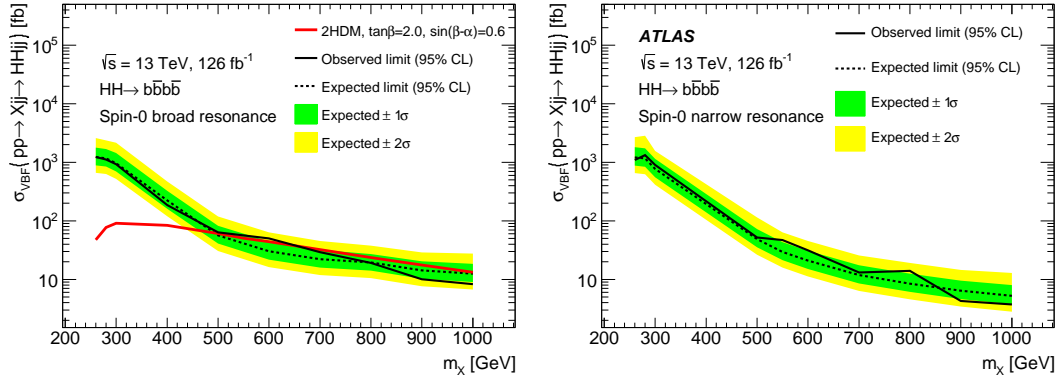


Figure 4.61: Observed and expected limits for the resonant signals at 126.0 fb^{-1} with all demonstrated systematic uncertainties. The left is the broad resonance hypothesis of the benchmark point of $\tan \beta = 2.0$ and $\sin(\beta - \alpha) = 0.6$ in Type-II 2HDM, and the right is the narrow resonance hypothesis.

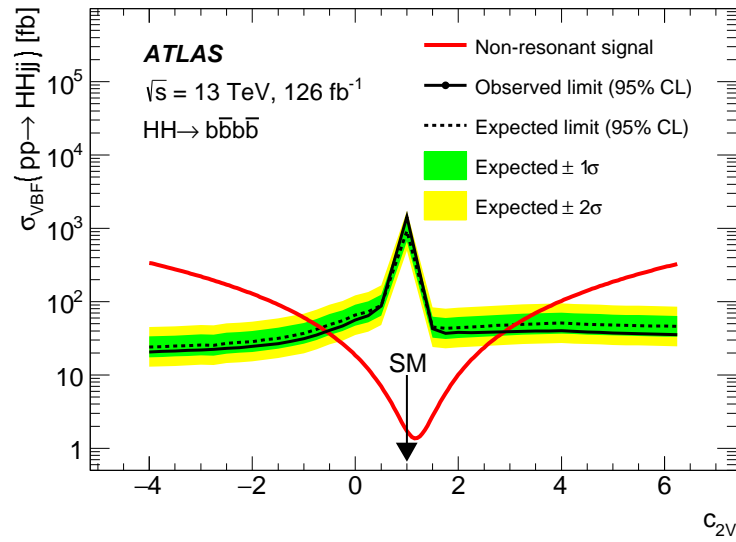


Figure 4.62: Observed and expected limits for the non-resonant signals at 126.0 fb^{-1} with all demonstrated systematic uncertainties.

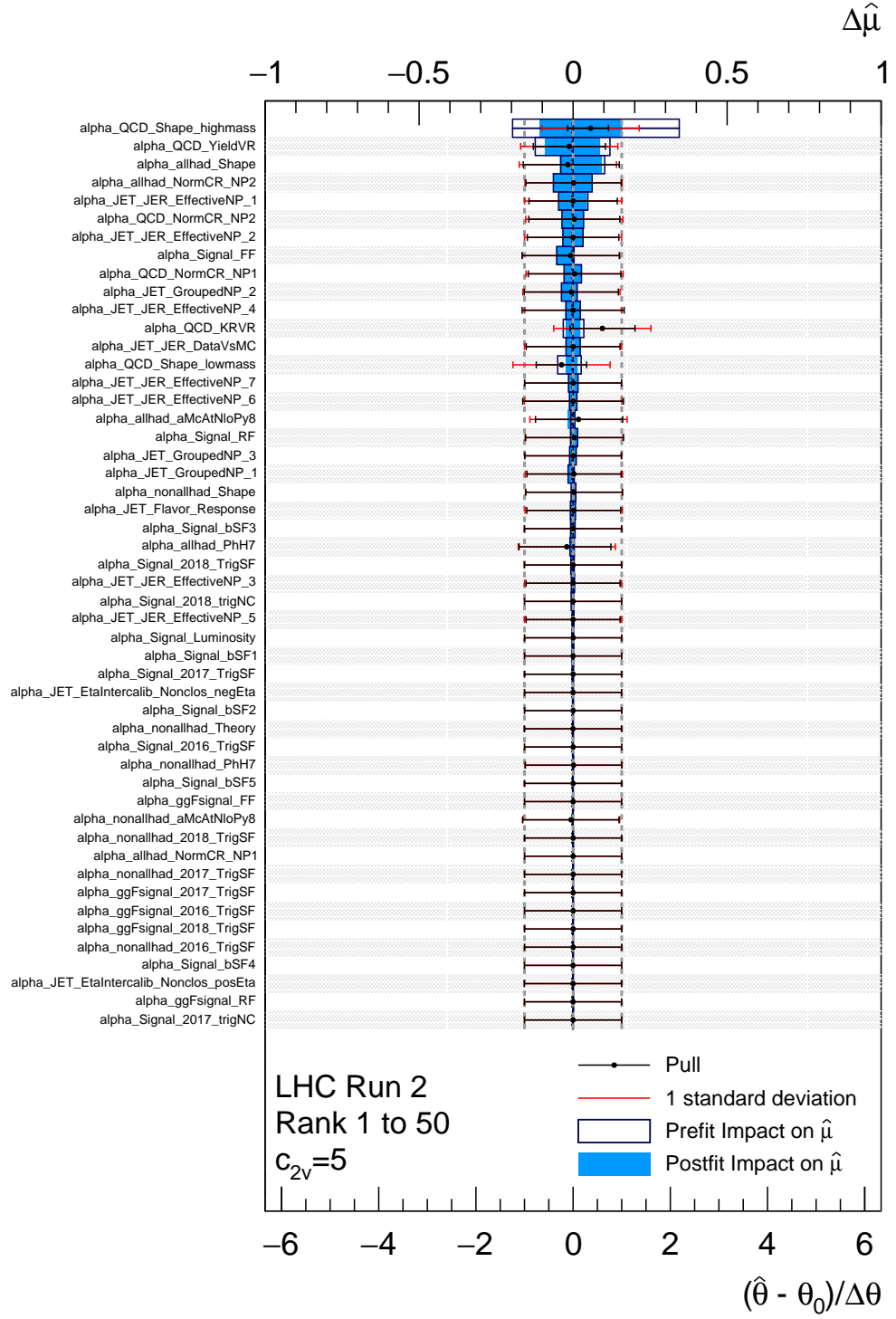


Figure 4.63: The figure in the right hand side shows the ranking plot of the systematics for the observed limit. This is for the 500 GeV mass point.

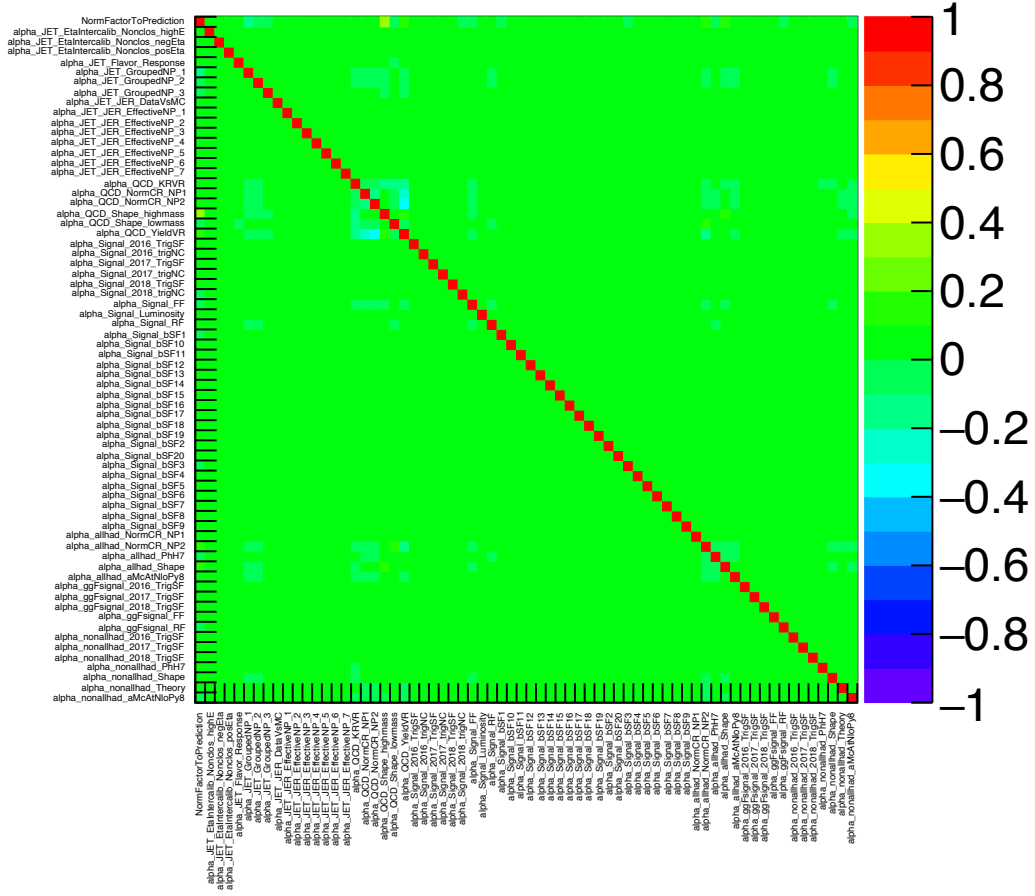


Figure 4.64: The correlation matrix of all nuisance parameters for the fit of the observed one, for the 500 GeV mass point. No significant correlation is observed.

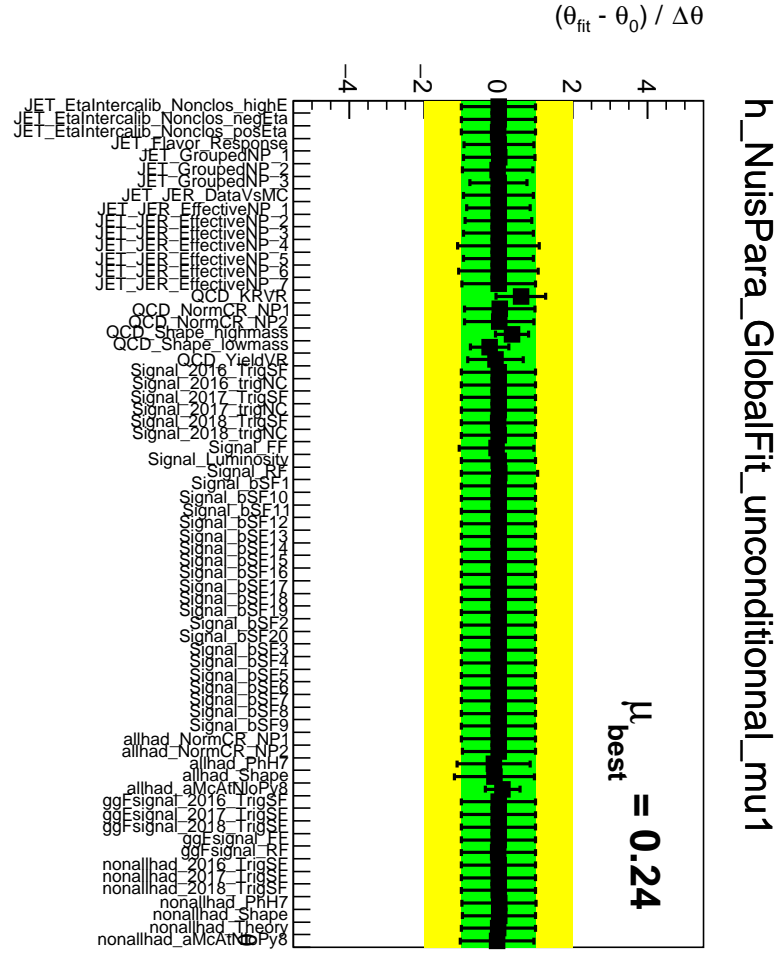


Figure 4.65: The pulls for the fit of the observed one. The largest profiling is from the uncertainty of the shape uncertainty that comes from the 2b/4b modeling and the normalization in CRs, as shown in Figure 4.63. This is for the 500 GeV mass point.

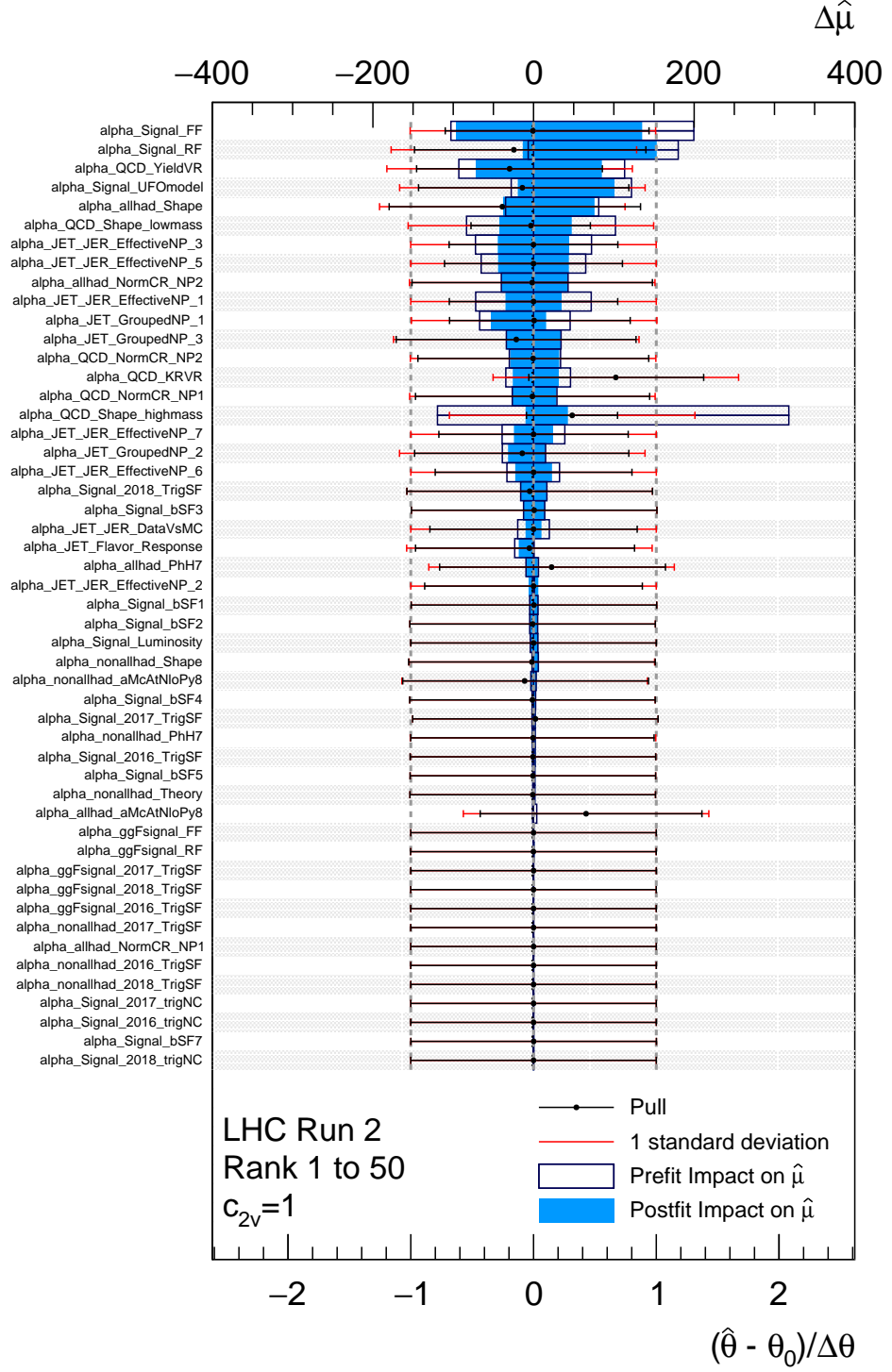


Figure 4.66: The ranking plot of the systematics for the observed limit of the non resonant signal. This is for the point of $\kappa_{2V} = 1$.

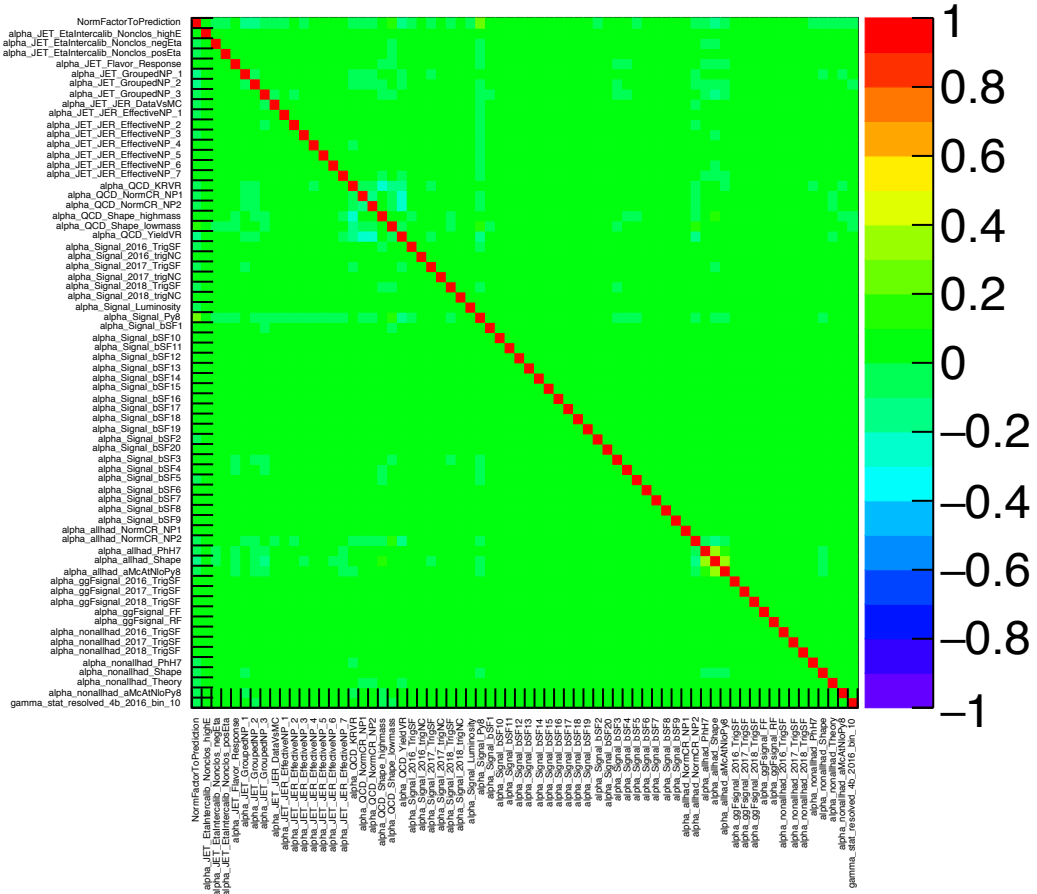


Figure 4.67: The correlation matrix of all nuisance parameters for the fit of the observed one, for the point of $\kappa_{2V} = 1$. No significant correlation is observed.

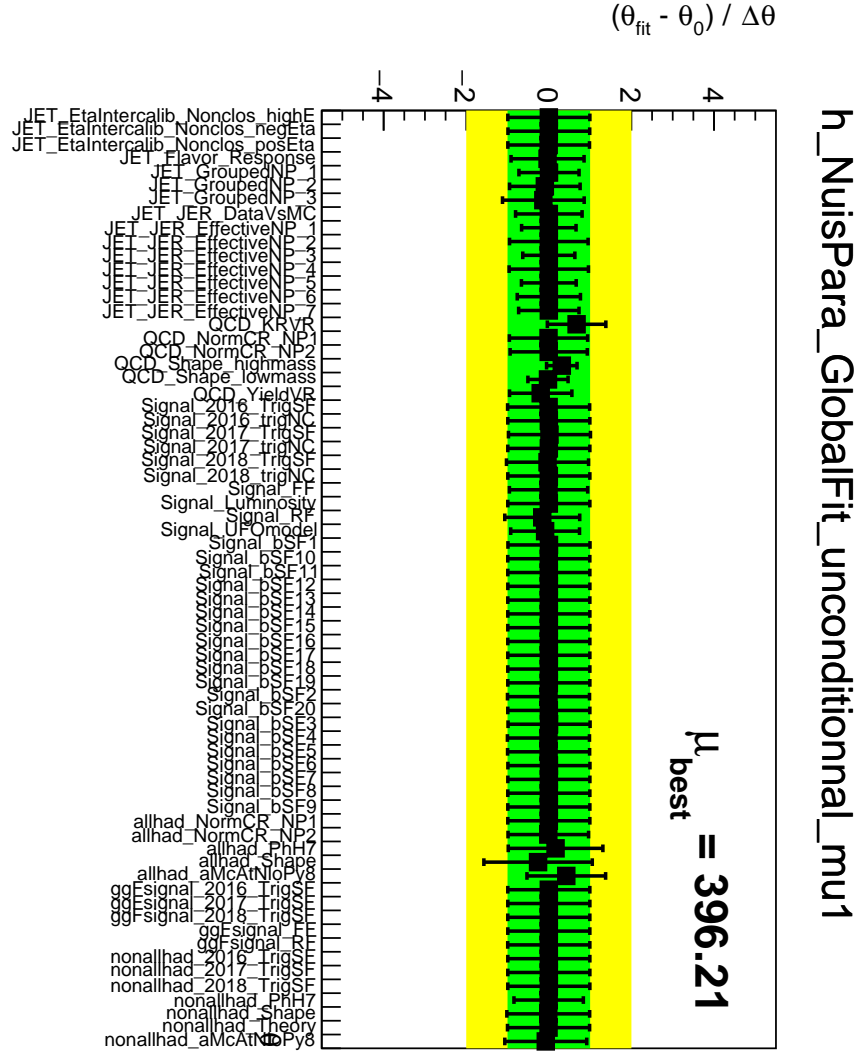


Figure 4.68: The pulls for the fit of the observed one. The largest profiling is from the uncertainty of the shape uncertainty that comes from the 2b/4b modeling and the normalization in CRs, as shown in Figure 4.63. This is for the point of $\kappa_{2V} = 1$.

Chapter 5

Discussion

5.1 Interpretation on the Type-II 2HDM

As described in the Section 4.10, the interpretation on the Type-II 2HDM with the parameter of $\tan\beta = 2.0$ and $\sin(\beta - \alpha) = 0.6$ has been performed as a benchmark point. In this section, we will discuss how the constraint on the parameter space are given in the Type-II 2HDM.

The production cross-section and the decay width of the heavy Higgs boson depend on the angles, α and β . The parameter regions where the cross-section is larger and the decay width is smaller than that of $\tan\beta = 2.0$ and $\sin(\beta - \alpha) = 0.6$ are expected to be excluded with the results of this analysis. Figure 5.1 shows the regions where the cross-section is larger and the decay width is smaller than that of $\tan\beta = 2.0$ and $\sin(\beta - \alpha) = 0.6$ in red, the regions where the cross-section is larger and the decay width is larger than that of $\tan\beta = 2.0$ and $\sin(\beta - \alpha) = 0.6$ in blue, and the regions where the cross-section is smaller and the decay width is smaller than that of $\tan\beta = 2.0$ and $\sin(\beta - \alpha) = 0.6$ in green. Comparing Figure 5.1 with Figure 2.9, the region of $3 \lesssim \tan\beta \lesssim 8$, $0.8 \lesssim (\beta - \alpha) \lesssim 1.1$, and $m_H \lesssim 600$ GeV, where the direct search using the ggF process cannot exclude, can be excluded.

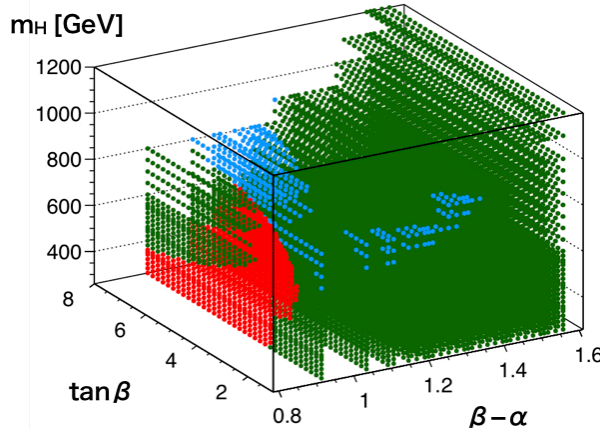


Figure 5.1: Red: the regions where the cross-section is larger and the decay width is smaller than that of $\tan\beta = 2.0$ and $\sin(\beta - \alpha) = 0.6$. Blue: the regions where the cross-section is larger and the decay width is larger than that of $\tan\beta = 2.0$ and $\sin(\beta - \alpha) = 0.6$. Green: the regions where the cross-section is smaller and the decay width is smaller than that of $\tan\beta = 2.0$ and $\sin(\beta - \alpha) = 0.6$.

On the other hand, the measurement of the signal strength of the SM Higgs boson can give

the constraint in the 2D region of $\tan\beta$ and $\cos(\beta - \alpha)$. Figure 5.2 shows the regions of the $(\cos(\beta - \alpha), \tan\beta)$ plane that are excluded at a confidence level of 95% or higher, for Type-II 2HDM. The data are consistent with the alignment limit at $\cos(\beta - \alpha) = 0$, in which the couplings of h match those of the SM Higgs boson, within one standard deviation or better in each of the tested models. The allowed regions also include narrow, curved petal regions at positive $\cos(\beta - \alpha)$ and moderate $\tan\beta$. These correspond to regions with $\cos(\beta + \alpha) \sim 0$, for which some fermion couplings have the same magnitude as in the SM, but the opposite sign. Figure 5.3 shows the cross section times the branching ratio of the VBF $hh \rightarrow b\bar{b}b\bar{b}$ process with the parameter of $\cos(\beta - \alpha)$ in Type-II 2HDM. The model point of $\tan\beta = 6.0$ and $\cos(\beta - \alpha) = 0.3$ where is in the curved petal region in Figure 5.2 has much less cross-section than that of the benchmark point of $\tan\beta = 2.0$ and $\cos(\beta - \alpha) = 0.8$. Unfortunately, the direct search of the Higgs pair production cannot be complementary analysis for the Type-II 2HDM.

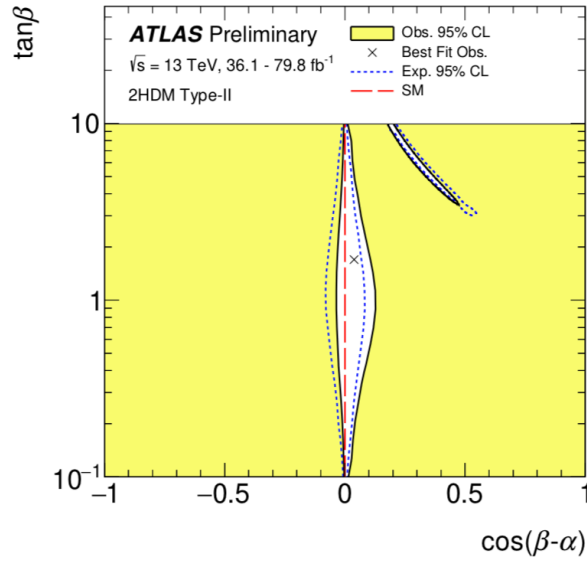


Figure 5.2: Regions of the $(\cos(\beta - \alpha), \tan\beta)$ plane of four types of 2HDMs excluded by fits to the measured rates of Higgs boson production and decays [9]. Contours at 95% CL, defined in the asymptotic approximation by $-2\log \Lambda = 5.99$, are drawn for both the data and the expectation for the SM Higgs sector. The cross in the plot marks the observed best-fit value.

5.2 Possibility of the other channels

In the previous ggF searches, the channels of $hh \rightarrow b\bar{b}b\bar{b}$, $b\bar{b}\tau\bar{\tau}$, $b\bar{b}\gamma\gamma$, etc. are used. Remembering Figure 2.7, the combination of them is effective for the limit section on the cross-section and the self-coupling strength κ_λ . The leading channels of $b\bar{b}\tau\bar{\tau}$ and $b\bar{b}\gamma\gamma$ have clean events that means low background because the final state consists leptons, while the $b\bar{b}b\bar{b}$ channel has full hadronic final state that mean high background from the QCD multi-jet events. The requirement of the additional two jets in forward region in the VBF $hh \rightarrow b\bar{b}b\bar{b}$ analysis makes the background $\sim 1/30$ and the ratio of the signal and the background $\sim 1/20$ for the all mass, m_{4b} , of the VBF resonant signal as shown in Figure 5.4. Therefore, the channels of $b\bar{b}\tau\bar{\tau}$, $b\bar{b}\gamma\gamma$ are expected to have low background for the VBF signals in all m_{4b} as well. Although it depends on the study on the each channels, we can expect the limit on the cross section of the resonant and non-resonant signals improved by a few factors if we can get similar sensitivity in each channels.

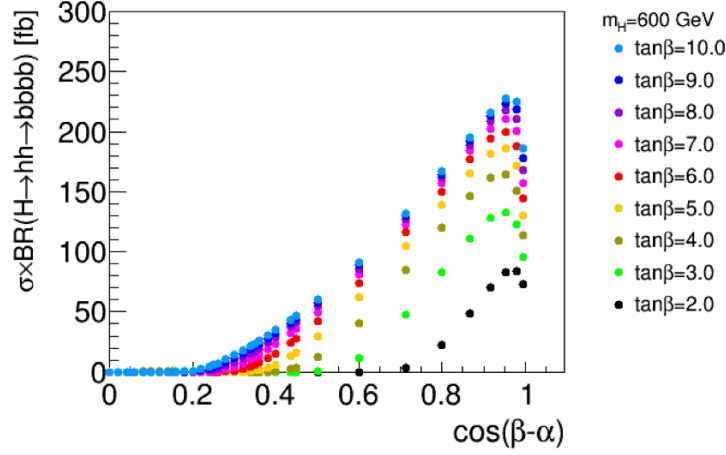


Figure 5.3: The cross section of the VBF $hh \rightarrow b\bar{b}b\bar{b}$ with the parameter of $\cos(\beta - \alpha)$ in the Type-II 2HDM, which are calculated using SusHi-1.5.0 [7] and 2HDMC-1.7.0 [8], respectively. The mass of the heavy Higgs boson is 600 GeV. The $\cos(\beta - \alpha)$ and $\tan\beta$ are scanned in 0–1 and 2–10, respectively.

5.3 Prospects for the High Luminosity LHC

The LHC experiment plans to get the data of about 3000 fb^{-1} in 10 years from 2026 with the instantaneous luminosity of $7.5 \times 10^{34} \text{ cm}^{-2}\text{s}^{-1}$. By increasing the statistics, not only the statistic uncertainty is reduced, but also the systematic uncertainties from the normalization of the background in CRs and the evaluation of yields and shape of the QCD multi-jet background in VR are reduced. Figure 5.5 shows the expected limit on the resonant signals with the extrapolated statistics. The expected excluded region corresponding to $m_H > 375.3 \text{ GeV}$ for the parameters of $\tan\beta = 2.0$ and $\sin(\beta - \alpha) = 0.6$ in the Type-II 2HDM. Figure 5.6 shows the expected limit on the non-resonant signals with the extrapolated statistics. The expected excluded region corresponds to $\kappa_{2V} < 0.29$ and $\kappa_{2V} > 1.77$.

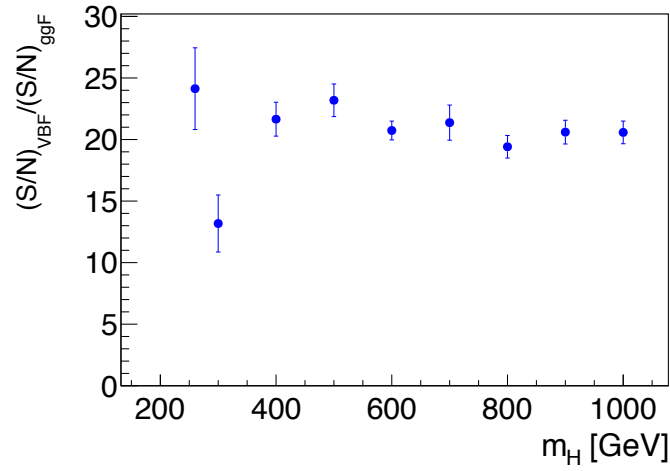


Figure 5.4: The ratio of the ratio of the signal and background in SR with selection of ggF and VBF analysis. The signal MC of VBF resonant signal with narrow is used for the both of the two selections. The mass window that maximize the sensitivity the count-based significance of the signal is set in the m_{4b} .

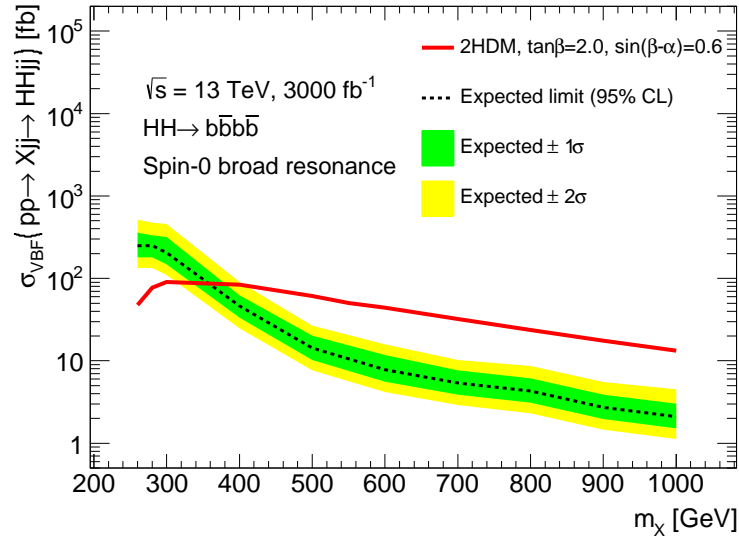


Figure 5.5: Expected limits for the resonant signals with the parameters $\tan\beta = 2.0, \sin(\beta - \alpha) = 0.6$ in Type-II 2HDM at 3000 fb^{-1} with all demonstrated systematic uncertainties.

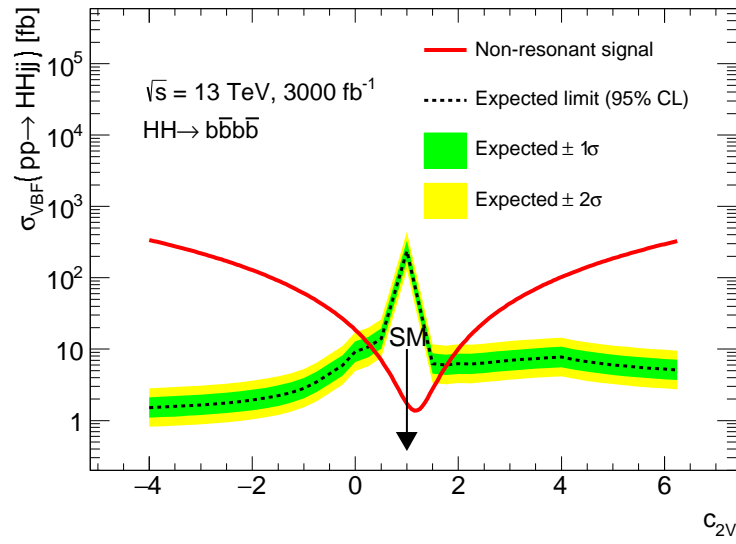


Figure 5.6: Expected limits for the non-resonant signals with κ_{2V} at 3000 fb^{-1} with all demonstrated systematic uncertainties.

Chapter 6

Conclusion

A search for the pair production of Higgs bosons is performed using $b\bar{b}b\bar{b}$ final state in Vector Boson Fusion at the pp collisions of full Run2 dataset with $\sqrt{s} = 13$ TeV. This is the first search in the LHC experiment. The unique features of this analysis are as below:

- VBF hh production is completely new signature for the heavy resonant search comparing with the ggF production mode that is studied in the conventional analyses.
- This analysis is sensitive for heavy Higgs predicted by two Higgs doublet model (2HDM) and can access different parameter space comparing to ggF $hh \rightarrow 4b$ analysis.
- This analysis can uniquely access the strength of the quadruple coupling of vector boson and Higgs bosons ($VVhh$ coupling) that has not been measured so far.

I have developed this new analysis from scratch:

- The triggers are selected according to the signal efficiency.
- The correction on the b-jet energy has been implemented to improve the resolution of Higgs candidates' mass.
- The event selections that are specific to the new signal are added and optimized.
- The background estimation is evaluated to be well-established.

Since no significant excess was observed unfortunately, I have set the 95% CL limitation on the specific parameter of Type-II 2HDM. At the benchmark point of $\tan\beta = 2.0$ and $\sin(\beta - \alpha) = 0.6$ in Type-II 2HDM, $m_H > 666.9\text{GeV}$ is excluded with 95% CL. Furthermore, the limits on the cross-section of non-resonant signals with various $VVhh$ coupling strength, κ_{2V} , have been set and the following regions are excluded with 95% CL: $\kappa_{2V} < -0.56$, $2.89 < \kappa_{2V}$. Since this analysis is the first one that focuses on the hh production via VBF and the dedicated procedure for the new signal has been developed, this constraint on κ_{2V} was able to be set at the first time in the world.

We can also explore the VBF production mode using $b\bar{b}\gamma\gamma$, $b\bar{b}\tau\tau$, and so on. Because these leading channels have sensitivity, that is comparable with $b\bar{b}b\bar{b}$ channel, for the non-resonant signal in ggF analysis, these channels are expected to help us to improve the κ_{2V} measurement. Furthermore, about 30 times statistics of the pp collision dataset is expected in HL-LHC. The increased statistics help us to set more strong constraint on κ_{2V} ; expected excluded region corresponds to $\kappa_{2V} < 0.29$ and $\kappa_{2V} > 1.77$ using only this $hh \rightarrow b\bar{b}b\bar{b}$ analysis. New channels, ideas for physics analysis, and improved detector performances can improve the measurement.

Acknowledgement

I acknowledge the support of supervisors Toru Iijima and Makoto Tomoto. I am grateful for the support from the members of the VBF $hh \rightarrow 4b$ analysis group Yu Nakahama, Maximilian J Swiatlowski, Kalliopi Iordanidou, Tatjana Lenz, Jana Schaarschmidt, and Alexander Melzer, in the ATLAS experiment at CERN. I also would like to thank Yasuyuki Okumura, Yuji Enari, and the other members of ATLAS Japan group for thorough discussions on this work. This work was supported by JSPS KAKENHI Grant Number 18J15246.

Bibliography

- [1] ATLAS Collaboration. Observation of a new particle in the search for the Standard Model Higgs boson with the ATLAS detector at the LHC. *Phys. Lett. B*, Vol. 716, p. 1, 2012.
- [2] CMS Collaboration. Observation of a new boson at a mass of 125 GeV with the CMS experiment at the LHC. *Phys. Lett. B*, Vol. 716, p. 30, 2012.
- [3] ATLAS Collaboration. Combined measurements of Higgs boson production and decay using up to 80 fb⁻¹ of proton-proton collision data at $\sqrt{s} = 13$ TeV collected with the ATLAS experiment. *Phys. Rev. D*, Vol. 101, p. 012002, 2020.
- [4] ATLAS Collaboration. Combination of searches for Higgs boson pairs in pp collisions at $\sqrt{s} = 13$ TeV with the ATLAS detector. *Phys. Lett. B*, Vol. 800, p. 135103, 2020.
- [5] Jaan Einasto. Dark Matter. *Astronomy and Astrophysics 2010*.
- [6] et. al. P. Nadolsky. Progress in CTEQ-TEA PDF analysis. 2012.
- [7] Computer Physics Communications. Vol. 183, pp. 1605–1617, 2013.
- [8] Computer Physics Communications. Vol. 181, pp. 189–205, 2010.
- [9] Debtosh Chowdhury, Otto Eberhardt. Update of global Two-Higgs-Doublet model fits. 2018.
- [10] Fady Bishara, Roberto Contino, and Juan Rojo. Higgs pair production in vector-boson fusion at the LHC and beyond. *Eur. Phys. J.*, Vol. C77, No. 7, p. 481, 2017.
- [11] ATLAS Collaboration. The ATLAS Experiment at the CERN Large Hadron Collider. *JINST*, Vol. 3, , 2008.
- [12] ATLAS Collaboration. Optimisation of the ATLAS b -tagging performance for the 2016 LHC Run. 2016.
- [13] ATLAS Collaboration. Level-1 trigger: technical design report.
- [14] ATLAS Collaboration. "Luminosity Determination in pp Collisions at $\sqrt{s} = 13$ TeV using the ATLAS detector at the LHC. 2019.
- [15] P. Nason S. Frixione and C. Oleari. Matching NLO QCD computations with parton shower simulations: the POWHEG method. *JHEP*, Vol. 11, p. 070, 2007.
- [16] C. Oleari S. Alioli, P. Nason and E. Re. A general framework for implementing NLO calculations in shower Monte Carlo programs: the POWHEG BOX. *JHEP*, Vol. 06, p. 043, 2010.
- [17] S. Mrenna T. Sjostrand and P. Z. Skands. A brief introduction to PYTHIA 8.1. *Comput. Phys. Commun.*, Vol. 178, p. 852, 2008.

- [18] R. D. Ball et al. Parton distributions with LHC data. *Nucl. Phys.*, Vol. B867, p. 244, 2013.
- [19] ATLAS Collaboration. ATLAS Pythia 8 tunes to 7 TeV data. 2014.
- [20] F. A. Dreyer and A. Karlberg. Vector-Boson Fusion Higgs Pair Production at N³LO. *Phys. Rev. D*, Vol. 98, p. 114016, 2018.
- [21] H.-L. Lai et al. New parton distributions for collider physics. *Phys. Rev. D*, Vol. 82, p. 074024, 2010.
- [22] R. Frederix et al. Higgs pair production at the LHC with NLO and parton-shower effects. *Phys. Lett. B*, Vol. 732, p. 142, 2014.
- [23] J. Bellm et al. Herwig 7.0/Herwig++ 3.0 release note. *Eur. Phys. J. C*, Vol. 76, p. 196, 2016.
- [24] M. Czakon, P. Fiedler, and A. Mitov. Total Top-Quark Pair-Production Cross Section at Hadron Colliders Through $O(\alpha_S^4)$. *Phys. Rev. Lett.*, Vol. 110, p. 252004, 2013.
- [25] D. J. Lange. The EvtGen particle decay simulation package. *Nucl. Instrum. Meth. A*, Vol. 462, p. 152, 2001.
- [26] ATLAS Collaboration. Summary of ATLAS Pythia 8 tunes. 2012.
- [27] S. Agostinelli et al. GEANT4: A simulation toolkit. *Nucl. Instrum. Meth. A*, Vol. 506, p. 250, 2003.
- [28] . The ATLAS simulation infrastructure. *Eur. Phys. J. C*, Vol. 70, p. 823, 2010.
- [29] Luminosity Public Results Run2. <https://twiki.cern.ch/twiki/bin/view/AtlasPublic/LuminosityPublicResultsRun2>.
- [30] A. Hoecker et al. TMVA - Toolkit for Multivariate Data Analysis. 2007.
- [31] ATLAS Collaboration. Tagging and suppression of pileup jets with the ATLAS detector. 2014.
- [32] ATLAS Collaboration. Search for pair production of Higgs bosons in the $bbbb$ final state using proton-proton collisions at $\sqrt{s} = 13$ TeV with the ATLAS detector. *JHEP*, Vol. 01, p. 030, 2019.
- [33] Glen Cowan, Kyle Cranmer, Eilam Gross, and Ofer Vitells. Asymptotic formulae for likelihood-based tests of new physics. *Eur. Phys. J.*, Vol. C71, p. 1554, 2011. [Erratum: *Eur. Phys. J.*C73,2501(2013)].

Appendices

A The sensitivity with two case of cut on the η of the jets

In this analysis, the η regions for b -jets and VBF jets are completely separated to avoid weird behavior of pseudo-tagging in $2b/4b$ extrapolation. In this appendix, the yields in signal region and the demonstrated sensitivity with four cases of η cuts on jets are compared;

1. $|\eta_b| < 2.5$ for b -jets emitted from higgs candidates and $2.5 < |\eta_{\text{VBF}}| < 4.9$ for VBF-jets,
2. $|\eta_b| < 2.0$ for b -jets emitted from higgs candidates and $2.0 < |\eta_{\text{VBF}}| < 4.9$ for VBF-jets,
3. $|\eta_b| < 1.5$ for b -jets emitted from higgs candidates and $1.5 < |\eta_{\text{VBF}}| < 4.9$ for VBF-jets,
4. $|\eta_b| < 1.0$ for b -jets emitted from higgs candidates and $1.0 < |\eta_{\text{VBF}}| < 4.9$ for VBF-jets,

The m_{4b} distribution and the demonstrated count-based sensitivity with the optimized mass windows of Table 1 are shown in Figure 1 and Figure 2, respectively. The selection of $|\eta_b| < 2.0$ and $2.0 < |\eta_{\text{VBF}}| < 4.9$ has best sensitivity.

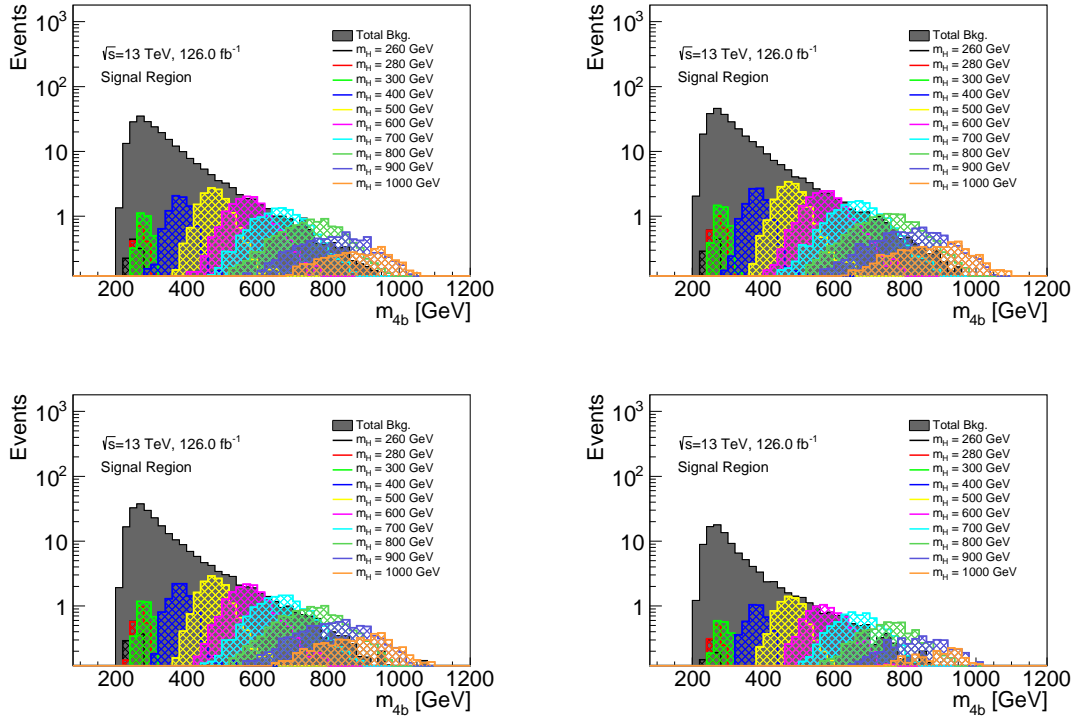


Figure 1: The m_{4j} distribution with the case of $|\eta_b| < 2.5$ and $2.5 < |\eta_{\text{VBF}}| < 4.9$ (upper left), $|\eta_b| < 2.0$ and $2.0 < |\eta_{\text{VBF}}| < 4.9$ (upper right), $|\eta_b| < 1.5$ and $1.5 < |\eta_{\text{VBF}}| < 4.9$ (lower left), and $|\eta_b| < 1.0$ and $1.0 < |\eta_{\text{VBF}}| < 4.9$ (lower right)

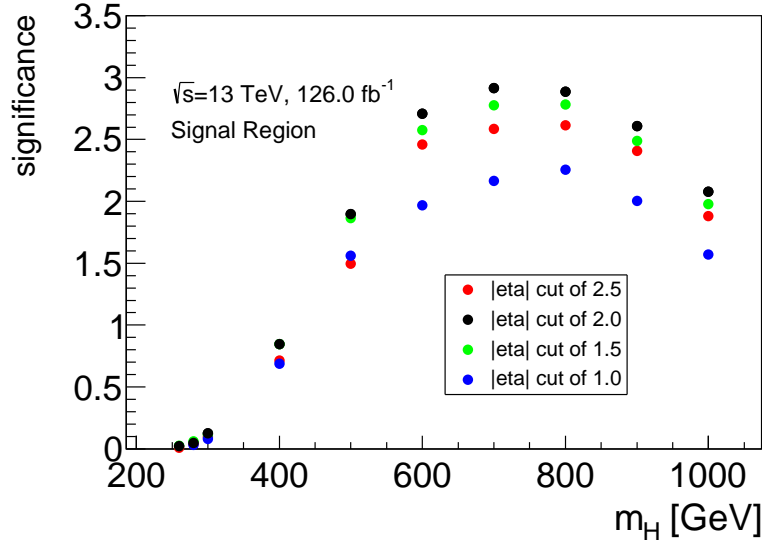


Figure 2: The demonstrated sensitivity with the case of $|\eta_b| < 2.5$ and $2.5 < |\eta_{\text{VBF}}| < 4.9$, $|\eta_b| < 2.0$ and $2.0 < |\eta_{\text{VBF}}| < 4.9$, $|\eta_b| < 1.5$ and $1.5 < |\eta_{\text{VBF}}| < 4.9$, and $|\eta_b| < 1.0$ and $1.0 < |\eta_{\text{VBF}}| < 4.9$

Table 1: The mass windows for the calculation of the count-based significance. These mass windows are optimized to maximize the significance.

m_H (GeV)	mass window in m_{4b} (GeV)
260	$200 < m_{4b} < 260$
280	$220 < m_{4b} < 280$
300	$250 < m_{4b} < 300$
400	$350 < m_{4b} < 450$
500	$410 < m_{4b} < 600$
600	$500 < m_{4b} < 700$
700	$600 < m_{4b} < 800$
800	$660 < m_{4b} < 950$
900	$750 < m_{4b} < 1300$
1000	$800 < m_{4b} < 1500$

B Comparison of distributions with different pseudo tag rate

In this section, the distributions of the $t\bar{t}$ MC in 2b and 4b regions at the preselection (just after choosing 4 b-jets and 2 VBF jets) are shown. The pseudo-tag rate f for 2b sample is determined so that the yields of the 2b sample weighted by f becomes consistent with 4b sample at the preselection level. The distributions of non-all hadronic $t\bar{t}$ are listed in Section B.1. The distributions of 2b and 4b samples are consistent with each other, except for the nJetOther. However, the impact of the inconsistent on the nJetOther of non-all hadronic $t\bar{t}$ doesn't have impact on the fit of the f for the QCD multi-jet background. The distributions of all hadronic $t\bar{t}$ are listed in Section B.2. All distributions of 2b and 4b samples are consistent with each other.

B.1 Non-all hadronic $t\bar{t}$

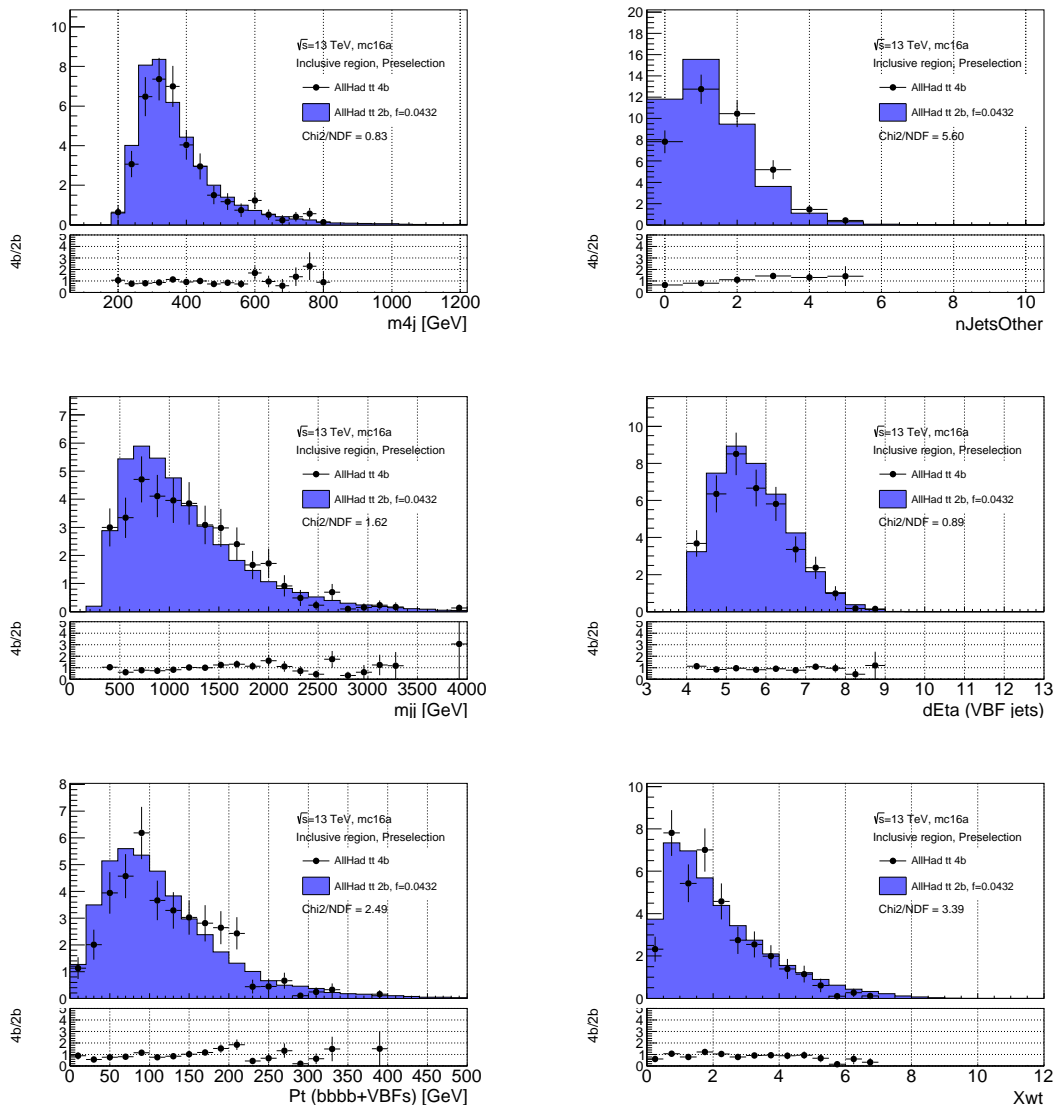


Figure 3: Each distribution of 4b and 2b MC samples of non all hadronic $t\bar{t}$, without 2b reweighting and with 2b reweighting using psedo-tag-rate f of 0.0432 for 2016.

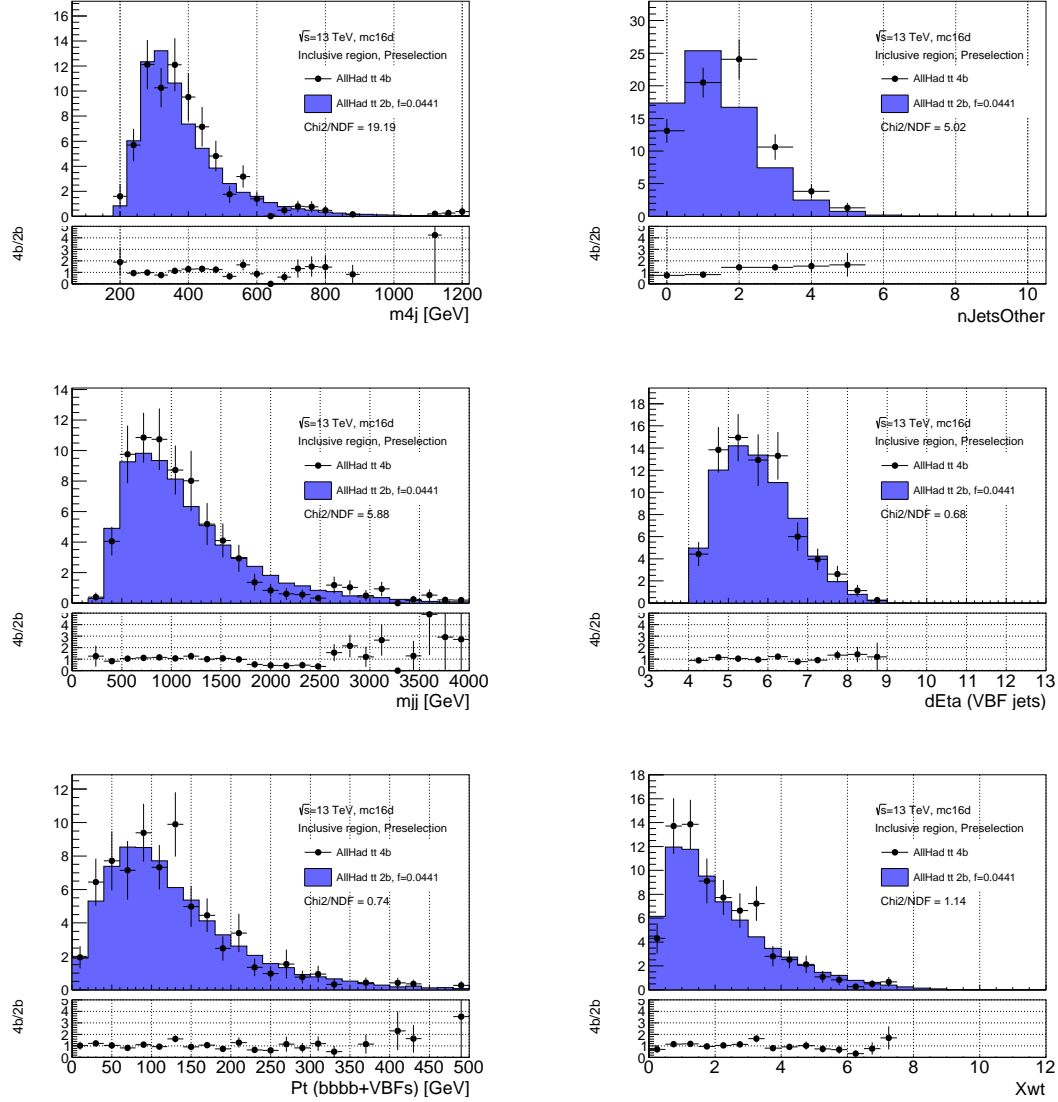


Figure 4: Each distribution of 4b and 2b MC samples of non all hadronic $t\bar{t}$, without 2b reweighting and with 2b reweighting using pseudo-tag-rate f of 0.0441 for 2017.

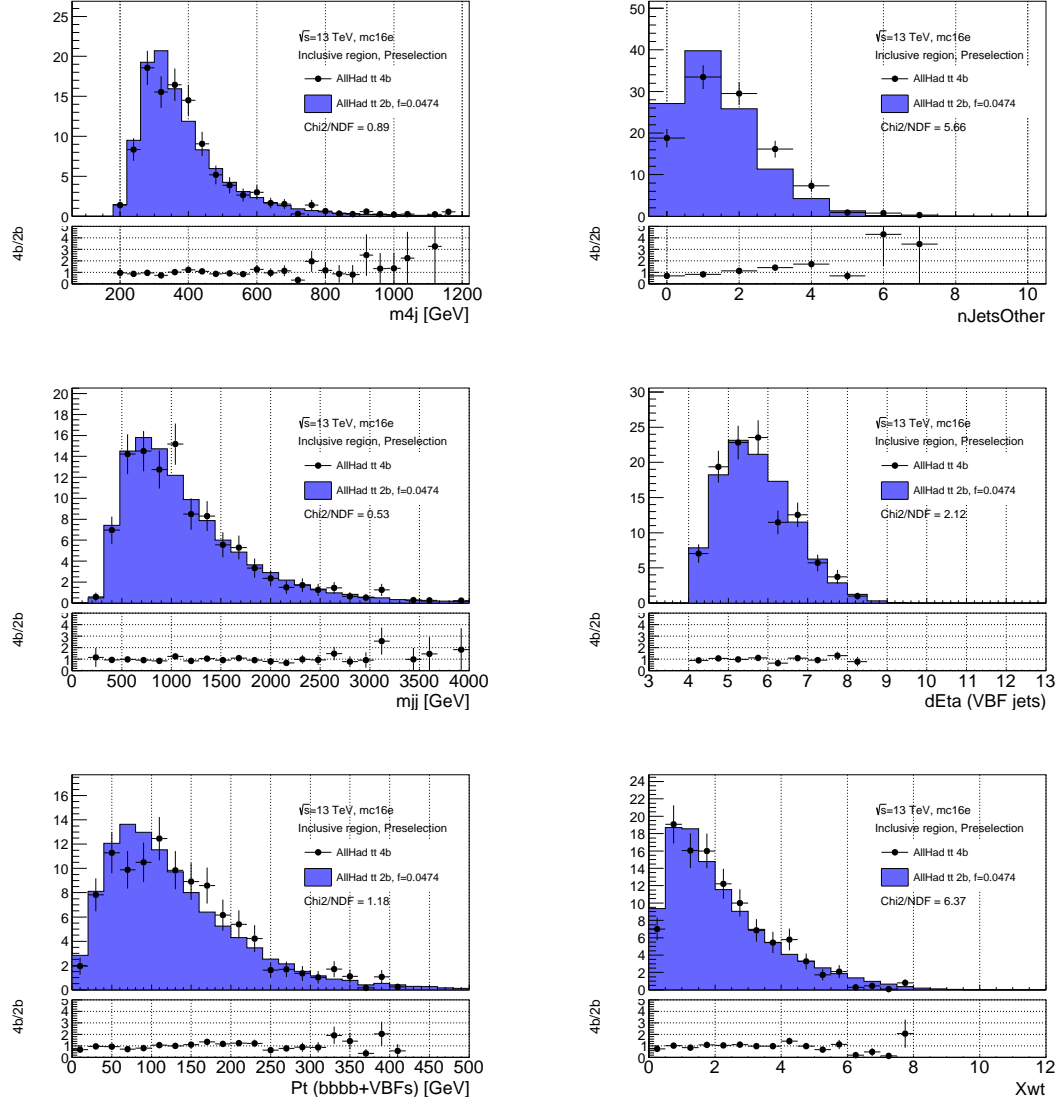


Figure 5: Each distribution of 4b and 2b MC samples of non all hadronic $t\bar{t}$, without 2b reweighting and with 2b reweighting using pseudo-tag-rate f of 0.0474 for 2018.

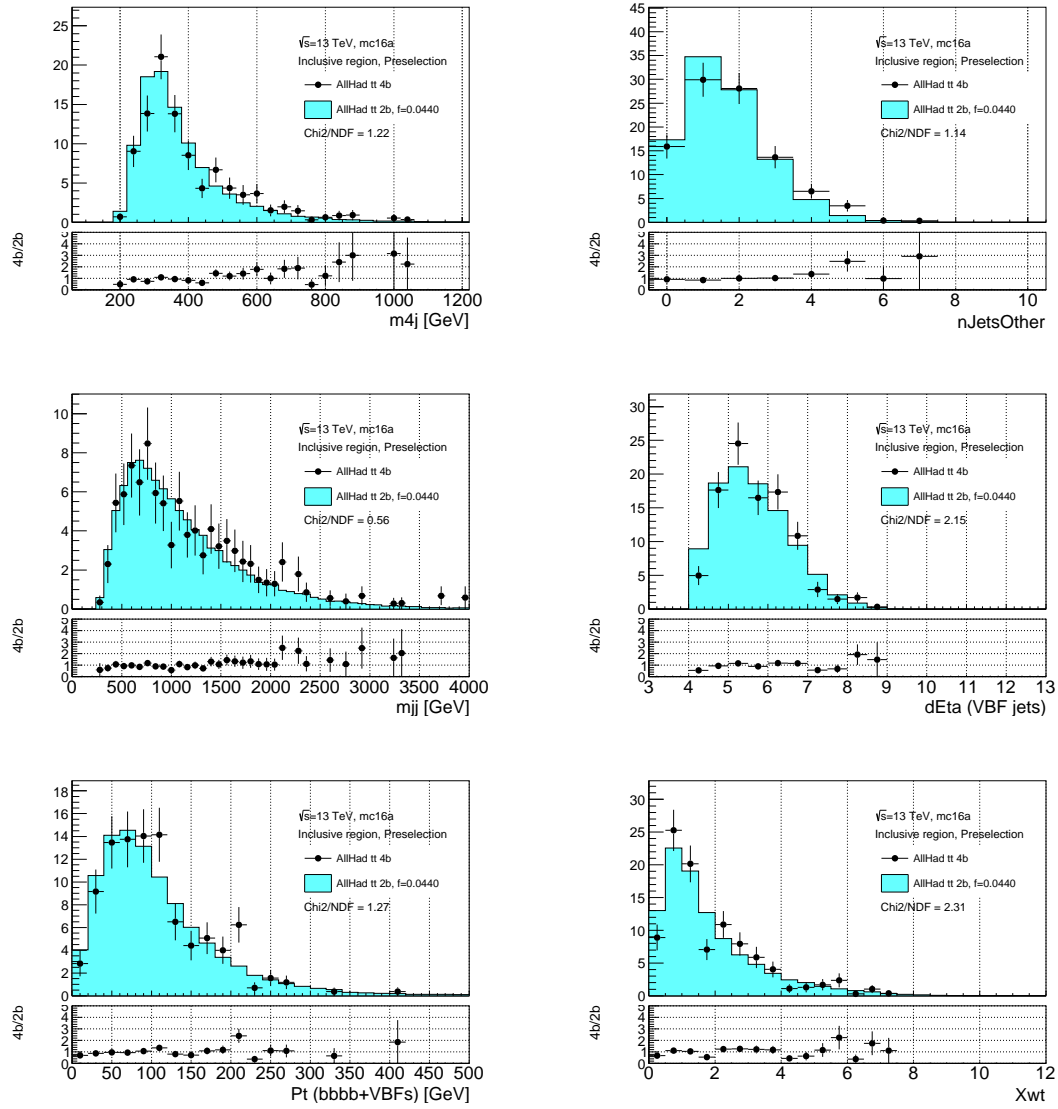
B.2 All hadronic $t\bar{t}$ 

Figure 6: Each distribution of 4b and 2b MC samples of all hadronic $t\bar{t}$, without 2b reweighting and with 2b reweighting using pseudo-rate f of 0.0440 for 2016.

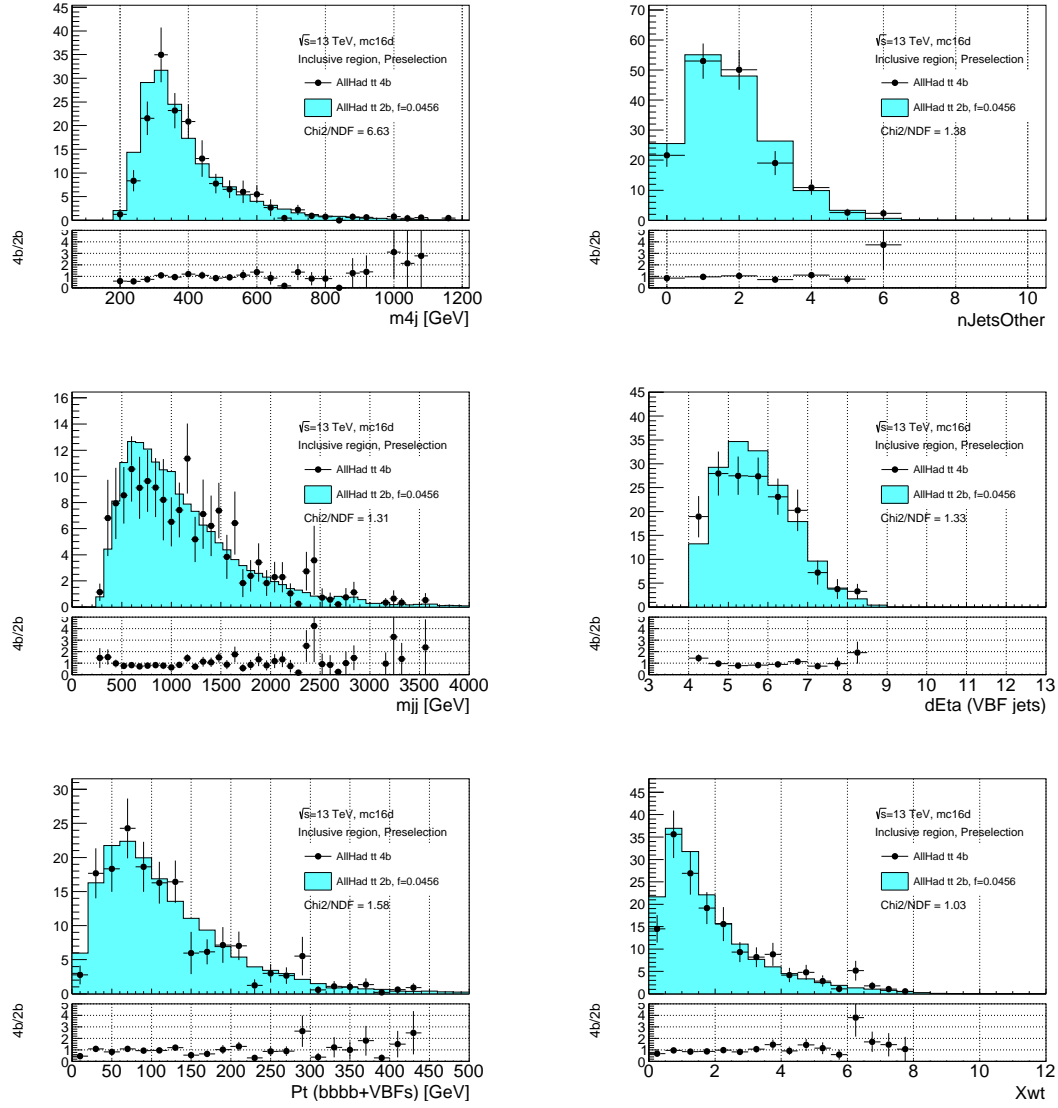


Figure 7: Each distribution of 4b and 2b MC samples of all hadronic $t\bar{t}$, without 2b reweighting and with 2b reweighting using pseudo-tag-rate f of 0.0456 for 2017.

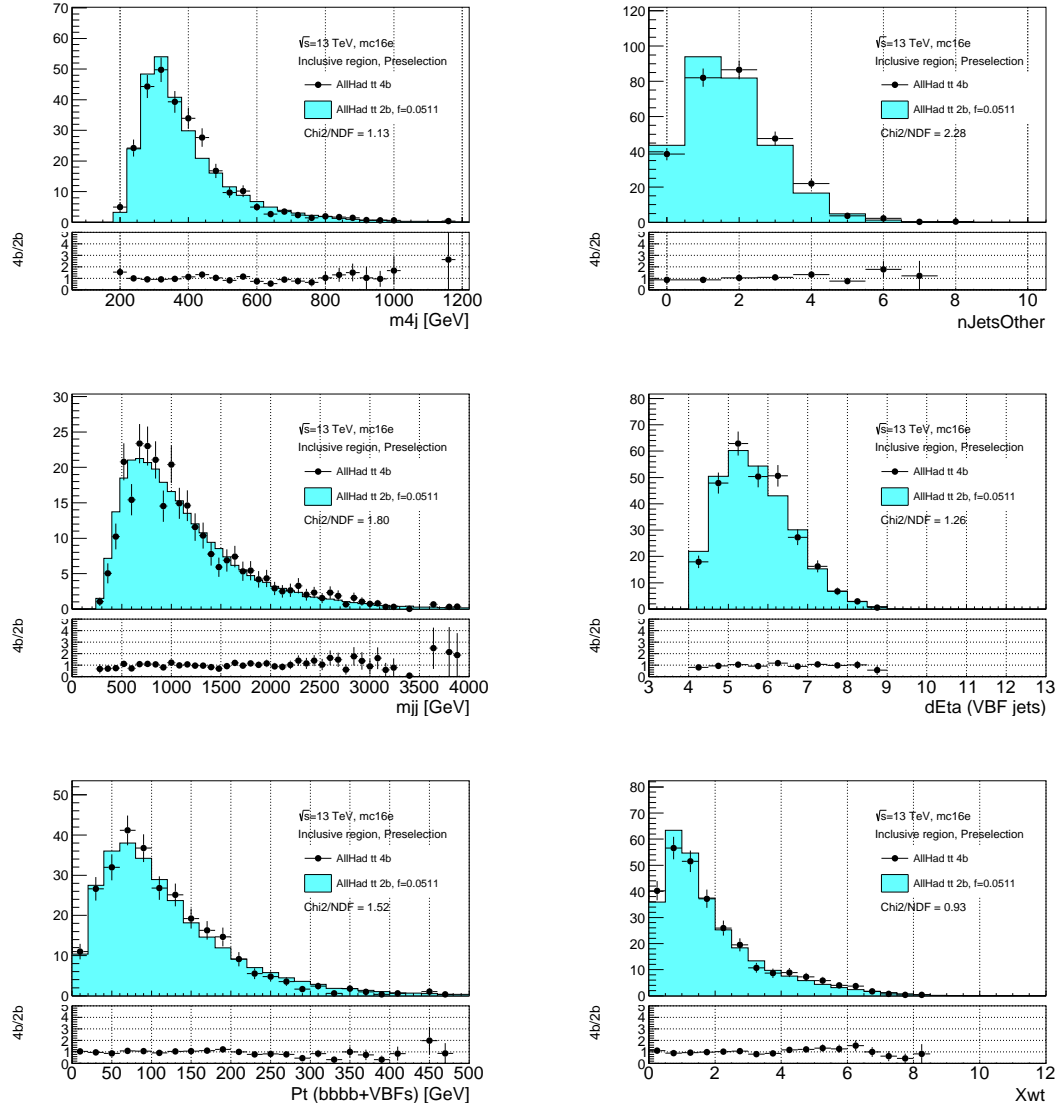


Figure 8: Each distribution of 4b and 2b MC samples of all hadronic $t\bar{t}$, without 2b reweighting and with 2b reweighting using pseudo-tag-rate f of 0.0511 for 2018.